Thesis for the degree of Doctor of Philosophy

Local Sea Level Observations Using Reflected GNSS Signals

Johan S. Löfgren

CHALMERS

Department of Earth and Space Sciences
CHALMERS UNIVERSITY OF TECHNOLOGY
Gothenburg, Sweden 2014

Local Sea Level Observations Using Reflected GNSS Signals

Johan S. Löfgren
ISBN 978-91-7385-955-4

Doktorsavhandlingar vid Chalmers tekniska högskola
Ny serie Nr 3637
ISSN: 0346-718X

Department of Earth and Space Sciences
Space Geodesy and Geodynamics
Chalmers University of Technology
SE–412 96 Gothenburg, Sweden
Phone +46 (0)31-772 1000

Cover
The picture on the left side shows the GNSS tide gauge at the Onsala Space Observatory. The graph on the right side displays sea level from phase-delay analysis (blue squares) and Signal-to-Noise Ratio (SNR) analysis (green circles) of GPS L_1 data recorded by the GNSS tide gauge, together with sea level observations from the co-located pressure tide gauge (black line). Observations are from October 10–11, 2012. A mean value is removed from each time series.

Printed in Sweden
Chalmers Reproservice
Gothenburg, Sweden 2014

Local Sea Level Observations Using Reflected GNSS Signals

Johan S. Löfgren
Department of Earth and Space Sciences
Chalmers University of Technology

Abstract

Sea level rise due to global warming is predicted to have a large impact on human society, especially for populations living in coastal regions and on islands. It is therefore of great importance to monitor the sea level and to increase the understanding of the local hydrodynamic and meteorological responses to a global sea level rise.

The focus of this thesis is to estimate the local sea level using Global Navigation Satellite System (GNSS) signals reflected off the sea surface. These signals were recorded in two different ways using a GNSS tide gauge at the Onsala Space Observatory, consisting of standard geodetic-type commercially off-the-shelf GNSS equipment. First, the phase-delay of the reflected GNSS signals were recorded directly with a receiver connected to a nadir-looking antenna. Together with the phase-delay of the direct signals, recorded with a receiver connected to a zenith-looking antenna, standard geodetic analysis provided GNSS sea level observations. Second, the Signal-to-Noise Ratio (SNR) recorded with the receiver connected to the zenith-looking antenna, provided an indirect measurement of the reflected GNSS signals, as the reflected signals interfered with the direct GNSS signals and affected the recorded observables. From analysis of the multipath oscillations, an additional type of sea level observation was possible. Furthermore, the SNR-analysis method allowed other GNSS stations, located close to the ocean, in different parts of the world to become GNSS tide gauges.

The GNSS-derived sea level from the GNSS tide gauge at the observatory was compared with independent observations of sea level from co-located traditional tide gauges, showing a high level of agreement with correlation coefficients of 0.89–0.99. The sea level results from the phase-delay analysis performed better with respect to the traditional sea level records than the results from the SNR-analysis. As an example, the Root-Mean-Square (RMS) differences from 1 month of observations between the GNSS-derived sea level (using frequency band L_1) and the sea level from the co-located tide gauge were 3.2–3.5 cm and 4.0–4.7 cm for the phase-delay analysis and the SNR-analysis, respectively.

Sea level results applying the SNR-analysis for data of 5 different GNSS stations around the world were compared to independent co-located traditional tide gauge records. The results showed RMS differences on the order of 6.2 cm for stations with low tidal ranges (up to 165 cm) and 43 cm for stations with high tidal ranges (up to 772 cm). In this case, an extended SNR-analysis approach was applied, modelling a time dependent sea level.

Keywords: *GNSS, GPS, GLONASS, GNSS-R, reflected signals, multipath, sea level, tide gauge, phase-delay, signal-to-noise ratio*

Appended Publications

This thesis is based on the work contained in the following papers, referred to by Roman numerals in the text.

I Löfgren, J. S., R. Haas, & J. M. Johansson, (2011), Monitoring coastal sea level using reflected GNSS signals, *Journal of Advances in Space Research*, 47(2), pp. 213–220.

II Löfgren, J. S., R. Haas, H.-G. Scherneck, & M. S. Bos, (2011), Three months of local sea level derived from reflected GNSS signals, *Radio Science*, 46, RS0C05, 12 pp.

III Larson, K. M., J. S. Löfgren, & R. Haas, (2013), Coastal Sea Level Measurements Using a Single Geodetic GPS Receiver, *Journal of Advances in Space Research*, 51(8), pp. 1301–1310.

IV Löfgren, J. S., R. Haas, & H.-G. Scherneck, Sea level time series and ocean tide analysis from multipath signals at five GPS sites in different parts of the world, *submitted to Journal of Geodynamics, September 2013.*

V Löfgren, J. S., & R. Haas, Sea level measurements using multi-frequency GPS and GLONASS observations, *submitted to EURASIP Journal on Advances in Signal Processing, December 2013.*

Other Publications

Besides the appended papers, the author has contributed to the following publications.

1. Löfgren, J. S., R. Haas, & J. M. Johansson, (2009), Sea level monitoring using a GNSS-based tide gauge, *Proceedings of the 2nd International Colloquium - Scientific and Fundamental Aspects of the Galileo Programme*, Proceedings CD-ROM, 14–16 October 2009, Padua, Italy.
2. Löfgren, J. S., R. Haas, & J. M. Johansson (2010), High-rate local sea level monitoring with a GNSS-based tide gauge, *Proceedings of the 2010 IEEE International Geoscience and Remote Sensing Symposium (IGARSS)*, Proceedings DVD-ROM, pp. 3616–3619, 25–30 July 2010, Honolulu, HI, USA.
3. Löfgren, J. S., F. Björndahl, A. W. Moore, F. H. Webb, E. J. Fielding, & E. F. Fishbein, (2010), Tropospheric correction for InSAR using interpolated ECMWF data and GPS zenith total delay from the Southern California Integrated GPS Network, *Proceedings of the 2010 IEEE International Geoscience and Remote Sensing Symposium (IGARSS)*, Proceedings DVD-ROM, pp. 4503–4506, 25–30 July 2010, Honolulu, HI, USA.
4. Löfgren J. S., R. Haas, & H.-G. Scherneck, Sea-level analysis using 100 days of reflected GNSS signals, *Proceedings of the 3rd International Colloquium Scientific and Fundamental Aspects of the Galileo Programme*, Proceedings CD-ROM, 31 August–2 September 2011, Copenhagen, Denmark.
5. Hobiger, T., R. Haas, & J. S. Löfgren, GLONASS-R: GNSS reflectometry with an FDMA based satellite navigation system, *submitted to Radio Science, December 2013.*

Acknowledgements

First of all, I would like to express my sincere thanks to my supervisor Rüdiger Haas, whose direction and support has been most appreciated and without whom, this work would not have been possible. I have had a lot of fun over the last years and you have always been supportive, enthusiastic, and available to answer questions. Thanks also to all the other past and present colleagues in the Space Geodesy and Geodynamics group at Chalmers University of Technology (CTH), in which I also include the Time and Frequency group at SP Technical Research Institute of Sweden. I would like to especially thank Jan Johansson, who during my master's thesis sent me to the Jet Propulsion Laboratory in California, USA, where I worked with the brilliant researchers Frank H. Webb, Angelyn W. Moore, Eric J. Fielding, and Evan F. Fishbein. Without that experience, I'm not sure that I would have started as a PhD student.

I would also like to extend my special thanks to Per Jarlemark and Kristine M. Larson. Per was very helpful, and enthusiastic when I started to write my own code for analysis of phase-delay data. Kristine visited the group as a CTH Jubilee Professor during the summer of 2011 and brought a lot of knowledge with her. With her great mind, she was very valuable and supportive in helping me discover the world of SNR-analysis.

I have really enjoyed working both at the Department of Earth and Space Sciences at CTH and at the Onsala Space Observatory during the past 5 years. There are so many great colleagues and friends there, making it a great environment to work in. My fellow doctoral students have meant a lot when facing challenges and difficulties, as well as in the day-to-day life. I would like to specially acknowledge the doctoral students in the Radio Astronomy and Astrophysics group and in the Radar Remote Sensing group, with whom I have spent a lot of my time. In addition, I would like to give thanks to all of the people who spent their Wednesday lunches playing floorball. At the observatory, the people at the workshop, in particular Lars Wennerbäck, have been crucial for the construction of the GNSS tide gauge installation. Thank you for great ideas and the good design. I would also like to thank Roger Hammargren at the observatory for making things work, especially related to computers and VLBI.

Finally, many thanks to my family and friends who have supported me all of these years. Most importantly, I could not have done this without the support and encouragement of my soon-to-be wife, Hanna. You make life beautiful!

Johan
Gothenburg, January 2014

Contents

1 Introduction

Observing and monitoring the sea level and its changes is of great importance for human society, especially for populations living in coastal regions and on islands. With the impact of global climate change on the sea level by, e.g., melting of large masses of ice in polar and subpolar regions and bringing freshwater into the ocean, thermal expansion of sea water, and changes in atmospheric and ocean circulation, these areas are highly exposed (*Bindoff et al.*, 2007). In particular there are severe consequences from extreme weather such as storms, extreme waves, and cyclones, which strike hard against the population and in addition impact on the economy (*Nicholls et al.*, 2007). An example is that it is predicted that about 120 million people are exposed annually to tropical cyclone hazards, which killed about 250 000 people from 1980 to 2000 (*Bindoff et al.*, 2007). With an anticipated sea level rise, the occurrences of these extreme events are increasing and it is predicted that by the end of the 21st century, up to 332 million people living in coastal and low-lying areas will be directly affected by flooding from sea level rise (*Watkins et al.*, 2007). Furthermore, the displacement of these people will affect millions more. Because of the large impact on human society, it is crucial to monitor the sea level and to increase the understanding of the local hydrodynamic and meteorological response to a global sea level rise.

Today sea level is measured both locally with tide gauges, which has been used during the last centuries (*IOC*, 2006), and globally by satellite altimetry, which has been the dominating technique for the last 25 years. These measurements, with different spatial resolutions, are important, since the sea level change is spatially highly non-uniform, meaning that in some regions the sea level is rising at a higher pace than the global average whereas in other regions the sea level is decreasing (*Bindoff et al.*, 2007). As an example, Figure 1.1 illustrates the regional sea level trends from satellite altimetry during the period from October 1992 to March 2010. From Figure 1.1, it is apparent that in some areas the trend is positive, e.g., in the west parts of the North Pacific Ocean (east of the Philippines) where the trend is around +12 mm/year, whereas in other areas the trend is negative, e.g., in the east parts of the North Pacific Ocean (west of Middle America) where the trend is around –4.8 mm/year.

The Intergovernmental Panel of Climate Change (IPCC) is a scientific intergovernmental body with a mission to provide comprehensive scientific assessments of the risk of climate change caused by human activity its consequences, and the possibilities for adapting to or to mitigate the effects. The fifth assessment report from the IPCC has been accepted, but not approved in detail and can therefore not be cited (publication is expected in the beginning of 2014). However, in the previous IPCC assessment report it is stated that the global mean sea level is rising, with scenarios of sea level rise in the range of 18 cm to 59 cm by the end of the 21st century (*IPCC*, 2007). From measurements using tide gauges situated on stable land regions, the average global mean sea level rise from 1961 to 2003 was $+1.8 \pm 0.5$ mm/year (*Bindoff et al.*, 2007). From satellite altimetry, however, the global mean sea level rise from 1993 to 2003 was $+3.1 \pm 0.7$ mm/year. The discrepancy in the IPCC results from tide gauges and satellite altimetry probably originates from a bias in the tide gauge dataset where long sea level records are usually from coastlines (not ocean interiors) in the northern hemisphere and the utilised data are from a small number of tide gauges (*Bindoff et al.*, 2007).

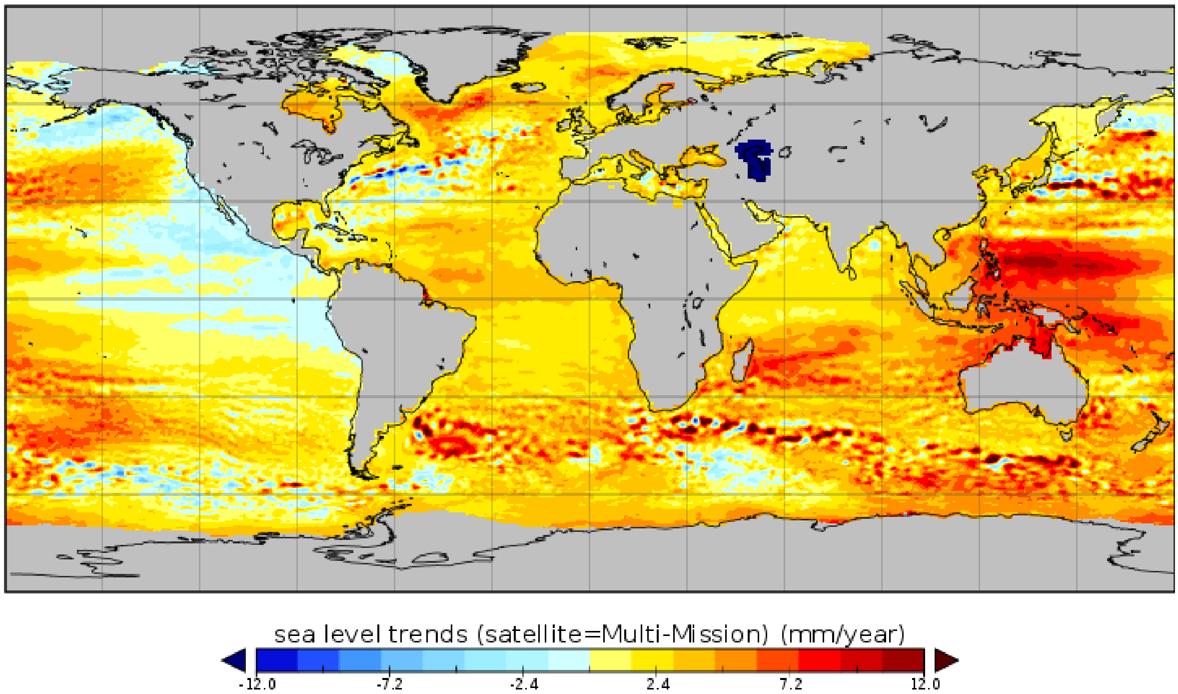

Figure 1.1: *Regional mean sea level trends from October 1992 to March 2010 in mm/year. The image is the result of processing of satellite altimetry data from missions Jason-1 & 2, Topex/Poseidon, Envisat, GFO, ERS-1 & 2, and Geosat. Regional differences in sea level of –12 to +12 mm/year are visible. However, the global rise in mean sea level has been estimated to +3.27 mm/year with a slope error of 0.6 mm/year with a 90 % confidence interval using data from the three satellite missions Jason-1 & 2 and Topex/Poseidon. The image was produced with data from AVISO (2011) (courtesy of CLS/CNES/LEGOS).*

Sea level observations with tide gauges are measurements of the vertical distance between the sea surface and the land surface. These measurements are relative to the Earth's crust (*Scherneck et al.*, 2002), through the benchmark on land where they are established, which is in motion on different time scales. This means that tide gauge measurements are affected by both sea level changes and land surface changes. One of the important observations for coastal societies is of course the sea level change with respect to land. However, for applications related to changes in the global ocean volume, e.g., the global sea level budget, and for sea level measurements in tectonically active regions, absolute sea level measurements are necessary, i.e., sea level measurements with respect to the a terrestrial reference frame (*Church et al.*, 2011). This means that all land motions need to be known in order to measure the sea level change due to ocean water volume and other oceanographic changes. It is possible to predict Global Isostatic Adjustment (GIA) from global geodynamic models (*Bindoff et al.*, 2007), but other land motions are not that well known. Thus, there is a need for nearby geodetic or geological data. Nevertheless, such datasets are not always available, and the result is that sea level measurements in regions with major tectonic activity are often disregarded for an overall sea level analysis.

This is where measurements with Global Navigation Satellite Systems (GNSS) can contribute. One of the main applications for GNSS is to measure position and velocity. This means that GNSS can be used to measure land surface changes (see e.g., *Lidberg et al.*, 2010; *Scherneck et al.*, 2010). By combining tide gauge observations of sea level with GNSS observations of land surface (provided that the GNSS measurements are representative for the location of the tide gauge), it is possible to derive sea level change with respect to the International Terrestrial Reference Frame (ITRF), see e.g., *Wöppelmann et al.* (2009); *Schöne et al.* (2009).

The absolute sea level measurements, with the inclusion of GNSS measurements, can in addition be of importance for calibration of satellite altimetry. By combining altimetry measurements with tide gauge records, it is possible to correct for instrumental biases in the altimetry data (see e.g., *Mitchum*, 1994; *Chambers et al.*, 1998; *Mitchum*, 2000), provided that the tide gauge records are not influenced by land surface changes.

Furthermore, GNSS signals reflected off the ocean surface can be used as a single technique to measure sea level. The advantage of using reflected GNSS signals for remote sensing of the sea surface, compared to measurements by traditional tide gauges, is the possibility of measuring absolute sea level, i.e., sea level with respect to the ITRF. With GNSS measurements, it is actually possible to measure both the sea level height, i.e., sea level relative to land as measured by a traditional tide gauge, and the land surface height, i.e., the land motion. As previously described, combining the both measurements allows to derive absolute sea level.

There are several ways to use reflected GNSS signals to measure sea level. In this thesis, the observation of local sea level with land-based commercially off-the-shelf GNSS equipment is presented. The measurements are carried out with a so-called GNSS tide gauge that is realised with either one antenna (zenith-looking) or two antennae (one zenith and one nadir-looking). The sea level analysis is based on Signal-to-Noise Ratio (SNR) data and phase-delay data, respectively.

As an introduction to the subject, ***The History of Sea Level Observations*** is presented, followed by a section on ***Sea Level Observations with GNSS***, which shortly guides the reader through what has been done in the fields until now. The introduction ends with explaining the ***Thesis Structure***, which introduces the main part of the thesis.

1.1 The History of Sea Level Observations

Throughout time, people living close to the ocean have always utilised the water as a resource, e.g., for food and for transportation. There are numerous historical examples, from 4000 BC, when Polynesian traders travelled long distances in the Pacific Ocean, through the 15th century, when explorers such as Christopher Columbus set sail going across the Atlantic Ocean to the new world, up to today, when much of our transports are ocean-based (*Stewart*, 2008). However, in recent times much attention has been given to extreme events in the ocean such as storm surges and tsunami waves together with the rise in global sea level due to global warming. Nonetheless, what is common for the society in all these eras is the dependency on the ocean and the necessity of observing its changes on different timescales.

Tide poles or staffs have been used to measure sea level for thousands of years. This is most probably due to their simple (but effective) and straight forward design, consisting of a vertical pole with etched horizontal markings, mounted to a stable structure in the water. An early example of usage is the Nilometers used by the ancient Egyptian priests to warn their people of imminent flooding of the Nile (*Pugh*, 1996). Furthermore, tide poles were also found in harbours throughout the history of seafaring, usually constructed by engraved levels in the seawalls. This was of course especially important in regions with high tidal range, e.g., at Avonmouth in the Bristol Channel (United Kingdom) which experience a tidal range of about 14 m (*NOC*, 2010).

As previously mentioned, observations of sea level have been carried out for thousands of years. However, understanding the mechanisms behind, e.g., the gravitational attraction of the Moon and the Sun creating tides was not explained until the 18th century. The first historic record of connecting the local variations in sea level to the Moon and Sun can be found in the Samaveda of the Indian Vedic period, 2000–1400 BC (*Pugh*, 1996). Though, it was not until the 17th century, that three serious theories emerged: Galileo Galilei (1564–1642), the earth rotates annually around the sun and daily about its own axis giving rise to sea motion which is modified by the seabed; René Descartes (1596–1650), space is full of invisible matter (ether) that exerts pressure on the sea when the Moon exerts pressure on the ether; Johannes Kepler (1571–1630), the Moon exerts gravitational attraction on the oceans (when it is overhead) and this is balanced by the Earth's attraction. As the heliocentric system of planets were gradually accepted, Kepler's theories of gravitational attraction was adopted, but it was not until the 18th century that Isaac Newton's (1642–1727) law of gravitational attraction could thoroughly explain the tides (*Pugh*, 1996). This was also the time when observations of sea level started in Stockholm (Sweden). This is the longest continuous time series of sea level in the world, starting from 1774 (*Hammarklint*, 2010).

The most common system for measuring sea level is probably the stilling well gauge, since the majority of permanent gauges installed after the mid-19th century are of this type (*Pugh*, 1996). The Swedish Meteorological and Hydrological Institute (SMHI) started to install stilling well gauges along the Swedish coast in 1886 and there are now 23 permanent stations (*Hammarklint*, 2010). The stilling well gauge design was first described by *Moray* (1666) and consists today of a vertical tube (well) of concrete, coated steel, or plastic (~1 m diameter) extending below the lowest sea level to be measured. In the bottom of the well or in the lower parts of the well, small openings allow inflow and outflow of water. A float in the well is vertically connected through a wire to a pulley (or a float wheel) and a counterweight system to a recording device.

During the last decades, satellite altimetry has been the dominant technique for large-scale sea level observations. The first satellite altimetry mission that delivered continuous worldwide observations of the Earth's oceans was the Seasat mission, which was launched in 1978 (*Rosmorduc et al.*, 2011). The principle of satellite altimetry is to transmit a short radar pulse, which is received by the satellite sensor after reflection off the sea surface, and to measure the travel time that is then converted to range (*Rees*, 2003). Each waveform illuminates a large area of the sea surface from about 2–10 km depending on the height of the satellite orbit, the sea surface topography, and roughness. This large scale coverage, compared to tide gauges, is the major advantage of satellite altimetry and enables global estimates of sea level, see Figure 1.1 for an example of regional sea level trends.

1.2 Sea Level Observations with GNSS

The evolution of GNSS started in the 1970s, with the development of the Global Positioning System (GPS) by the United States and the Globalnaya Navigatsionnaya Sputnikovaya Sistema (GLONASS) by the Soviet Union (*Seeber*, 1993). The two military systems for positioning and navigation started to form during the 1980s with an increasing number of satellites in orbit. Even before the completion of GPS and GLONASS in 1995, the civilian community quickly realised the potential these systems and an exploration of the possible applications of these new systems started (*Hofmann-Wellenhof*, 2001; *Polischuk et al.*, 2002).

The first measurements of sea level with GNSS signals, were conceptual very close to the original idea of how these system should be used, i.e., install a GNSS antenna and receiver on top of a buoy and continuously measure its position. This was done by e.g., *Hein et al.* (1990), estimating wave height and the buoys movement with the ocean currents for calibration of satellite altimetry. The idea was very elegant, however, some technical issues were found, e.g., there needs to be nearby land-based reference stations, additional sensors are needed to account for the dipping and tilting of the buoy, and multipath signals, i.e., signals that have reflected in the ocean surface, need to be reduced, for high-accuracy sea level measurements (*IOC*, 2006). GNSS buoys are still used today in calibration of satellite altimetry and in tsunami detection and warning systems (see e.g., *Cheng et al.*, 2002; *Kato et al.*, 2005; *Kuo et al.*, 2012).

The technique of using the freely available GNSS signals for remote sensing of the sea level was first proposed by *Martin-Neira* (1993), initiating the field of GNSS Reflectometry (GNSS-R). The idea was to develop a spaceborne system in low earth orbit, that receives both the direct GNSS signals and the GNSS signals that are reflected off the sea surface, for mesoscale (10–1000 km) sea level altimetry. This system, called the PAssive Reflectometry and Interferometry System (PARIS), is still being developed today.

With GPS and GLONASS almost fully operational, *Auber et al.* (1994) were researching a real-time aircraft tracking system based on GPS, when they were surprised to find that their GPS receiver locked onto the signal reflected off the water, during low altitude flights. This unwanted multipath effect that disturbed the measurements and reduced the accuracy of the position solution, also indicated the possibility to use commercial GNSS equipment for observing the sea level.

Towards the end of the decade, research in GNSS-R increased with multiple studies of receiving reflected signals from a variety of low-altitude airborne platforms, e.g., aircraft experiments of reflected GPS signals from the ocean using a specialised GPS receiver (*Garrison et al.*, 1998), comparing theoretical models of ocean scattered GPS signals with experimental aircraft data from an aircraft determining wave height, wind speed and wind direction (*Komjathy et al.*, 1998), mapping wetlands with reflected GPS signals (*Katzberg*, 1998), aircraft measurements of GPS signals reflected of sea ice (*Komjathy et al.*, 2000), and high precision aircraft ocean altimetry with GPS signals (*Lowe et al.*, 2002a). In addition, theoretical studies on receiving scattered GPS signals from the ocean with receivers in space were carried out (see e.g., *Katzberg & Garrison*, 1996), culminating in the first study of actual spaceborne observations of the ocean with reflected GPS signals by *Lowe et al.* (2002b). This study was carried out with the Spaceborne Imaging Radar-C (SIR-C) onboard the Shuttle Radar Laboratory-2 mission that flew in 1994 and was followed by measurements with the GPS bistatic remote sensing experiment onboard one of the United Kingdom's Disaster Monitoring Constellation (UK-DMC) satellites (*Gleason et al.*, 2005).

At the same time, *Anderson* (1995) (see also *Anderson*, 1996, 2000) was the first to use ground-based GPS measurements of the interference pattern in the recorded Signal-to-Noise Ratio (SNR), originating from the ocean-reflected signal interfering with the direct satellite signal, and relate that to sea level height. The precision of these measurements was about 12 cm with signals recorded with standard geodetic antennae (tilted 20° from the zenith to improve the reception of the reflected signals) and receivers. This SNR remote sensing method was later developed for soil moisture measurements, snow depth measurements, measurements of lake-ice thickness, locating reflecting objects (see e.g. *Larson et al.*, 2008, 2009; *Jacobson*, 2010; *Benton & Mitchell*, 2011, respectively), and local sea level measurements with a GPS tide gauge (*Paper III, and IV; Larson et al., 2013; Nakashima & Heki, 2013)* and with a GNSS tide gauge (*Paper V*).

Other land-based GNSS methods for sea level observations using one antennae directed towards the water, receiving the reflected signal, and one antenna directed towards the satellites, receiving the direct signal, and recording and analysing carrier-phase measurements have been developed, e.g., pond measurements as validation for the PARIS concept (*Martin-Neira et al.*, 2002), bridge measurements with customised receivers (*Rivas & Martin-Neira*, 2006), sea state and sea level measurements with equipment developed for commercial use (*Dunne et al.*, 2005; *Caparrini et al.*, 2007), bridge measurements with a software receiver (*Bai et al.*, 2011), and measurements with an experimental GNSS tide gauge (*Paper I, II, V*).

During recent years, the research in GNSS-R has had an increase in interest and several proposals have been submitted to both European Space Agency (ESA) and National Aeronautics and Space Administration (NASA) for satellite-based missions using the PARIS concept (*Rosmorduc et al.*, 2011). Previous implementations of this technique, using code correlation (correlating the reflected signals with the well-known replicas of the GPS satellites codes) have been tested in several campaigns, see e.g., *Cardellach et al.* (2009). The current research is dedicated towards cross-correlating the direct and reflected signals using the full power and bandwidth of the GNSS signals (e.g., *Rius et al.*, 2009; *Nogués-Correig et al.*, 2010; *Rius et al.*, 2012; *Cardellach et al.*, 2013), with the next phase being to implement a PARIS in-orbit demonstrator. In addition, also other GNSS-R methods for sea level observations are under research, e.g, altimetry based on residual observations of Doppler frequency (*Semmling et al.*, 2012, 2013) and measurements from correlation of direct and reflected GLONASS signals (*Hobiger et al.*, 2013).

The future for sea level observations with GNSS-R is bright, with two fully operational systems, GPS and GLONASS, and two additional systems on the way, BeiDou and Galileo. This means that there is an increasing number of reflected GNSS signals that are freely available. In addition, there are numerous of GNSS sites around the world, continuously recording GNSS signals affected by multipath from, e.g., the nearby ocean. This extensive GNSS-R dataset is just waiting to be analysed and turned into GNSS sea level.

1.3 Thesis Structure

This thesis covers the five appended articles, *Paper I, II, III, IV, and V*, and is aiming at giving the reader a more comprehensive understanding of the research therein, which can be summarised as local sea level observations using reflected GNSS signals. In addition, a few ideas and results that have not been published before are presented along the way.

The thesis started with an introduction (Chapter 1) explaining the importance of sea level observations and how GNSS can contribute to sea level measurements: by measuring land motion and by measuring the sea level directly. Additionally, a short ***Introduction*** to the history of sea level observations and the history of using GNSS for sea level observations was presented.

Since the thesis is dedicated to remote sensing of the ocean using GNSS signals, the next chapter (Chapter 2) describes ***Global Navigation Satellite Systems***. First, the general concept is presented followed by a short insight into the two main systems today: GPS and GLONASS. Secondly, the two upcoming systems, Galileo and BeiDou, are briefly described. Finally, the last sections are dedicated to the permanent reference networks of GNSS receivers and their significance.

Chapter 3 focuses on ***Reflected GNSS Signals***, investigating signal polarisation modifications due to reflection, the size and shape of the reflective surface, and the impact of signal reflection on the GNSS receiver performance.

The concept of the GNSS tide gauge based on commercially off-the-shelf GNSS equipment and using ***GNSS Reflectometry*** is presented in Chapter 4, explaining the different methods for connecting the GNSS observables to the local sea level. These methods are the phase-delay analysis, using both a zenith-looking and a nadir-looking antenna, and the SNR-analysis, using only a zenith-looking antenna. In addition, there is a section describing the data analysis for each method.

Furthermore, in Chapter 5, the GNSS tide gauge at the Onsala Space Observatory is described with its different installations and with the co-located traditional tide gauges that have been used for comparison and validation. ***GNSS Sea Level Results*** are shown for the GNSS tide gauge at the observatory and for a few GNSS stations world wide, which have been used as GNSS tide gauges.

The final chapter, ***Conclusions and Future Work*** (Chapter 6), presents the major conclusions, summarises *Paper I to V*, and introduces some ideas for the future.

2 Global Navigation Satellite Systems

The evolution of Global Navigation Satellite Systems (GNSS) started in the 1970s with the development of the Global Positioning System (GPS) by the United States and the Globalnaya Navigatsionnaya Sputnikovaya Sistema (GLONASS) by the Soviet Union (*Seeber*, 1993). From the beginning, the systems were primarily designed for military use in positioning and navigation. However, the civilian community quickly realised the potential of satellite-based positioning and found it increasingly useful in different fields. Today, civilian GNSS applications include positioning and navigation, time transfer, measurements of tectonic motion and post-glacial rebound, atmospheric remote sensing, near real-time meteorology, space weather monitoring, climate research, glacier and sea ice motion, snow depth and soil moisture measurements, tracking birds and mammals, tsunami early warning systems, landslide and volcano monitoring systems, and remote sensing of the ocean, see e.g., *Gfg*^{2} *Consortium* (2013).

In this chapter, ***The GNSS Concept*** will be presented together with the two fully operational systems today: the ***Global Positioning System*** and the ***Globalnaya Navigatsionnaya Sputnikovaya Sistema***. Currently, there are also several ***New GNSS***, either in the early stages of development or on their way to become fully operational. These systems are introduced together with ground-based ***GNSS Reference Networks***, which are used for both scientific and commercial purposes.

2.1 The GNSS Concept

In general, a GNSS consists of three segments: the space segment, including the satellite constellation and the broadcasted signals; the control segment, which is maintaining the system with orbit and clock determination and prediction and uplinking data to the satellites through several ground stations; and the user segment, consisting of the users (both military and civilian). An important part of the user segment is the several national and international organisations that maintain their own permanent GNSS reference network of ground-based receivers and antennae, providing data and products to the users, e.g., the Swedish permanent GNSS network and the International GNSS Service (IGS), see Section 2.5.

The main principle for positioning with a GNSS is to measure the distance to several satellites with known positions (*Hofmann-Wellenhof*, 2001). The fundamental observable is the signal propagation time from each satellite to the receiver. Each satellite signal is continually marked with its own transmission time and the carrier frequency is modulated with a known code (both depending on the multiple access technique of the specific GNSS). By correlating the received satellite signal with a signal replica generated in the receiver, it is possible to acquire the signal propagation time. Multiplying the propagation time with the signal velocity (approximately the speed of light) yields the range between the satellite and the receiver. However, since the satellite and the receiver clocks are not perfectly synchronised, this range is influenced by clock errors. Therefore, the measurement is not of the true range and is thus called the pseudorange. Each measurement of pseudorange contains four unknowns: the three dimensional coordinate of the true range (or actually the three dimensional coordinate of the receiver, since the positions of the satellites are known) and the clock errors. This means that at least four satellite observations are needed to solve this equation system.

The previously mentioned positioning concept is valid for measurements with the code, that is modulated on the carrier frequency on each satellite signal, and is performed with the correlation in the receiver (*Hofmann-Wellenhof*, 2001). This type of measurement is used for positioning with, e.g., car navigation systems and mobile phones, and positioning solutions with code measurements typically have accuracies of a few metres.

After correlation, the code and the navigation message (information about the satellite health, clock, orbit, and different corrections) are removed from the carrier signal (*Hofmann-Wellenhof*, 2001). The phase of the incoming signal is then compared with the phase of the signal replica generated in the receiver to perform a phase measurement. This means that the receiver can only determine the phase difference between the received signal at reception and the generated signal replica and not the full pseudorange. Consequently, this means that the observation is ambiguous by an integer number of wavelengths, which is called the integer or phase ambiguity (*Hofmann-Wellenhof*, 2001). The phase ambiguity is, however, the same for a given satellite-receiver pair as long as the receiver can keep continuous lock on the satellite signal. The observation of the phase measurements in units of metres can according to *Teunissen & Kleusberg* (1998) be described as

$$\lambda\, \Phi^j_A = \rho^j_A + c\,(\tau_A - \tau^j) + Z^j_A - I^j_A + \lambda\, N^j_A + \epsilon \tag{2.1}$$

where the left side of Equation 2.1 is the wavelength of the carrier λ times the observed carrier phase in units of cycles Φ^j_A. The right side of Equation 2.1 consists of the geometric range to the satellites ρ^j_A, the signal velocity (the speed of light in vacuum) c, the clock bias in the receiver τ_A, the clock bias in the satellite τ^j, the delay caused by the neutral atmosphere Z^j_A (also called tropospheric delay), the ionospheric delay I^j_A, the wavelength of the carrier, the phase ambiguity N^j_A, and the unmodeled errors ϵ, e.g., multipath and receiver noise. Superscript j and subscript A denote satellite and receiver, respectively.

As seen in Equation 2.1, the GNSS signals are affected when passing through the Earth's atmosphere. This contribution is for convenience separated into a tropospheric and an ionospheric delay. The troposphere is the lower part of the Earth's atmosphere from the surface to about 10–16 km defined by decreasing temperature with increasing altitude (actually the whole neutral atmosphere going up to 50 km is loosely referred to as the troposphere in GNSS data analysis). Because of the presence of neutral atoms and molecules, the GNSS signals are delayed in the troposphere (*Teunissen & Kleusberg*, 1998). The delay can be divided into Zenith Hydrostatic Delay (ZHD), which is caused by induced dipoles in the molecules, and the Zenith Wet Delay (ZWD), which is mainly caused by the permanent dipole moment of water vapour. The ZHD is the major part of the delay with a magnitude of about 2.3 m for a site at sea level and at standard atmosphere (1013 hPa). Since this delay is slowly varying as a function of pressure it can be estimated in the zenith direction using surface pressure measurements, see *Saastamoinen* (1971). The ZWD is smaller than the ZHD and can range from less than 1 cm to 40 cm. Nonetheless, the distribution of water vapour is highly variable and cannot be predicted accurately. Therefore, in high-accuracy positioning, the ZWD has to be treated as an unknown parameter and estimated together with the other parameters. To a first approximation, both ZHD and ZWD are handled together as a slant delay called Zenith Total Delay (ZTD), which is mapped to the directions of the observations using mapping functions, see e.g. *Davis et. al* (1985); *Niell* (1996).

The ionosphere is the upper part of the Earth's atmosphere, approximately 50–1000 km above the surface. Here the significant amount of free electrons, due to ionising radiation mostly from the Sun, delays the code measurements and advances the carrier phases (*Hofmann-Wellenhof*, 2001). The total amount of free electrons along the propagation path is defined as the Total Electron Content (TEC) and can vary between 5–60 TECU (1 TECU = 1×10^{16} electrons/m^2) depending on solar activity, time of day, season, and satellite and observation site position (*Ma et al.*, 2009). However, by using the ionospheric-free Linear Combinations (LC), two phase measurements from two different frequencies, the delay can be removed to the first order (99.9 %), see *Hernández-Pajares et al.* (2007).

The last term on the right side of Equation 2.1 consists of additional errors which are hard to model, e.g., receiver characteristics, which are built-in, and multipath signals, i.e., satellite signals that have reflected from structures in the surroundings of the antenna before reaching the antenna. Nevertheless, the effect of multipath signals can be mitigated by, e.g., microwave absorbing material on the bottom of the antenna, see *Ning et al.* (2011).

Carrier-phase measurements according to Equation 2.1 are used in most high-accuracy applications, e.g., tectonic motion and atmospheric remote sensing. The positioning solutions for these types of measurements have accuracies on the centimetre level and below.

2.2 Global Positioning System

The Global Positioning System (GPS) is today the most known GNSS due to it being the only fully operational system during the late nineties and until 2011. It was initially proposed by the United States Department of Defence in 1973, and had the first satellite launch in 1978 (*Hofmann-Wellenhof*, 2001). The nominal constellation consists of 24 satellites in 6 evenly spaced nearly circular orbit planes (4 satellites per plane). Each orbit plane is inclined 55° with the satellites at an altitude of 20 200 km above the Earth's surface. This constellation was finally realised in 1995 and today the GPS constellation consists of 31 fully operational satellites (*GPS World*, 2012a). The orbital period for each satellite is 12 sidereal hours (11 h 28 min 2 s), which means that each satellite makes approximately two revolutions per day.

GPS is currently using the two carrier signals L_1 (f = 1575.42 MHz, λ = 19.05 cm) and L_2 (f = 1227.60 MHz, λ = 24.45 cm). However, on newer generation satellites there is a third carrier signal L_5 (f = 1176.45 MHz, λ = 25.48 cm) for Safety-of-Life (SoL) applications in aviation (*GPS World*, 2012a). Additionally, the new generation satellites have an increased signal power, 6–10 dB, to improve operations.

In order to distinguish between satellites the GPS uses Code Division Multiple Access (CDMA). This means that each satellite is given a unique code with which it can be distinguished from the other satellites. In practice, each satellite is given two unique PseudoRandom Noise (PRN) codes, which are modulated on the two main carriers (*Hofmann-Wellenhof*, 2001). These PRN codes are the civilian Coarse/Acquisition-code (C/A-code) and the military Precision-code (P-code). The C/A-code is less precise than the P-code and modulated on the L_1 carrier for civilian use. The P-code is modulated on both carriers, but it is encrypted and can only be used by the military. Since 2005, there is also a second civilian code, which is modulated on the L_2 carrier called L_{2C} (*Inside GNSS*, 2006). The new L_{2C} signal does not have a higher signal power compared to the L_1 C/A-signal. However, with a more robust code structure and improved error-correcting methods, it can be used more effectively, leading to a greater data recovery than for the original L_2 signal (*Gakstatter*, 2006), which improves e.g., dual-frequency applications such as correction for ionospheric errors (*Inside GNSS*, 2006). Currently, 11 satellites transmit the L_{2C} signal and 4 satellites transmit the L_5 signal (*UNAVCO*, 2013).

In addition to the PRN codes there is a data message modulated on both carriers. This message consists of status information, satellite ephemeris (orbital parameters), satellite clock biases, and additional correction data (*Hofmann-Wellenhof*, 2001). For comparison to other GNSS, see Table 2.1, with a list of the main parameters of the four systems presented in this thesis.

2.3 Globalnaya Navigatsionnaya Sputnikovaya Sistema

The development of the Globalnaya Navigatsionnaya Sputnikovaya Sistema (GLONASS) started in 1976 in the Soviet Union. Several satellites were launched during 1982 and the system was fully operational in 1995. However, due to the collapse of the Russian economy, the maintenance of the system was reduced during several years until the early 2001, when a restoration was started (*Polischuk et al.*, 2002). GLONASS is now maintained by Roscosmos (the Russian Federal Space Agency) and is today again fully operational with 24 operational satellites and 3 in-orbit spare satellites (*GPS World*, 2012b).

The nominal constellation consists of 24 satellites distributed into three equally spaced orbital planes. Each orbital plane, containing 8 evenly spaced satellites, has an inclination of 64.8°, providing a higher latitude coverage than the GPS (*Hofmann-Wellenhof*, 2001). The nearly circular orbits are on an altitude of 19 100 km above the Earth's surface with an orbital period of 11 h 15 min 44 s. The orbits are designed so that the satellites take over each others positions, i.e., after one day the satellites in the orbital plane pass over the same spot as the previous satellite in that orbital plane. The repeat time for a satellite is 8 siderial days.

The GLONASS signal structure is different from that of GPS (*Hofmann-Wellenhof*, 2001). The PRN codes are the same for all satellites, and the way to distinguish between satellites is instead by using Frequency Division Multiple Access (FDMA). This means that for each satellite two individual carrier signals are assigned which lie around the center frequencies L_1 ($f = 1602.00$ MHz, $\lambda = 18.71$ cm) and L_2 ($f = 1246.00$ MHz, $\lambda = 24.06$ cm) in the frequency ranges 1598.06–1605.38 MHz (18.76–18.67 cm wavelengths) and 1242.94–1248.62 MHz (24.12–24.01 cm wavelengths), respectively. The channel separations are 562.5 kHz (L_1) and 437.5 MHz (L_2), with only 14 channels for 24 satellites. This is solved by assigning the same carrier frequencies to satellites located on opposite sides of the planet. These satellites will never be in view at the same time by a receiver on the surface of the Earth.

A C/A-code is modulated on the L_1 carriers and a P-code is modulated on both L_1 and L_2 carriers (*Hofmann-Wellenhof*, 2001). Both the C/A and the P-code are freely available. There is also a navigation message which is transmitted every 30 min containing the satellite position, velocity, and acceleration vectors.

For the future, GLONASS will in addition to the FDMA signals in L_1 and L_2 transmit CDMA signals on L_1, L_2, L_3 ($f = 1207.14$ MHz, $\lambda = 24.83$ cm) and possibly on L_5 ($f = 1176.45$ MHz, $\lambda = 25.48$ cm) (*GPS World*, 2012b). The first launch of a satellite transmitting a CDMA signal on L_3 was in February 2011, which opens up for international GNSS interoperability with the current CDMA system GPS and the future European CDMA system Galileo (*GPS World*, 2011). For comparison to other GNSS, see Table 2.1, with a list of the main parameters of the four systems presented in this thesis.

2.4 New GNSS

During recent years, several new GNSS and regional satellite navigation systems have evolved from both commercial and scientific interests and are today in different stages of development. Two of the new global systems that are currently advancing in different stages of deployment are the Galileo system of the European Union, with four satellites currently in orbit for a validation phase (*ESA*, 2013a), and the BeiDou system of the People's Republic of China, already with regional coverage and plans of launching additional satellites for global coverage (*Chong*, 2009).

2.4.1 Galileo

The Galileo project started in the 1990s by proposals from different countries that merged into a joint program for the European Union and ESA in 1999 (*Benedicto et al.*, 2006). As a part of the system development and testing, two experimental Galileo In-Orbit Validation Element (GIOVE) satellites were launched in 2005 (GIOVE-A) and in 2008 (GIOVE-B)(*Gao et al.*, 2008). These two satellites transmitted an experimental signal, securing the frequency spectrum, and allowed for testing of the payload and spacecraft environment. This in-orbit validation phase continued with four operational satellites that were launched, in pairs, in October 2011 and October 2012, providing the minimum required number of satellites for positioning and timing testing (*ESA*, 2013a). The next Galileo launch is planned for mid-2014 with two Full Operational Capability (FOC) satellites that are currently under testing (*Inside GNSS*, 2013b).

The planned satellite constellation consists of 30 satellites in three equally spaced orbital planes (*ESA*, 2013b). Each orbital plane, containing 9 evenly spaced satellites and 1 active spare satellite, has an inclination of 56°. The nearly circular orbits are on an altitude of 23 222 km above the Earth's

Table 2.1: *General information about the four main Global Navigation Satellite Systems (GNSS) that are available today. The today fully operational GNSS are the United States Global Positioning System (GPS) and the Russian Globalnaya Navigatsionnaya Sputnikovaya Sistema (GLONASS). In addition, the European Union are currently validating their Galileo system with four orbiting satellites, and the People's Republic of China is increasing the number of satellites in its BeiDou system with the aim of achieving global coverage in 2020.*

	GPS	GLONASS	Galileo	BeiDou
Affiliation	United States	Russia	Europe	China
Satellites	31 (24)[a]	27 (24)[a]	4 (27)[a]	4 (27)[ab]
Orbital planes	6	3	3	3[b]
Orbital height (km)	20 200	19 100	23 222	21 150[b]
Orbital period	11 h 28 min	11 h 15 min	14 h 7 min	12 h 53 min[b]
Orbital inclination	55°	64.8°	56°	55.5°[b]
Multiple access	CDMA	FDMA[c]	CDMA	CDMA
Carrier frequencies (MHz)	1575.42	1598.06–1605.38	1575.42	1561.098
	1227.60	1242.94–1248.63	1278.75	1589.742
	1176.45	1207.14	1207.14	1207.140
		1176.45	1176.45	1268.520
Current status	fully operational	fully operational	in-orbit validation	partly operational[d]

[a] Number of operational satellites and number of satellites for the nominal constellation.
[b] Numbers are for the BeiDou Medium Earth Orbit constellation. In addition, BeiDou has satellites in Geostationary Earth Orbit (GEO) and in Inclined GeoSynchronous Orbit (IGSO), see *Chong* (2009).
[c] In the future, GLONASS will in addition to transmitting FDMA signals in the L_1 and L_2 bands also transmit CDMA signals on L_1, L_2, L_3, and possibly also L_5, see *GPS World* (2012b).
[d] BeiDou has regional coverage, which is achieved with 5 GEO, 3 IGSO, and 4 Medium Earth Orbit satellites, see *Chong* (2009); *Inside GNSS* (2013a).

surface with an orbital period of 14 h 7 min, repeating every tenth sidereal day.

Similar to GPS, Galileo uses CDMA to distinguish between satellites. The system is inter-operable with GPS and GLONASS, transmitting signals in the L-band (*European Union*, 2010). The Galileo specified signal bands are E_5 (E_{5a}: $f = 1176.45$ MHz, $\lambda = 25.48$ cm; E_{5b}: $f = 1207.14$ MHz, $\lambda = 24.83$ cm), E_6 ($f = 1278.75$ MHz, $\lambda = 23.44$ cm), and E_1 ($f = 1575.42$ MHz, $\lambda = 19.03$ cm). In addition to the code modulated on the carrier signals, there is also a message consisting of status information, satellite ephemeris, satellite clock biases, and additional correction data. For a comparison to other GNSS, see Table 2.1, with a list of the main parameters of the four systems presented in this thesis.

2.4.2 BeiDou

The People's Republic of China has had plans since the 1980s to build an independent GNSS and completed its regional navigation system BeiDou-1 (BD-1) in 2003 (*Chong*, 2009). In 2005, the development of the successor of BD-1, called BeiDou-2 (also known as BDS and COMPASS) started with the first launch in 2007 (*Inside GNSS*, 2013a). BeiDou was established as a fully operational regional system in 2012 with the plan of global coverage before 2020.

In contrast to other GNSS, the BeiDou space segment consists of three different orbit constellations (*Chong*, 2009). The primary nominal constellation consists of 27 satellites in three equally spaced nearly circular orbital planes in Medium Earth Orbit (MEO; similar to other GNSS). The altitude is 21 150 km above the Earth's surface with an orbital period of approximately 12 h 53 min and the inclination of 55.5° (*ILRS*, 2012). In addition, there will be 5 satellites in Geostationary Earth Orbit (GEO) with an altitude of ~35 786 km above the Earth's surface, and 3 satellites in Inclined GeoSynchronous Orbits (IGSO). Both the GEO and IGSO will have an orbital period equal to the Earth's rotational period, however, because of the inclination of the IGSO, the satellites in this orbit will move in a north-south analemma once each siderial day. The current BeiDou space segment consists of 5 satellites in GEO, 5 satellites in IGSO, and 4 satellites in MEO (*Inside GNSS*, 2013a).

Similar to GPS and Galileo, BeiDou uses CDMA to distinguish between satellites and transmits in the L-band (*Chong*, 2009). The specified signal bands for BeiDou are B_1 (f = 1561.10 MHz, λ = 19.20 cm), B_{1-2} (f = 1589.74 MHz, λ = 18.86 cm), B_2 (f = 1207.14 MHz, λ = 24.83 cm), and B_3 (f = 1268.52 MHz, λ = 23.63 cm). For a comparison to other GNSS, see Table 2.1, with a list of the main parameters of the four systems presented in this thesis.

2.5 GNSS Reference Networks

With the evolution of GNSS, national and international ground-based networks have been constructed. These networks consists of antennae and receivers continuously recording GNSS data for use in various applications in both real-time and post-processing. The different applications can be everything from improving existing GNSS models to applied research in, e.g., land uplift and tectonic motion of the Earth's crust or atmospheric remote sensing, which significantly contributes to the international GNSS community. In Scandinavia there are several regional networks, e.g., the Swedish permanent GNSS network, contributing with data to the IGS, which provides both data and products free of charge for scientific use.

2.5.1 International GNSS Service

The International GNSS Service (IGS) is a non-commercial voluntary international confederation, consisting of more than 200 organisations in over 80 countries, supporting scientific research using GNSS (*Dow et al.*, 2009). The IGS was officially established in 1994 as a service of the International Association of Geodesy (IAG), but has been active already since 1992 under a different name. The service is self-governed by its members, where each organisation contributes with its own resources.

The foundation of the IGS is the global network of GNSS stations, see Figure 2.1, from which data are provided by the different organisations (*Dow et al.*, 2009). Both the data and the different products obtained from the data are provided free of charge. The initial and primary products are the GPS orbit and clock correction solutions, e.g., final solution satellite orbits and satellite and station clocks with with the accuracy of ~2.5 cm and ~75 ps Root-Mean-Square (RMS)/~20 ps standard deviation, respectively. However, products also include other orbit and clock solutions, GLONASS final ephemeris, earth rotation parameters, and atmospheric parameters. Recently, also real-time streaming and applications have become an interest for the IGS. In the future, IGS products will most probably involve Galileo and BeiDou data and products.

In addition to providing data and products, the IGS manages several working groups and pilot projects involving scientist from all over the world. The reason is to coordinate the research in fields of interest for the IGS and to develop future IGS products (*Dow et al.*, 2009). Examples of working groups and pilot projects are the Antenna Working Group (dedicated to antenna phase centre determination), the Multi-GNSS Experience (dedicated to tracking, comparison, and analysis of all GNSS signals), Reference Frame Working Group (dedicated to station position and velocity products and earth rotation

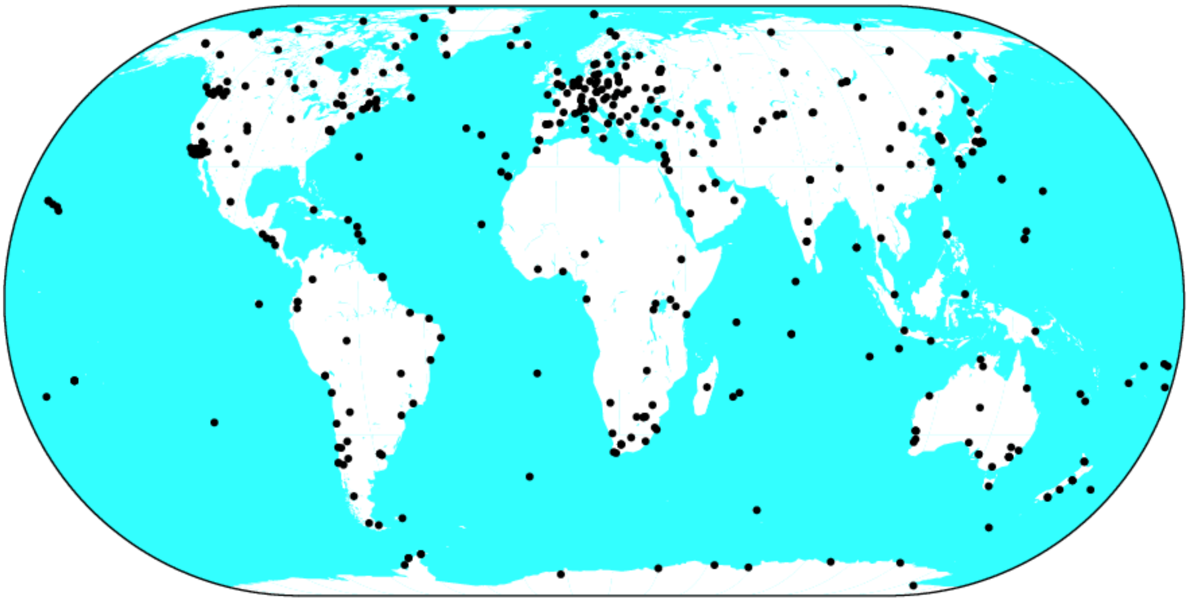

Figure 2.1: *A world map showing the global distribution of the Global Navigation Satellite System (GNSS) stations (black dots) contributing to the International GNSS Service (IGS) network. The IGS data are provided by regional GNSS networks with stations consisting of a receiver-antenna pairs, continuously recording GNSS data. The IGS analysis centres analyse the data and provides free of charge products such as satellite orbits and clock corrections. The image is in courtesy of NASA/JPL-Caltech and IGS (Dow et al., 2009).*

parameters and maintains the list of stations for the realisation of the International Terrestrial Reference Frame), the RealTime Working Group (dedicated to design and development of the real-time tracking network and products), and the Tide Gauge Benchmark Monitoring Pilot Project (dedicated to analyse data from stations near tide gauges).

2.5.2 Scandinavian Networks and BIFROST

The Swedish permanent GNSS network (SWEPOS) was established in 1993, realised a full operational capability in 1998, and is maintained and operated by the National Land Survey of Sweden (Lantmäteriet) (*Johansson et al.*, 2002). Today SWEPOS consists of 41 reference stations, which are placed on solid bedrock throughout the country (*Engberg et al.*, 2013). Each reference station consists of a concrete pillar with a temperature regulation constant at 15° C. Furthermore, there are about 244 additional SWEPOS stations for densification of the network that are mounted on, e.g., buildings.

In addition to SWEPOS there are other Nordic permanent GNSS networks: the Finnish network maintained by the Finnish Geodetic Institute, FinnRef, was built during the same time as SWEPOS and consists today of 20 permanent reference stations installed on bedrock (*Häkli et al.*, 2013); the Norwegian network, SATREF, started in 1989, is maintained by the Norwegian Land Survey (Statens kartverk), and consists of about 150 stations (of which a few are installed on bedrock) (*Vestol*, 2013); and the Danish network, REFDK, constructed in the beginning of the 1990s with 10 permanent stations, maintained by the Danish Geodata Agency (*Keller et al.*, 2013).

These permanent GNSS networks are used in several research projects, where perhaps the most comprising is the Baseline Inferences for Fennoscandian Rebound Observations Sea Level and Tectonics (BIFROST) project which started in 1993, see e.g., *Johansson et al.* (2002); *Scherneck et al.* (2002); *Lidberg et al.* (2010); *Scherneck et al.* (2010). The goal of the project is to use GNSS observations to determine the three-dimensional movement of the Earth's crust and to use the result in models of GIA in Fennoscandia. In the beginning, the analysis was based on observations from SWEPOS and FinnRef,

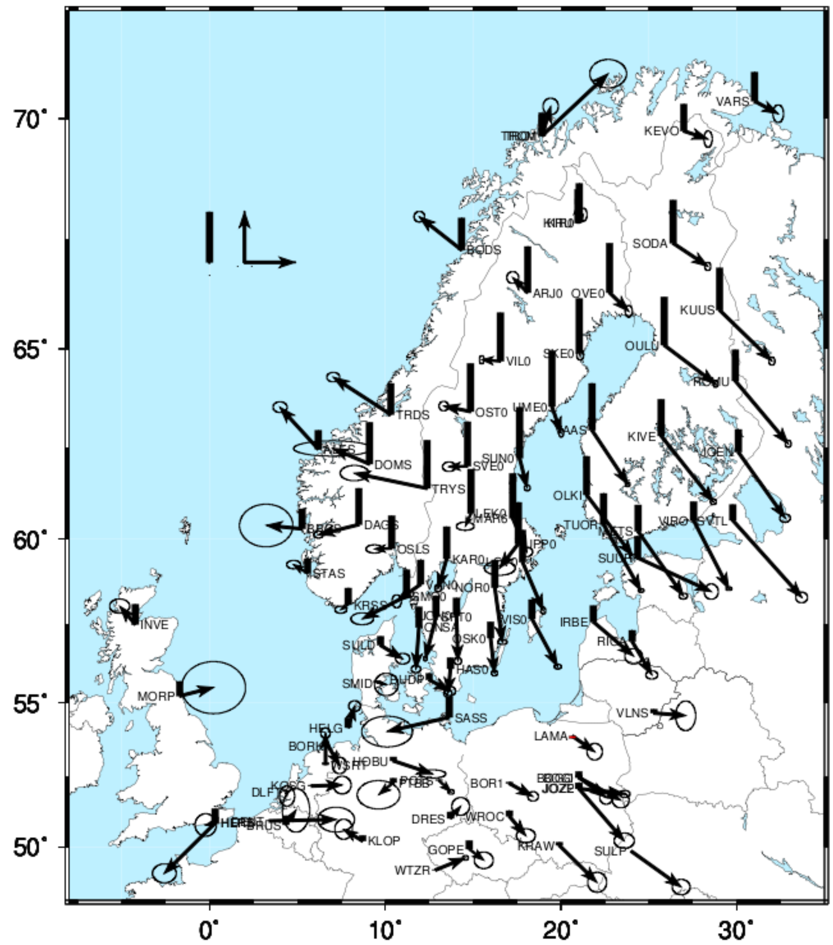

Figure 2.2: *Vertical (bar) and horizontal (arrow) motion in Northern Europe from analysis of GPS data acquired over the period 1996–2006. The legend shows 10 mm/year in the vertical and 1 mm/year in the horizontal component. Data from SWEPOS, FinnRef, SATREF, REFDK, and other northern European GNSS networks are used. The image is in courtesy of Martin Lidberg and can be found in Lidberg et al. (2010).*

but during recent years the network has evolved into using also SATREF, REFDK, and a selection of stations from northern Europe (see *Lidberg et al.*, 2010; *Scherneck et al.*, 2010). As an example of the results obtained with data from SWEPOS and the other European networks, Figure 2.2 show the velocity field (vertical and horizontal motion) in Northern Europe from analysis of GPS data acquired over the period 1996–2006.

3 Reflected GNSS Signals

In many applications, reflected GNSS signals are regarded as something unwanted, e.g, the direct satellite signals reflect off objects in the surroundings of the installation and reach the antenna. These signals then interfere with the direct satellite signals, affect the GNSS observables recorded by the receiver, and reduce the accuracy of the measurements. These reflected signals, or multipath signals, are one of the major error sources in high-accuracy positioning and there are numerous studies in the geodetic community on how to mitigate the effect, e.g., *Georgiadou & Kleusberg* (1988); *Elósegui et al.* (1995); *Hannah* (2001); *Park et al.* (2004); *Bilich et al.* (2008); *Ning et al.* (2011).

However, after the introduction of reflected GNSS signals for remote sensing of the sea level by *Martin-Neira* (1993), the research with reflected GNSS signals, or GNSS Reflectometry (GNSS-R), has evolved into its own field with both ground-based and spaceborne measurements. Examples of GNSS-R include remote sensing of sea level from the ground, e.g, *Anderson* (2000); *Dunne et al.* (2005); *Paper I to V*, and from space, e.g., *Gleason et al.* (2005), soil moisture, e.g, *Larson et al.* (2010), snow depth, e.g., *Larson et al.* (2008, 2009), lake-ice thickness, e.g., *Jacobson* (2010), and locating reflecting objects, e.g., *Benton & Mitchell* (2011).

The common denominator of all the above mentioned examples is of course reflected signals. In this chapter, a general introduction to ***Reflections*** is given, focusing especially on GNSS signals reflected off the sea surface. Concepts like polarisation, reflection coefficients, and reflection surface will be introduced and discussed. In addition, a few comments are made on the effect of surface roughness on the reflected signals.

3.1 Reflections

In order to measure and analyse reflected GNSS signals, it is necessary to investigate how these signals differ from directly received GNSS signals. First, the effect on the signal polarisation from signal reflection from a medium is reviewed using the Fresnel reflection coefficients for specular reflection. Second, the size and shape of the surface contributing to the reflection, approximated by the first Fresnel zone, is studied for different satellite elevation angles. Third, a few notes on the effect on the signal from increasing surface roughness and how this affects the tracking performance of a standard geodetic GNSS receiver.

3.1.1 Signal Polarisation after Reflection

The polarisation of an electromagnetic wave is defined as how the electric and magnetic field propagate in space, e.g., (*Rees*, 2003). Since the electric field is perpendicular to the magnetic field, and both fields are perpendicular to the propagation direction, the components of the electric field is generally used to describe the polarisation.

In order to investigate how the Right-Hand Circularly Polarised (RHCP) GNSS signal is affected from reflection off different media with different electrical properties, the Fresnel reflection coefficients for specular reflection can be used (see e.g., *Rees*, 2003; *Hannah*, 2001). The Fresnel reflection coefficients, for reflection off a non-magnetic media, can for horizontal (Γ_H) and vertical (Γ_V) polarisation be expressed as

$$\Gamma_H = \frac{\sin\theta - \sqrt{\eta - \cos^2\theta}}{\sin\theta + \sqrt{\eta - \cos^2\theta}}; \qquad \Gamma_V = \frac{\eta\,\sin\theta - \sqrt{\eta - \cos^2\theta}}{\eta\,\sin\theta + \sqrt{\eta - \cos^2\theta}} \tag{3.1}$$

where the satellite elevation angle of the incoming wave is denoted θ and the complex dielectric constant is denoted η. The complex dielectric constant depends on the relative dielectric constant η_r (also called relative permittivity), the conductivity of the reflecting medium σ, and the wavelength λ, according to $\eta = \eta_r - j\,60\,\lambda\,\sigma$. Note that both the relative dielectric constant and the conductivity are functions of signal frequency.

Since the GNSS satellite signal is circularly polarised, it is convenient to express the linear reflection coefficients from Equation 3.1 as circular reflection coefficients with a co-polarised (original), Γ_O, and a cross-polarised (opposite), Γ_X, component according to

$$\Gamma_O = \frac{\Gamma_H + \Gamma_V}{2}; \qquad \Gamma_X = \frac{\Gamma_H - \Gamma_V}{2} \tag{3.2}$$

The complex-valued circular reflection coefficients in Equation 3.2, can be used to describe the amplitude and phase of the reflected signal relative to the incident signal. A simulation of the relative magnitude and phase of the circular reflection coefficients (Equation 3.2) for different reflection surfaces is presented in Figure 3.1 (top and bottom, respectively) as co- and cross-polarisation components for different elevation angles. The reflection surfaces used are wet ground, fresh water, and sea water and their respective values of the dielectric constants (30, 80, 20) and conductivity (0.2, 0.2, 4 S/m) are representative for the GPS L_1 frequency (1.575 GHz) and are taken from *ITU* (1992).

The magnitudes of the reflection coefficients, see Figure 3.1 (top), for the different media behave quite similar. The co-polar components decrease with increasing elevation angle, from 1 to 0, whereas the cross-polar components increase with increasing elevation, from 0 to 0.8 (0.7 for wet ground). With different magnitudes of the co- and cross-polar components, the resulting polarisation is elliptic, whereas with equal magnitudes, called the Brewster angle (at about 10.3°, 6.4°, and 8.0° for wet ground, fresh water, and sea water, respectively), the resulting polarisation is linear. This can also be seen in Figure 3.1 (bottom), where the phase of the co- and cross-polar components are equal (this is easiest to see for reflection off sea water), thus the polarisation is linear.

Because of the transmitted RHCP GNSS signal, the co-polar and the cross-polar components can be viewed as RHCP and Left-Hand Circularly Polarised (LHCP) components, respectively. Looking at Figure 3.1 (top), for elevation angles below the Brewster angle, the predominant signal component is the co-polar, or the RHCP, and hence the result is right-hand elliptical polarisation. Conversely, for elevation angles greater than the Brewster angle, the predominant signal component is the cross-polar, or LHCP, and hence the result is left-hand elliptical polarisation. This means that to record GNSS signals reflected off, e.g., the sea surface, at low elevations (i.e., below the Brewster angle), the most feasible approach would be to use an RHCP antenna and contrarily, to record GNSS signals reflected off the sea surface at high elevations (i.e., above the Brewster angle), the most feasible approach would be to use a LHCP antenna.

Another important conclusion from Figure 3.1 (top) is that the magnitude of the LHCP component of the reflected signal is always lower than the RHCP signal before reflection and reaches at maximum 0.7–0.8 (depending on reflection media) for elevation angles closer to 90°.

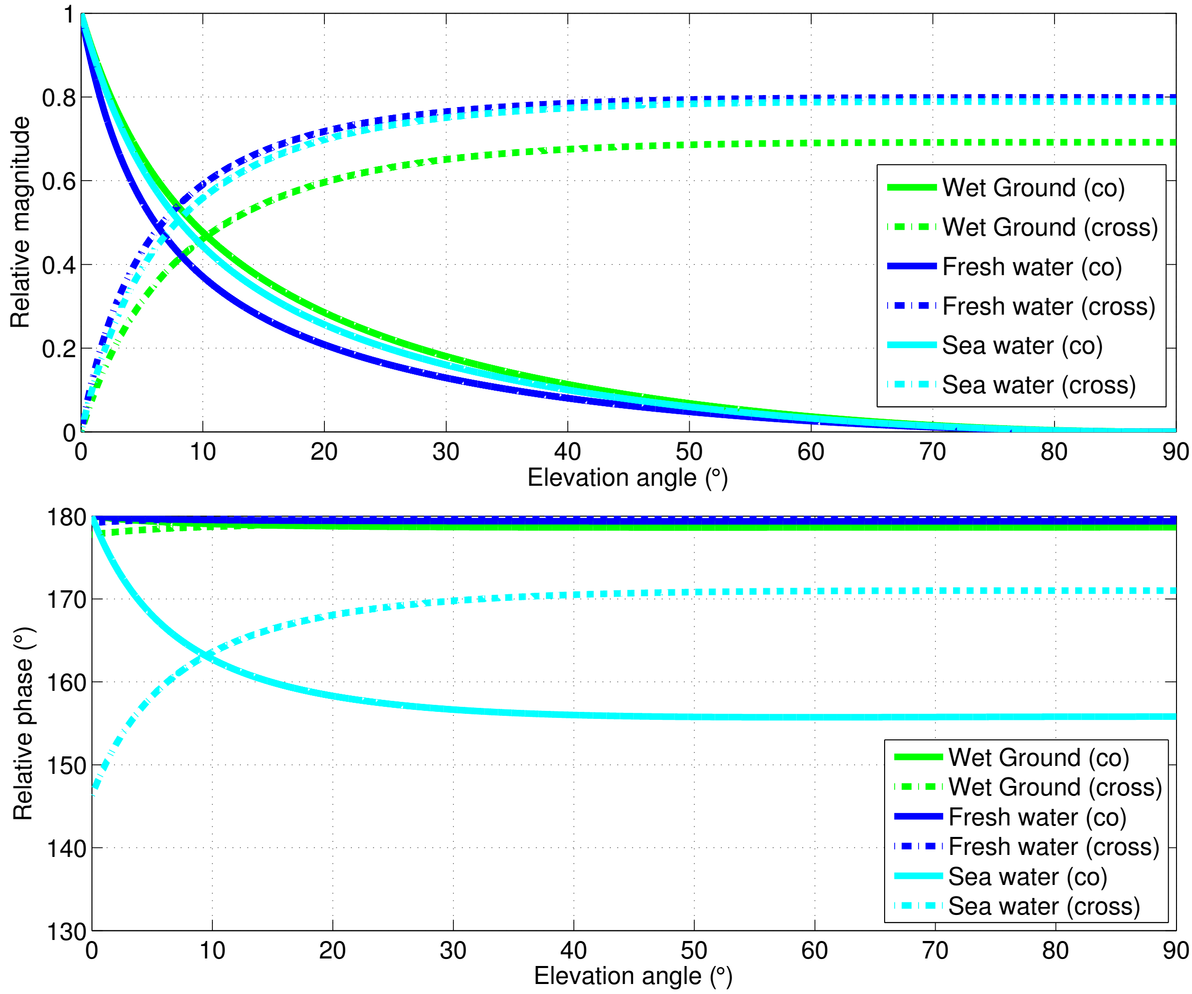

Figure 3.1: *Magnitude (top) and phase (bottom) of the circular Fresnel reflection coefficients for wet ground (green), fresh water (blue), and sea water (cyan), presented as co-polarisation (solid line) and cross-polarisation (dashed line) for the GPS L_1 frequency. Values of the reflection coefficients are relative to the incident wave. The magnitudes of the co-polar components decrease with increasing elevation angle, whereas the cross-polar components instead increase with increasing elevation and dominate for angles larger than the Brewster angle (here between 6.4° and 10.3°). The phase of both the co- and cross-polar components are stable between 177° and 180° for reflection off wet ground and fresh water, whereas for reflection off sea water, the co- and cross-polar components are only equal at the Brewster angle.*

3.1.2 Reflection Surface

Since a GNSS satellite signal illuminates a large region of the surface, the reflection off the sea surface can not be considered to originate from only one single geometric point, the specular point. Instead, reflections from the illuminated area surrounding the specular point will contribute to the total reflected signal. In order to approximate this reflection surface, specular reflection is considered, meaning that both the incident and the reflection angles are equal and lie in the receiver-transmitter plane, the reflection surface is perfectly flat, and the reflected signal power is coherent and governed by the Fresnel equations (see e.g., *Katzberg & Garrison*, 1996; *Masters et al.*, 2004). Based on these assumptions, the reflection area can be described by the first Fresnel zone. The first Fresnel zone, with the specular point in the centre, is defined by a phase change of the signal, across the reflective surface, of less than half the signal wavelength. The semi-major axis (a) and the semi-minor axis (b) of the first Fresnel zone (or

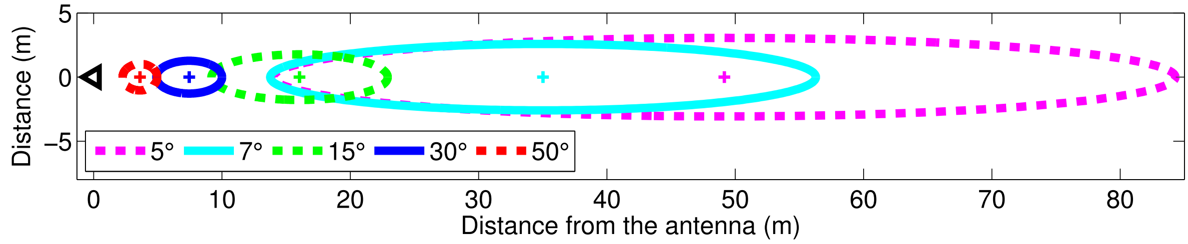

Figure 3.2: *The extent of the reflective surface approximated by the first Fresnel zone for an antenna at height 4.3 m over the surface. The contours describe the reflective surfaces, for GPS observations at frequency L_1, for elevation angles 5° (magenta dashed line), 7° (cyan solid line), 15° (green dashed line), 30° (blue solid line), and 50° (red dashed line). The corresponding areas are 338 m^2, 173 m^2, 38 m^2, 10 m^2, and 4 m^2, respectively. The GPS antenna is represented as a left-pointing triangle, located in the origin, and the specular point for each surface is marked with a plus sign.*

ellipse) can be calculated as

$$a = \frac{\sqrt{\lambda h \sin\theta}}{\sin^2\theta}\,; \qquad b = \frac{\sqrt{\lambda h \sin\theta}}{\sin\theta} \tag{3.3}$$

where the GNSS wavelength is denoted λ, the height of the receiving antenna over the reflector is denoted h, and the elevation angle of the transmitting satellite is denoted θ. As an example of the extent of the reflective surface, Figure 3.2 illustrates the first Fresnel zone for an antenna at height 4.3 m over the reflecting surface for a GPS satellite at elevation angles of 5°, 7°, 15°, 30°, and 50°, transmitting the L_1 frequency.

From Figure 3.2 it is possible to get an idea of the size of the reflective surface for different elevation angles, e.g., a high elevation angle corresponds to a small reflective surface and a low elevation angle corresponds to a large reflective surface. A change in elevation angle at low elevations seems to change the size of the reflective surface more than a change in elevation angle at high elevations, see e.g., Figure 3.2 where the difference in reflection area for elevations 5° to 8° and for elevations 30° to 50° is 165 m^2 and 6 m^2, respectively.

Another way of illustrating the reflective surface is to directly compare the area of the surface ($\pi\, a\, b$) with different antenna heights and for different elevation angles. Simulations of the area of the reflective surface from Equation 3.3 are shown in Figure 3.3 for antenna heights over the surface of 1–10 m and with a GPS satellite at elevation angles of 0.6°–90°, transmitting the L_1 frequency. For ease of viewing, Figure 3.3 is divided into three contour subplots for elevation ranges 0.6°–2.0° (top), 2°–20° (bottom left), and 20°–90° (bottom right) with the area given in m^2. It is clear that for a decrease in the elevation angle or an increase in the antenna height, the size of the reflective surface increases. As seen before, for low elevation angles, Figure 3.3 top and bottom left, the reflecting surface is very large (up to 5000 m^2) compared to high elevation angles, Figure 3.3 bottom right, where the reflecting surface is small (below 1 m^2).

Another important factor regarding the reflective surface is its orientation and ellipticity. The semi-major axis of the elliptic surface extends in the same direction as the vector from the receiving antenna to the sub-satellite point. This means that the reflective surface is continuously moving with the satellite. The ellipticity of the surface is only dependent upon the elevation angle and goes from 0 (circular area) to 1 (extending to infinity) as $e = \cos(\theta)$. This means that for high elevation angles, the reflective area is nearly circular and close to the antenna, whereas for low elevations the area is highly elliptical extending far away from the antenna, see Figure 3.2. Additionally, for observations to multiple GNSS satellites, there are multiple reflective surfaces, that are continuously changing with the satellites changing elevations. These reflective surfaces will at times overlap and cover the same area on the water surface.

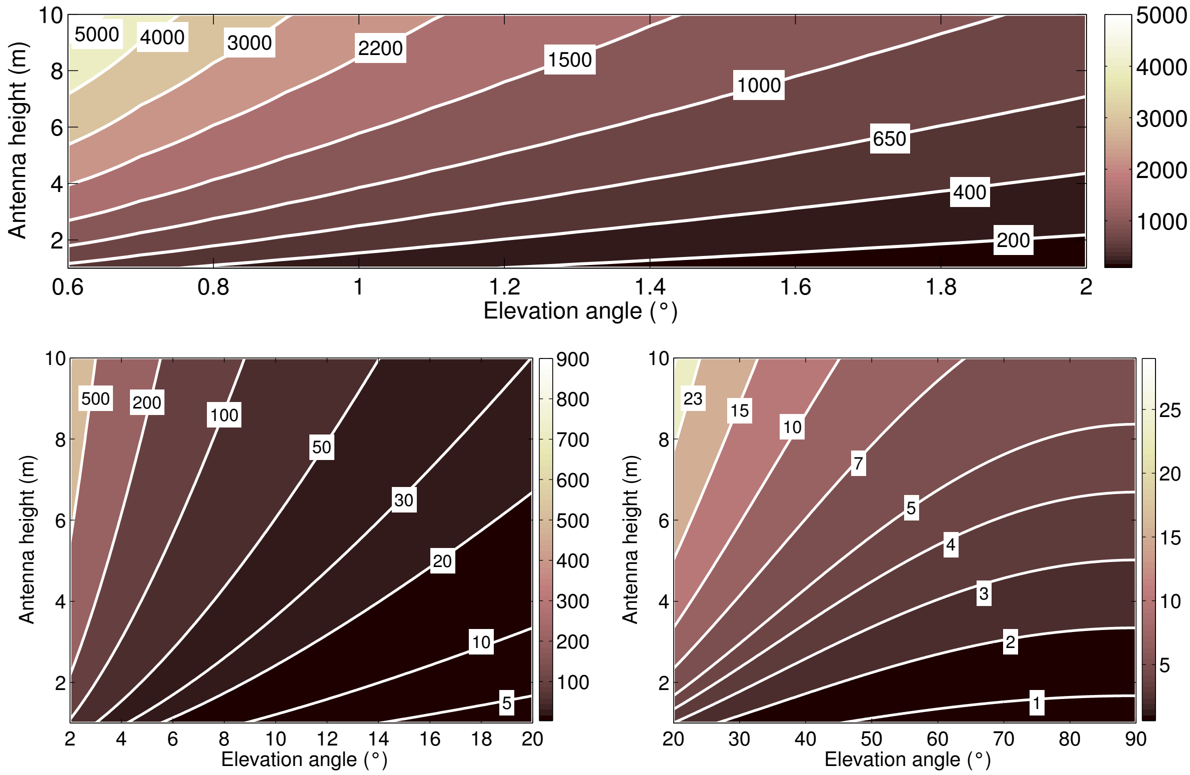

Figure 3.3: *Reflective surface in m^2, approximated by the first Fresnel zone, for observations from a single GPS satellite (frequency L_1) as a function of antenna height over the reflector versus satellite elevation angle. The figure is divided into three contour subplots with the elevation angle ranges of 0.6°–2.0° (top), 2°–20° (bottom left), and 20°–90° (bottom right). To the right of each image is a colorbar showing the contour area range. In addition, white lines indicating equal area are shown with the area value in the figures.*

3.1.3 The Effect of Surface Roughness on the Reflected Signal

For an increasing sea surface roughness, the coherent part of the reflected signal decreases together with an increase in the incoherent part. It is therefore expected that at a certain sea surface roughness, the receivers' tracking loop cannot distinguish the signal from the noise, since the coherent part of the reflected signal is too small (assuming that a standard geodetic GNSS receiver is used to record the reflected signal). As a result, the receiver will lose track of the satellite signal. Examples of this are shown in *Paper II*, where the number of phase observations recorded by the receiver is decreasing for increasing wind speeds (which is correlated with sea surface roughness), and in *Paper V*, as the difference between the GNSS-derived sea level and the tide gauge record increases for increasing wind speeds. Increasing wind speed was in both cases used as an indication for sea surface roughness, since direct measurements of sea surface roughness were not available. This means that the receiver hardware and its internal firmware are limiting factors (at least for a standard geodetic GNSS receiver) for receiving GNSS signals reflected off the sea surface directly.

For an increasing sea surface roughness, it is also expected that the signal after reflection will spread more in space than for specular reflection. This changes the reflection area on the sea surface which will extend to a so-called glistening zone surrounding the specular reflection point (*Katzberg & Garrison*, 1996).

4 GNSS Reflectometry

The field of GNSS Reflectometry (GNSS-R) started with a proposal by *Martin-Neira* (1993) to use the freely available GNSS signals for remote sensing of the sea level. The idea was to record both the direct GNSS signals and the GNSS signals that are reflected off the sea surface in order to measure the sea level. Following this idea, there have been numerous of different methods and techniques for using the reflected GNSS signals for sea level observations from ground-based platforms (e.g. *Anderson*, 2000; *Martin-Neira et al.*, 2002; *Dunne et al.*, 2005; *Larson et al.*, 2013; *Nakashima & Heki*, 2013, *Paper I to V)*, from airborne platforms (e.g., *Garrison et al.*, 1998; *Lowe et al.*, 2002a; *Cardellach et al.*, 2013), and from spaceborne platforms (*Lowe et al.*, 2002b; *Gleason et al.*, 2005).

This thesis is focused on using standard geodetic commercially off-the-shelf GNSS equipment for recording both the direct satellite signals and the satellite signals that are reflected off the sea surface. The GNSS signals are recorded by a so-called GNSS tide gauge, which is a rather broad concept including both one and multi-antennae installations and analysis of code, phase-delay or Signal-to-Noise Ratio (SNR) data (e.g., *Anderson*, 2000; *Martin-Neira et al.*, 2002; *Dunne et al.*, 2005; *Rivas & Martin-Neira*, 2006; *Caparrini et al.*, 2007, *Paper I to V)*. The GNSS tide gauge can in theory actually be any GNSS installation close to the ocean.

The GNSS tide gauge presented in this thesis builds upon the concept of bistatic radar measurements at L-band to estimate the local sea level. Each GNSS satellite broadcasts carrier signals that are received both directly and after reflection off the sea surface. Two standard geodetic-type two-frequency GNSS receivers are used to track and record the direct and the reflected signals. These data, either from both receivers or from one of the receivers, are analysed in post-processing or near real-time to extract sea level information.

In this chapter, ***The GNSS Tide Gauge*** will be introduced and described in detail. This will be done both by explaining the concept, connecting to Chapter 3 with reflected signals, and by presenting two different techniques, recording the signals with one or two antennae, and the respective analysis methods, ***Phase-Delay Analysis*** and ***SNR-Analysis***.

4.1 The GNSS Tide Gauge

The GNSS tide gauge consists of two antennae mounted back-to-back, preferably aligned along a local vertical, on a beam extending out over the coast line. One of the antennae is Right-Hand Circularly Polarised (RHCP) and zenith-looking, receiving the direct GNSS signals in the main lobe of the antenna radiation pattern, see Figure 4.1. Solving for the position of this antenna results in land surface height with respect to the International Terrestrial Reference Frame (ITRF), i.e., the position with respect to the Earth's centre of mass. This is similar to what is continuously done for stations in national and international permanent GNSS networks, e.g, the Swedish permanent GNSS network (SWEPOS) and

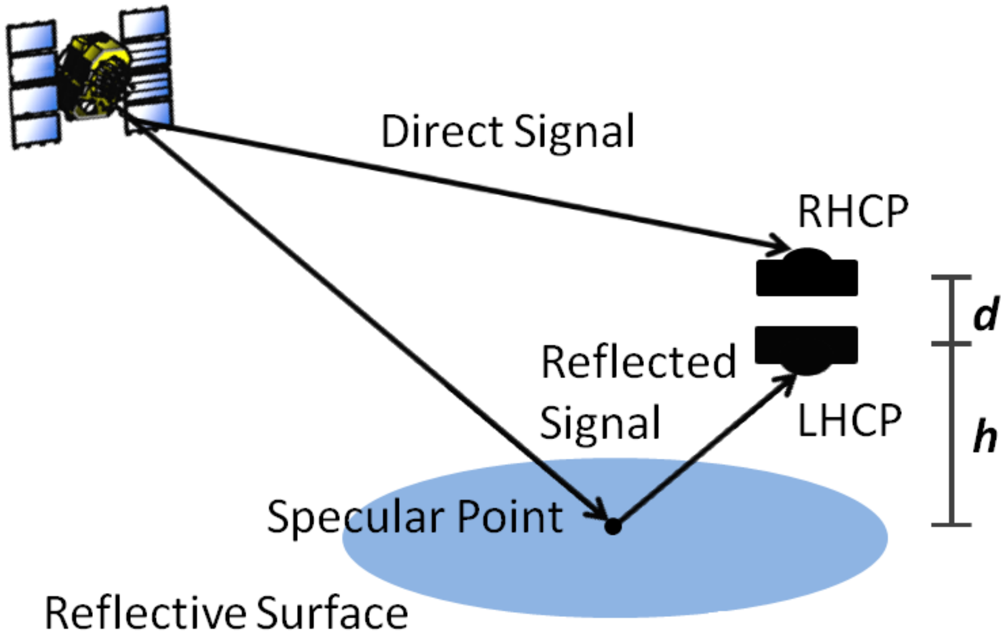

Figure 4.1: *Schematic drawing of the bistatic radar concept and the GNSS tide gauge. The GNSS satellite transmits a Right-Hand Circularly Polarised (RHCP) signal which is received both directly, by the upward-looking RHCP antenna, and after reflection off the sea surface, when the signal changes polarisation to dominantly Left-Hand Circular Polarisation (LHCP) or actually left-hand elliptical polarisation, by the downward-looking LHCP antenna. In addition, a portion of the reflected signal reaches the back of the RHCP antenna, interferes with the direct signal, and affects the recorded data. This multipath effect is strongest for satellite observations from low elevation angles. Solving for the positions of the two antennae allow for sea level height with respect to the International Terrestrial Reference Frame and using the multipath affected data it is possible to determine the sea level height with respect to the RHCP antenna.*

the International GNSS Service (IGS), see Section 2.5.

The other antenna is Left-Hand Circularly Polarised (LHCP) and nadir-looking, facing the sea surface and receiving the GNSS signals that have reflected off the sea surface in the antenna main lobe (see Figure 4.1). From Section 3.1.1 we know that when the GNSS satellites' RHCP signals reflects off the sea surface the polarisation changes into dominantly LHCP, or at least Left-Hand Elliptical Polarisation (LHEP), for satellite elevation angles larger than about 8°.

For the GNSS tide gauge there are simultaneous observations from multiple satellites with different elevation and azimuth directions at each epoch. Since the total reflective surface consists of overlapping individual elliptic area from several satellite observations distributed over the sea surface (they can also be overlapping), the total surface will continuously change its size, see Section 3.1.2. In addition, changes in sea level due to tides and meteorological forcing (can be seen as changes in antenna height in Figure 4.1), will also affect the size of the reflective surface.

As described, the GNSS tide gauge installation is constructed to receive the direct GNSS signals with the upward-looking RHCP antenna, in the same way as a geodetic GNSS station in order to be able to solve for an accurate position with respect to the ITRF, and to maximise the number of received reflected GNSS signals with the downward-looking LHCP antenna. The sea level height can then be derived by solving for the position of the LHCP antenna, since the reflection occurs at different heights depending on the sea level height. Combining both measurements results in sea level with respect to the ITRF.

The antennae will not only receive signals through the front or the main lobe, they will also receive a portion of the signals through the back or through side lobes. For example, the direct GNSS signal reaches the RHCP antenna, but at the same time a portion of the direct signal has reflected off the sea surface and reaches the back side of the RHCP antenna. This multipath signal interferes with the direct signal and affects the recorded data. The effect is of course highly dependent on the antenna radiation pattern, and for geodetic GNSS antennae, the effect is strongest for satellite observations from low elevation angles. Multipath signals are often seen as an error source, however, in this case it opens up another possibility of measuring the sea level with an antenna that is oriented away from the actual object of interest. Analysis of the multipath affected data results in sea level height with respect to the RHCP antenna. Combining the sea level height with the position of the RHCP antenna with respect to the ITRF results in sea level with respect to the ITRF.

4.2 Phase-Delay Analysis

The concept of phase-delay analysis with the GNSS tide gauge is similar to that of high-accuracy positioning with GNSS, i.e., determine the position of the two antennae or actually the distance between them (the baseline). The zenith-looking RHCP antenna is connected to a standard geodetic GNSS receiver, recording the phase-delay of the direct GNSS signals. After reflection off the sea surface, the RHCP satellite signals change polarisation into dominantly LHCP, or LHEP, for observations from satellite elevation angles of over 8° (see reflection coefficients in Section 3.1.1). The phase-delay of the reflected LHCP signals are then recorded by a standard geodetic GNSS receiver connected to the nadir-looking LHCP antenna.

Since the reflected signals experience an additional path delay compared to the directly received signals, the nadir-looking antenna will appear to be a virtual zenith-looking antenna located below the sea surface, see Figure 4.2. The position of this virtual antenna will be at the same distance below the sea surface as the actual LHCP antenna is located above the sea surface.

With a vertical change in the sea surface, the additional path delay of the reflected signals changes. Hence, the LHCP antenna appears to change its vertical position. This means that the height of the nadir-looking antenna over the sea surface h_a is directly proportional to the sea surface height. Utilising the geometry in Figure 4.2, h_a can easily be related to the vertical baseline between the two antennae Δv according to

$$\Delta v = 2\,h_a + d \tag{4.1}$$

where d is the vertical separation of the phase centres of the two antennas and θ is the satellite elevation angle. This means that with the GNSS tide gauge, it is possible to monitor both changes in land surface height with respect to the ITRF, with the zenith-looking antenna, and changes in sea surface height, with the nadir-looking antenna. Additionally, by combining measurements from both antennas, local sea level with respect to the ITRF can be obtained.

4.2.1 Positioning Using Phase-Delay Observations

In order to discuss analysis of GNSS phase-delay data, there is a need to recapitulate a few ideas from Chapter 2. The GNSS observation is basically a measurement of travel time, which makes the process highly dependent on accurate clocks. Furthermore, the desired receiver position is determined towards multiple satellites, meaning that it is crucial to have precise satellite orbits for a highly accurate determination of the receiver position. With this in mind, there are several ways to analyse GNSS phase-delay data, see e.g., *Blewitt* (1997); *Hofmann-Wellenhof* (2001). To start with, recall the GNSS

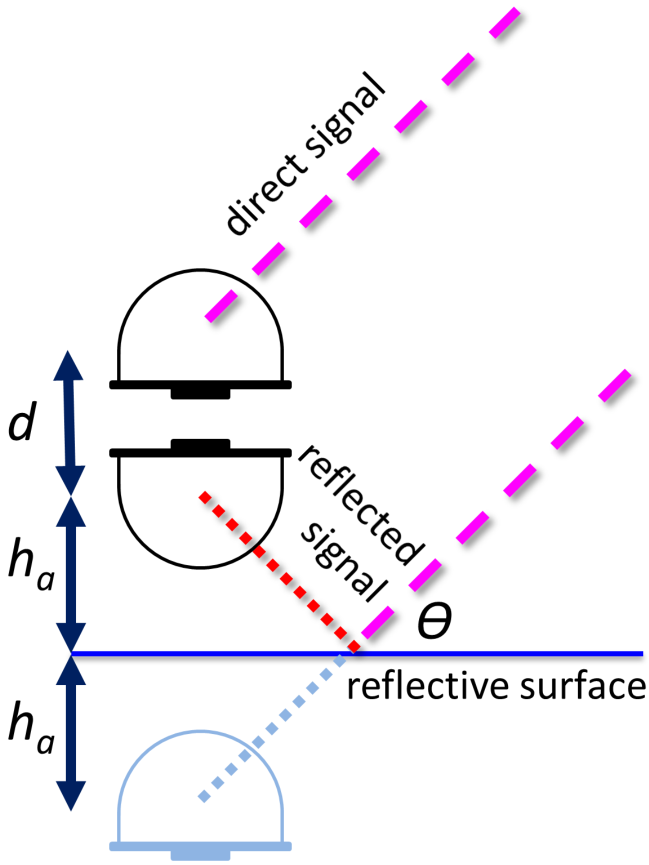

Figure 4.2: *Schematic drawing of the GNSS tide gauge for the phase-delay analysis. The phase-delay of the direct and the reflected signal are recorded separately by a receiver connected to the Right-Hand Circularly Polarised (RHCP) zenith-looking antenna and a receiver connected to the Left-Hand Circularly Polarised (LHCP) nadir-looking antenna, respectively. The RHCP satellite signals change polarisation to LHCP after reflection. Through geodetic analysis of the phase-delay, the baseline between the antennae can be determined and related to the height of the nadir-looking antenna over the sea surface, h_a, and the vertical distance between the antenna phase centres, d. Since h_a is directly proportional to the sea surface height and it is straight forward to determine the position of the zenith-looking antenna with respect to the International Terrestrial Reference Frame (ITRF), from the GNSS tide gauge it is possible to achieve local sea level with respect to the ITRF. Other figures explaining the concept can be found in Paper I, II, and V.*

phase observation equation (Equation 2.1), modeling the phase-delay measurement as a function of the geometric range to the satellites, signal propagation effects in the atmosphere, clock biases for both the receiver and the satellites, and phase ambiguity parameters for each satellite. Solving for a single receiver position with Equation 2.1, means that a large number of parameters need to be estimated. Hence, this implies that an even larger number of observations is required for an accurate determination. This is possible using the Precise Point Positioning (PPP) strategy (*Zumberge et al.*, 1997), but in a situation where the number of observations is limited, e.g., a GNSS tide gauge with reflections from the sea surface, the results are often not satisfying. Another way would be to do a differential analysis, i.e., combining several satellite observations and solving for the baseline between two receivers, which can remove several unknowns during certain circumstances (*Blewitt*, 1997).

Differential solutions can be formed in several ways. To start with, first consider the GNSS observation equation (Equation 2.1) for two different receivers, denoted by subscript A and B, with observations to the same satellite, denoted by superscript j,

$$L_A^j = \rho_A^j + c\,(\tau_A - \tau^j) + Z_A^j - I_A^j + B_A^j + \epsilon \tag{4.2a}$$
$$L_B^j = \rho_B^j + c\,(\tau_B - \tau^j) + Z_B^j - I_B^j + B_B^j + \epsilon \tag{4.2b}$$

with the same parameter notation as in Equation 2.1 except for L_n^j and B_n^j, which are the observed carrier phase measurements $L_n^j = \lambda\,\Phi_n^j$ and the phase ambiguity parameters ($B_n^j = \lambda\,N_n^j$) in metres from receiver n, respectively. By taking the difference between Equation 4.2a and Equation 4.2b, the single difference phase equation for each epoch, ΔL_{AB}^j, is formed as

$$\Delta L_{AB}^j = \Delta\rho_{AB}^j + c\Delta\tau_{AB} + \Delta Z_{AB}^j - \Delta I_{AB}^j + \Delta B_{AB}^j \tag{4.3}$$

where the difference between the two receivers is denoted by Δ and double subscript. Assuming that the satellite clock biases, τ^j, are identical for simultaneous observations to the same satellite, the differential satellite clock bias term is left out from Equation 4.3 (*Blewitt*, 1997). Additionally, for shorter receiver separations, the differential terms for the neutral atmosphere (the troposphere), ΔZ^j, and the ionosphere, ΔI^j, cancel out. For single differencing the tropospheric component can usually be ignored for receiver separations of less than 30 km and the ionospheric component for separations of less that 1–30 km, depending on ionospheric conditions. With these assumptions, the observation equation for each epoch simplifies to

$$\Delta L_{AB}^j = \Delta\rho_{AB}^j + c\Delta\tau_{AB} + \Delta B_{AB}^j \tag{4.4}$$

containing the measured carrier phase differences between the two receivers expressed in metres, ΔL_{AB}^j, the differences in geometry or baseline between the receivers, $\Delta\rho_{AB}^j$, the receiver clock bias differences, $\Delta\tau_{AB}$, and the phase ambiguity parameter differences, ΔB_{AB}^j.

The term for the difference in geometry in Equation 4.4, can be expanded and expressed in a local coordinate system using the azimuth, α, and elevation, θ, angle for each satellite according to

$$\Delta\rho_{AB}^j = \Delta e\,sin(\alpha^j)\,cos(\theta^j) + \Delta n\,cos(\alpha^j)\,cos(\theta^j) + \Delta v\,sin(\theta^j) \tag{4.5}$$

where Δe, Δn, and Δv are the east, north, and vertical components of the baseline between the two receivers, respectively. If the horizontal baseline is known, both the east and north baseline component can be moved to the left side of Equation 4.4, reducing the number of unknowns in the analysis. If the horizontal baseline is zero, the east and north contribution can be disregarded.

Taking the difference between two receivers (A and B) and two satellites, denoted by superscript j and k, forms the double difference phase observation for each epoch $\nabla\Delta L_{AB}^{jk}$. This is the same as taking the difference between two single difference observations, i.e., the difference between Equation 4.3 for two satellites (or the difference between Equation 4.4 for two satellites assuming a short baseline) and results in

$$\nabla\Delta L_{AB}^{jk} = \nabla\Delta\rho_{AB}^{jk} + \nabla\Delta B_{AB}^{jk} \tag{4.6}$$

where the double differenced parameters are denoted by ∇ and double superscript. Since a short baseline is assumed, the double differenced terms for the troposphere, $\nabla\Delta Z^j$, and the ionosphere, $\nabla\Delta I^j$, are left out of Equation 4.6. However, systematic effects due to unmodeled atmospheric errors increase slightly for double differences as compared to single differences (*Blewitt*, 1997). The same holds true for random errors, e.g., from measurement noise and multipath. On the other hand, the satellite clock bias cancels out for double differences (left out of Equation 4.6), which would create much larger errors. In addition, the double difference equation is especially advantageous for GPS observations (and other systems using code division multiple access to separate between satellites), since the double differenced phase ambiguity parameters become integers. This can be achieved in the analysis with integer ambiguity resolution, i.e., resolving the unknown cycle ambiguity of each double differenced observation, e.g., using the Least-squares AMBiguity Decorrelation Adjustment (LAMBDA) method developed by *Teunissen* (1993). Integer ambiguities are not the case for double differenced GLONASS observations, since the visible satellites have different carrier frequencies.

For short baselines, the double differenced geometry in a local coordinate system, $\nabla\Delta\rho_{AB}^{jk}$, can easily be obtained by taking the difference between the single difference geometry for two satellites, i.e., the difference between Equation 4.5 for two satellites.

It is also possible to form additional differences to Equation 4.6, e.g., triple differences (between double differences at different epochs). For triple differences the ambiguity parameters are eliminated if the parameters have not changed between epochs and if they have changed they will appear as outliers. The disadvantage with triple differences is that the precision is reduced due to correlations between observations in time (*Blewitt*, 1997).

4.2.2 GNSS Software Packages

There are currently several software packages available for processing of GNSS phase-delay data using the equations presented in Section 4.2.1, e.g., the GNSS-Inferred Positioning SYstem and Orbit Analysis SImulation Software (GIPSY-OASIS) version 6.2 (*Zumberge et al.*, 1997), the Bernese GNSS Software version 5.2 (*Dach et al.*, 2007), and GAMIT-GLOBK version 10.4 (*Herring et al.*, 2010). All three are extensive processing packages that have been developed during several years from processing of static GNSS data to include processing of kinematic datasets. Today they are used all over the world for continuous processing of permanent GNSS networks and for various GNSS research projects.

Even though these GNSS software packages are all very extensive, there are some applications where they cannot be used with full satisfaction. As previously mentioned, the GNSS tide gauge dataset is somewhat different from traditional geodetic datasets. The setup is basically a kinematic situation: the reflective surface is moving, implying that the nadir-looking antenna, in a data analysis sense, is moving. In addition, the reflected signals have lower SNR than the direct signals and with the desired reflections only originating from satellites in the sea surface direction, and not from the full hemisphere, the number of observations are reduced. Furthermore, since the reflective surface is ever-changing, the coherent part of the reflected signal varies and this results in a higher number of cycle slips and disruptions in the signal reception, than in the traditional geodetic case.

In the mentioned setup, a customised processing strategy could thus be more beneficial. Designing the software for a specific situation would provide full insight to the processing and the possibility to easily review each step. In addition, developing your own software secures a high level of independence and flexibility.

4.2.3 Data Analysis of Phase-Delay Observations

In Section 4.2.1, different phase-delay analysis methods were discussed, presenting single and double difference equations (Equation 4.4 and 4.6, respectively). In this chapter, the phase-delay analysis will be discussed from a more practical point of view, highlighting some ideas that can be of advantage in the analysis, and taking examples from *Paper I, II, and V.*

Before the analysis, it is of importance to assure the data from the reflected signals (received with the LHCP antenna) originate from the sea surface and not from other reflectors. This can be done with a simulation of the size of the reflective surface, approximated by the first Fresnel zone (see Section 3.1.2), and comparison of the results to the geometry at the site in order to determine suitable azimuth angles for analysis. A matter of equal importance is which elevation angles that should be considered in the analysis. In Section 3.1.1, it was determined that for higher elevation angles than 8°, the amplitude of the LHCP component of the reflected signal was stronger than the RHCP component. Since the nadir-looking antenna of the GNSS tide gauge is LHCP, it can therefore be argued that the elevation angles to use in the phase-delay analysis should at least be higher than 8°. However, it is known that for lower elevations, the effect of multipath signals, interfering with the direct signals, is the highest (see e.g, *Georgiadou & Kleusberg*, 1988; *Elósegui et al.*, 1995). This was also seen in the SNR data recorded for *Paper I* (see Figure 5). In order to reduce the multipath effect, it can therefore be beneficial to avoid analysis of data from observations with low elevation angles. For example, in *Paper I and II*, only data recorded from satellites with elevation angles of over 20° was analysed. Using another GNSS tide gauge installation, the elevation limit was set to 15°, see *Paper V*.

For continuous observations of multiple satellites during several epochs, the differenced observations (Equation 4.4 and 4.6) can be expressed as a linear system of equations, $D\,x = y + \epsilon$, consisting of the vector, y, of observed differenced phase measurements; the vector, ϵ, containing the unmodeled effects and the measurement noise; the design matrix, D, containing partial derivatives for the vertical baseline, the phase ambiguity parameters, and the differences in the receiver clock bias (for single differences); and the vector, x, containing the estimated parameters for the baseline, the phase ambiguity parameters, and the differences in clock bias (for single differences).

When solving the linear system of equations using least-squares, there is no need for estimating all the parameters at every epoch. This is of course dependent on the dataset and the application (static or kinematic), but there are some general constraints that can be applied in the analysis. The phase ambiguity parameters will remain the same for any given satellite or satellite pair as long as the receivers have continuous track of that satellite or satellite pair. However, if the receivers lose track, e.g., due to signal obstruction or excessive noise, a new ambiguity parameter has to be estimated. The differences in receiver clock bias for single differences, on the other hand, is unpredictable and needs to be estimated every epoch. For static analysis, the baseline components remain the same each epoch, whereas for kinematic processing the components are estimated at every epoch or with another temporal resolution depending on the application.

The primary phase-delay analysis that has been included in this thesis is with single differences (see Equation 4.4). There are two main reasons for this. First, one extra observation is needed to form double differences as compared to single differences and for our configuration with reflected signals, the number of observations is limited. Second, the goal has always been to analyse GNSS data, i.e., data from GPS and GLONASS (and additional GNSS), using the same models, and since GLONASS satellites have different carrier frequencies, it is not possible to solve for integer ambiguities.

The sea level is obviously kinematic, i.e., it is moving continuously. However, because of the limited number of (reflected) observations from the sea surface, it is useful to limit the number of parameters that needs to be estimated each epoch. One example is the vertical baseline between the antennae, see Equation 4.5. In order to reduce the number of unknowns, the tide gauge installation can be constructed so that the antennae are aligned horizontally and thus the horizontal components of the baseline become zero ($\delta e = \delta n = 0$). A useful assumption is that the sea level is static during a shorter time period, i.e., the sea level is not moving vertically during a period of a few minutes to a few tens of minutes, and one vertical component can be estimated during this time. For the phase-delay analysis in *Paper I, II, and V*, one vertical baseline (or static sea level) has been estimated during the time interval of 20 min. If a higher temporal resolution of the sea level is desired, it is possible to first analyse the sea level as static during, e.g., 20 min, and then re-analyse the sea level, using the ambiguity parameters from the static solution, for a wanted temporal resolution up to the sampling rate of the GNSS data, see e.g., *Löfgren et al.* (2010).

Assuming that the phase centres of the antennae are aligned horizontally, or that the horizontal distance is known, simplifies the analysis. However, in order to assure this, the phase centre variations of the antennae need to be included in the analysis. The antenna phase centre variations can account for several mm in the line of sight for the GNSS observations for each antenna. These phase centre variations have not yet been included in the phase-delay analysis software used in *Paper I, II and V*.

As mentioned before, it can be beneficial to use double difference analysis for GPS data. There are several methods to fix the ambiguity parameters to integers in the double difference analysis. One of the more advantageous methods is the LAMBDA method, see *Teunissen* (1993, 1994, 1995). The procedure for analysis using ambiguity fixing with the LAMBDA method can be described in three steps. First, a least-squares solution of Equation 4.6, estimating the ambiguity parameters as floats. Second, the float ambiguities are adjusted to integers with the LAMBDA method, using a re-parametrisation of the ambiguities and third, the least-squares solution is fixed using the integer ambiguities.

4.3 SNR-Analysis

GNSS antennae are designed to be sensitive to the direct RHCP satellite signals. This is achieved by the antenna radiation pattern focusing the antenna gain for RHCP signals towards zenith and decreasing the gain with decreasing elevation angle, see e.g. the radiation pattern for Leica AR25 (*Bedford et al.*, 2009). In parallel, the sensitivity for LHCP signals from the sky is reduced by about 13–23 dB, compared to the zenith gain for RHCP signals. At the same time, the antennae are designed to suppress unwanted signals from below the horizon, so-called multipath, which are signals that are reflected in the surrounding environment before reaching the antenna. For signals from below the horizon (negative elevation angles), the antenna gain is always 9 dB less than at zenith direction, and it is decreasing with decreasing elevation angle (towards –90°). In addition, at small negative elevation angles (0° to –30°), the RHCP gain is 2–7 dB larger than the LHCP gain.

Despite the design efforts to suppress signals from below the horizon, a portion of the direct signals reflects off the surroundings of the installation and reaches the antenna, see Figure. 4.3. These multipath signals interfere with the direct signals and affect the GNSS observables recorded by the receiver. This is one of the major error sources in high-accuracy positioning with GNSS and there are numerous studies on how to model and mitigate the effect, e.g., *Georgiadou & Kleusberg* (1988); *Elósegui et al.* (1995); *Hannah* (2001); *Park et al.* (2004); *Bilich et al.* (2008); *Ning et al.* (2011).

The multipath interference is created by the phase difference in the receiver between the direct and the reflected satellite signal. This phase difference changes when the satellite moves across the sky, creating an interference pattern. All GNSS observables are affected, but the interference pattern is especially visible as oscillations in the recorded SNR. From the frequency of these multipath oscillations, it is possible to derive the distance between the horizontal reflector and the antenna phase centre, called the reflector height. This means that for the data from the zenith-looking antenna of the GNSS tide gauge, or for data from any zenith-looking GNSS antenna close to the ocean, it is possible to derive the distance to the sea surface, see Figure 4.3. Furthermore, this distance is anticorrelated with the sea level height.

The connection between multipath oscillations of the recorded SNR and the reflector height has been known since the 1980s, see e.g., *Bishop et al.* (1985); *Georgiadou & Kleusberg* (1988). However, it was *Anderson* (1995), see also *Anderson* (1996, 2000), who associated the SNR oscillations with sea level observations using a tilted GPS antenna. The method was later further developed for remote sensing of the environment close to the antenna, e.g., for sensing soil moisture (*Bilich et al.*, 2007; *Larson et al.*, 2008), snow depth (*Larson et al.*, 2009), locating reflecting objects (*Benton & Mitchell*, 2011), and sea level (*Larson et al.*, 2013, ; *Paper III, IV, and V*).

4.3.1 Reflector Height from Recorded SNR

Multipath signals contaminate the recorded GNSS observables since the receiver tracking loop locks onto the composite signals consisting of the direct and the reflected satellite signal, see e.g., Figure 4.3. The effect can be clearly seen in the recorded SNR data, which are the raw signal strengths or the SNR values from the receiver for the phase observations (*Gurtner & Estey*, 2013), and can be related to the multipath environment. This means that SNR is a scaled version of signal amplitude, assuming a constant noise level, that is usually derived from the carrier tracking loop of the GNSS receiver. The tracking loop can be described, according to *Ward* (1996) (see also e.g., *Georgiadou & Kleusberg*, 1988; *Bilich et al.*, 2007) as the phase relationship between the in-phase (I) and the quadrature (Q) channels, see Figure 4.4.

In a multipath-free situation, the phasor diagram (see Figure 4.4) contains only the contribution from the direct signal, i.e., the single phasor of amplitude A_d, which is equivalent to the SNR. The

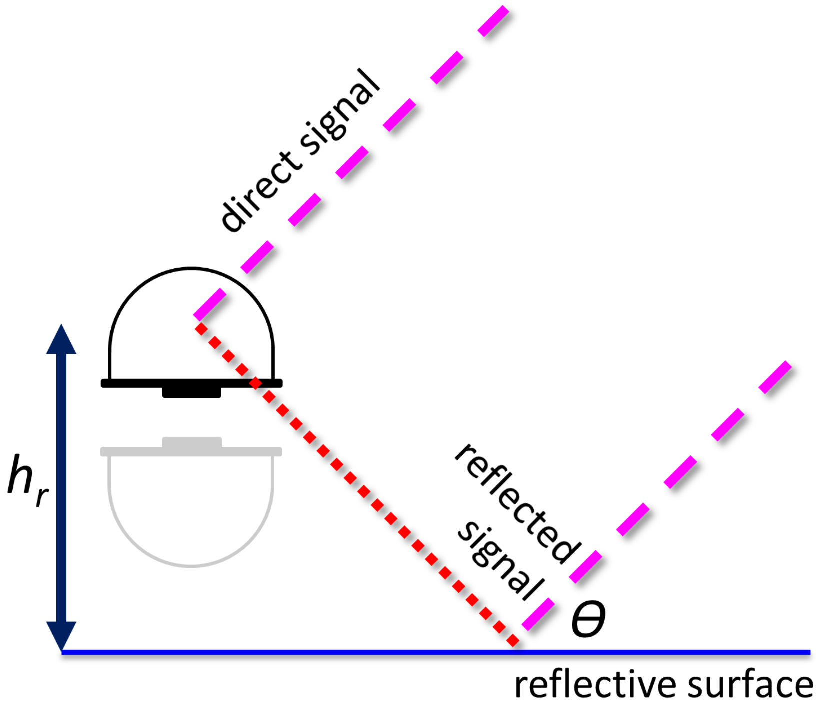

Figure 4.3: *Schematic drawing of the GNSS tide gauge for the Signal-to-Noise Ratio (SNR) analysis. The GNSS signal from the satellite is directly received by the antenna for elevation θ. Additionally, the satellite signal is reflected off the sea surface before reaching the antenna. The reflected signal, or multipath signal, interferes with the direct signal, affecting the recorded observables. This effect is especially visible in the recorded SNR as oscillations. From the frequency of these multipath oscillations it is possible to derive the distance between the antenna phase centre and the reflector, i.e., the reflector height h_r. The reflector height is anticorrelated with the sea level height. Other figures explaining the concept can be found in Paper III, IV, and V.*

carrier phase is measured by the phase angle ϕ_d, which is nonzero if the local and incoming phase angle are misaligned. With multipath present, one or multiple additional phasors are added to the diagram. Here the multipath phasor, or reflected signal phasor, is described by the amplitude A_r and the multipath relative phase angle ψ (relative to the phase angle of the direct signal phasor), which is directly related to the geometry. With the additional signal, the receiver tracking loop attempts to track the composite signal with amplitude A_c and phase angle ϕ_c. The composite signal is the vector sum of all phasors, containing both the direct and reflected signal, implying that the SNR is equivalent to the composite signal amplitude. Using a simplified model for GNSS signal tracking, with one direct signal and one signal reflected off the smooth planar surface (specular reflection), the composite SNR and the phase error $\delta\phi = \phi_c - \phi_d$, originating from tracking with the additional multipath signal as compared to tracking only the direct signal, can be expressed through the law of cosine and geometric relationships in Figure 4.4 as

$$\tan(\delta\phi) = \frac{A_r \sin(\psi)}{A_d + A_r \cos(\psi)} \tag{4.7a}$$

$$SNR^2 = A_c^2 = A_d^2 + A_r^2 + 2\, A_d\, A_r \cos(\psi) \tag{4.7b}$$

When a GNSS satellite moves across the sky, the reflection geometry changes. This implies that the phase difference between the direct and the reflected signal changes and from Equation 4.7b it is evident

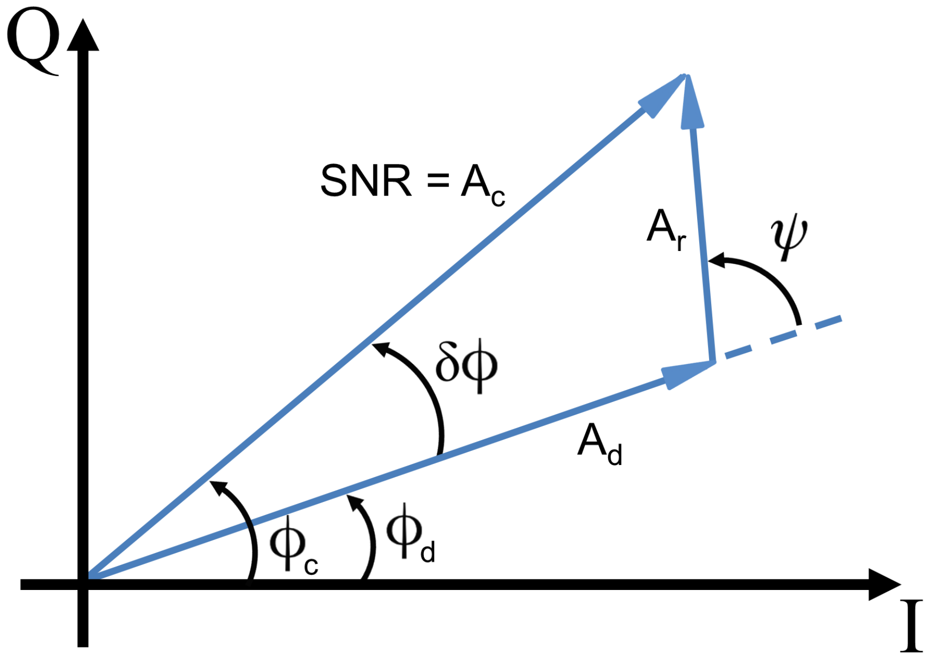

Figure 4.4: *The carrier tracking loop of a GNSS receiver presented as a phasor diagram, illustrating the relationship between the in-phase (I) and quadrature (Q) channels. During conditions with no multipath, the phasor diagram contains only the direct signal of amplitude A_d and phase ϕ_d and the SNR measurement is equivalent to A_d. With multipath present, the additional phasor from the reflected signal with amplitude A_r and phase angle ψ (relative to ϕ_d), is added. With the additional signal, the receiver records the composite signal with amplitude A_c and phase ϕ_c, which will bias the phase measurement by $\delta\phi$. Moreover, the SNR measurement is equivalent to the amplitude of the composite signal. The figure is inspired by Figure 1 in Bilich et al. (2007).*

that the amplitude of the SNR changes, creating an interference pattern. Note that the amplitudes in Equation 4.7b are affected by the antenna gain pattern. As previously mentioned, the direct signal is preferred more by the antenna gain pattern than the reflected signal and in addition the reflected signal is attenuated upon reflection, see Section 3.1.1, which makes $A_d \gg A_r$. The means that since A_d is large in magnitude, the overall magnitude of the SNR should be large, and slowly varying, during a satellite pass. Furthermore, the multipath contribution should have a small amplitude, but vary oscillatory. Moreover, the magnitude of the reflected signal is highly affected by the reflective surface and the satellite elevation angle, see e.g., Figure. 3.1 top, illustrating the magnitudes for reflection coefficients with reflection from different media. Considering that the antenna gain pattern prefers the RHCP signals more than the LHCP signals for small negative elevation angles, i.e., for specular reflections from satellite signals with elevation angle of about 0° to 30°, the dominant part of A_r is from RHCP signals. From Figure. 3.1 (top), the RHCP reflection coefficients for these elevations are rapidly decreasing with increasing elevation. This implies that A_r decreases with increasing elevation and also that the amplitude of the multipath oscillations in the SNR will decrease with increasing elevation.

The phase error due to multipath from Equation 4.7a can, assuming that $A_r/A_d \ll 1$ and neglecting higher order terms in A_r/A_d, be approximated by

$$\delta\phi \approx \frac{A_r}{A_d}\sin(\psi) \tag{4.8}$$

where ψ is the previously mentioned multipath relative phase angle, i.e., the difference in phase between the direct and the reflected signal. From Equation 4.7b, the relative phase angle is causing the multipath oscillations of the SNR. Furthermore, assuming a planar reflector, the relative phase angle in radians (rad) can be derived geometrically from the path delay δ of the reflected signal as

$$\psi = \frac{2\,\pi}{\lambda}\,\delta = \frac{4\,\pi\,h_r}{\lambda}\,\sin(\theta) \tag{4.9}$$

where h_r is the distance between the antenna phase centre and the reflecting surface (reflector height), λ is the signal wavelength, and θ is the satellite elevation angle. The frequency of the multipath oscillations can be obtained by the rate of change of the relative phase angle from Equation 4.9, in rad, here assuming that both the elevation angle and the reflector height are time dependent, as

$$f_\psi = \frac{d\psi}{dt} = \frac{4\,\pi\,\dot{h}_r}{\lambda}\,\sin(\theta) + \frac{4\,\pi\,h_r}{\lambda}\,\cos(\theta)\,\dot{\theta} \tag{4.10}$$

where $\dot{\theta}$ and $\dot{h}_r$ are the rate of change of the elevation angle ($d\theta/dt$) and the reflector height (dh_r/dt), respectively. By performing a change of variable to $x = \sin(\theta)$, Equation 4.10 can be rewritten in rad (rad/$\sin(\theta)$) as

$$\frac{d\psi}{dx} = \frac{d\psi}{d\sin(\theta)} = \frac{d\psi}{dt}\,\frac{dt}{d\sin(\theta)} = \left(\frac{4\,\pi\,\dot{h}_r}{\lambda}\,\sin(\theta) + \frac{4\,\pi\,h}{\lambda}\,\cos(\theta)\,\dot{\theta}\right)\frac{1}{\cos(\theta)\,\dot{\theta}} = \frac{4\,\pi}{\lambda}\left(\dot{h}_r\frac{\tan(\theta)}{\dot{\theta}} + h_r\right) \tag{4.11}$$

Equation 4.11 shows that the frequency of the multipath oscillations, with respect to the sine of the satellite elevation angle, can be divided into two parts. First of all, assuming a constant reflector, i.e., the reflective surface is not moving, Equation 4.11 simplifies to $4\,\pi\,h_r/\lambda$. This means that as a function of sine of elevation angle, the frequency of the multipath oscillations is constant and could be derived from spectral analysis (see e.g., *Georgiadou & Kleusberg*, 1988; *Bilich et al.*, 2007, *Paper III and V)*. Second, with a time dependent reflector (moving reflector), Equation 4.11 becomes more complex. However, the left term on the right-hand side can be seen as a correction to the term for a constant reflector (right term). This was first described by *Larson et al.* (2013), see also *Nievinski* (2013) and *Paper IV*, after finding that the assumption of a constant reflector for a coastal GPS tide gauge experiencing high tidal variations (>7 m) was not sufficient and resulted in differences between reflector height solutions from rising and setting satellite arcs.

This correction term ($4\,\pi\,\dot{h}_r\,\tan(\theta)/(\lambda\,\dot{\theta})$; the left term on the right-hand side of Equation 4.11) contains the rate of change of the reflector height and has therefore been called a height-rate correction (*Larson et al.*, 2013). The difficulty is of course that in order to accurately determine the unknown parameter, i.e., the reflector height, there needs to be prior knowledge of the rate of change of the unknown parameter. The correction thus requires either a model of the rate of change of the reflector or additional observations of the reflector height, e.g., from the reflector height solution assuming a constant reflector (provided that the results are sufficient) or from another technique such as a nearby traditional tide gauge. The latter is of course not acceptable if the GNSS tide gauge should be used as an independent technique.

4.3.2 Data Analysis of SNR Observations

It has previously been shown that the reflected satellite signals interfere with the direct satellite signals, creating an interference pattern in the recorded SNR, and how the frequency of this interference pattern can be related to the height of the antenna above the reflecting surface. In this section, the same process will be described, but from a more practical point of view, illustrated with real GNSS observations from a GNSS tide gauge located on the coast and thus receiving reflected signals from the ocean.

The SNR value is a scaled version of the signal amplitude (assuming a constant noise level), that is derived from the carrier tracking loop of the GNSS receiver. The quantity is usually given as carrier-to-noise-density ratio (C/N_0), i.e., the signal power divided by the noise power spectral density in decibel-Hz (dB-Hz). Using the noise bandwidth (B), the SNR can be converted into units of decibels (dB, in logarithmic scale), watt per watt (in linear scale), or volt per volt (the square root of the SNR in linear scale) according to $SNR = (C/N_0)/B$, see *Joseph* (2010).

As an example of SNR observations affected by multipath, data from the same satellite recorded at different days in 2012, day-of-year (doy) 4 and doy 27, with a GNSS tide gauge, setup as in Figure 4.3, are presented in Figure 4.5 (top), for satellite elevation angles of 0° to 20°. The time period of each observation is about 40 min. As previously described (see Section 4.3.1), the multipath effect on the SNR, the envelope of the oscillations, is most dominant for lower satellite elevations and the amplitude of the envelopes decrease with increasing elevation angle. From Figure 4.5, it is apparent that the frequencies of the multipath oscillations are different for the two different SNR observations. The frequency of the SNR oscillations depends on the satellite-reflector-antenna geometry. In this case, the observations are from two different days, with the reflector (the sea surface) being at two different vertical positions.

In order to isolate the multipath contribution of the SNR observations, i.e., the SNR oscillations, the overall increasing arc of the SNR data for each satellite is usually removed. As previously mentioned, this arc is mostly dependent on the signal strength and the antenna gain pattern, see Equation 4.7b and Equation 4.8. Removing the arc is done either by fitting and removing a low-order polynomial, see e.g., *Larson et al.* (2009); *Paper III, IV, and V*, or by filtering, see *Benton & Mitchell* (2011). The remaining SNR signal from each arc, consisting of the multipath oscillations, is often called detrended SNR (δSNR) and can be described by

$$\delta SNR = A\cos(f_\psi + \varphi) \tag{4.12}$$

where A is the amplitude, f_ψ is the frequency of the SNR oscillations, which is a function of sine of the elevation angle (see also Equation 4.10), and φ is the phase offset. As an example of δSNR, the data from the same satellite recorded at different days in 2012, doy 4 and doy 27, with a GNSS tide gauge setup as in Figure 4.3, are presented in Figure 4.5, bottom. The δSNR is constructed by fitting and removing a second-order polynomial from the data in Figure 4.3 (top), clearly showing the SNR oscillations for each satellite observation.

For multipath from a reflector that can be assumed to be constant during the observation, i.e., not moving vertically, the frequency of the oscillations in the δSNR (or in SNR) is constant as a function of sine of satellite elevation angle, see Equation 4.11 for $\dot{h}_r = 0$. This is illustrated in Figure 4.5, bottom, showing oscillations with a constant frequency for each δSNR arc.

The dominant oscillation frequency can be obtained from the δSNR data by a spectral analysis of each arc, which can be done in a number of ways. The SNR data are evenly sampled in time, which is then also the case for the satellite elevation. However, δSNR (or SNR) as a function of sine of the satellite elevation angle is not evenly sampled. Therefore, spectral analysis of this unevenly sampled dataset can be difficult for, e.g., the Fast Fourier Transform. Instead, the Lomb-Scargle Periodogram (LSP) has been used, since it can handle unevenly spaced samples (see e.g., *Larson et al.*, 2009, 2013, *Paper III, IV, and V)*. The LSP, also called least-squares spectral analysis, estimates the spectral power (or the normalised periodogram) at each point instead of at each time of the signal based on a sinusoidal model, see *Lomb* (1976); *Scargle* (1982); *Press et al.* (1992).

For a computer implementation of the LSP, the spectral power is calculated for frequencies up to a maximum frequency ($hifac$) compared to the Nyquist frequency. This can be useful in the SNR-analysis, limiting unrealistic reflector heights (too high oscillation frequencies) by using a priori information from the GNSS site to set the parameter $hifac$ accordingly. In addition, a low $hifac$, will reduce the computational time. Another factor of importance is the oversampling factor ($ofac$), determining the resolution of the spectrum. For example, using an oversampling factor of 40 (which has been used in *Paper III, IV, and V*) corresponds to a reflector height precision of about 4 mm, i.e., the resolution in frequency of the LSP spectrum multiplied by the signal wavelength is 4 mm.

As an example of results from the LSP, Figure 4.6 depicts the spectral power for different frequencies obtained from LSP analysis of the δSNR arcs as a function of sine of elevation angle in Figure 4.5 (bottom). The two spectra show clear peaks (high power) at two different frequencies, which is consistent with the two different oscillation frequencies in Figure 4.5. Assuming a constant reflector (keep in mind Equation 4.11), the oscillations frequencies can easily be converted into reflector heights using the

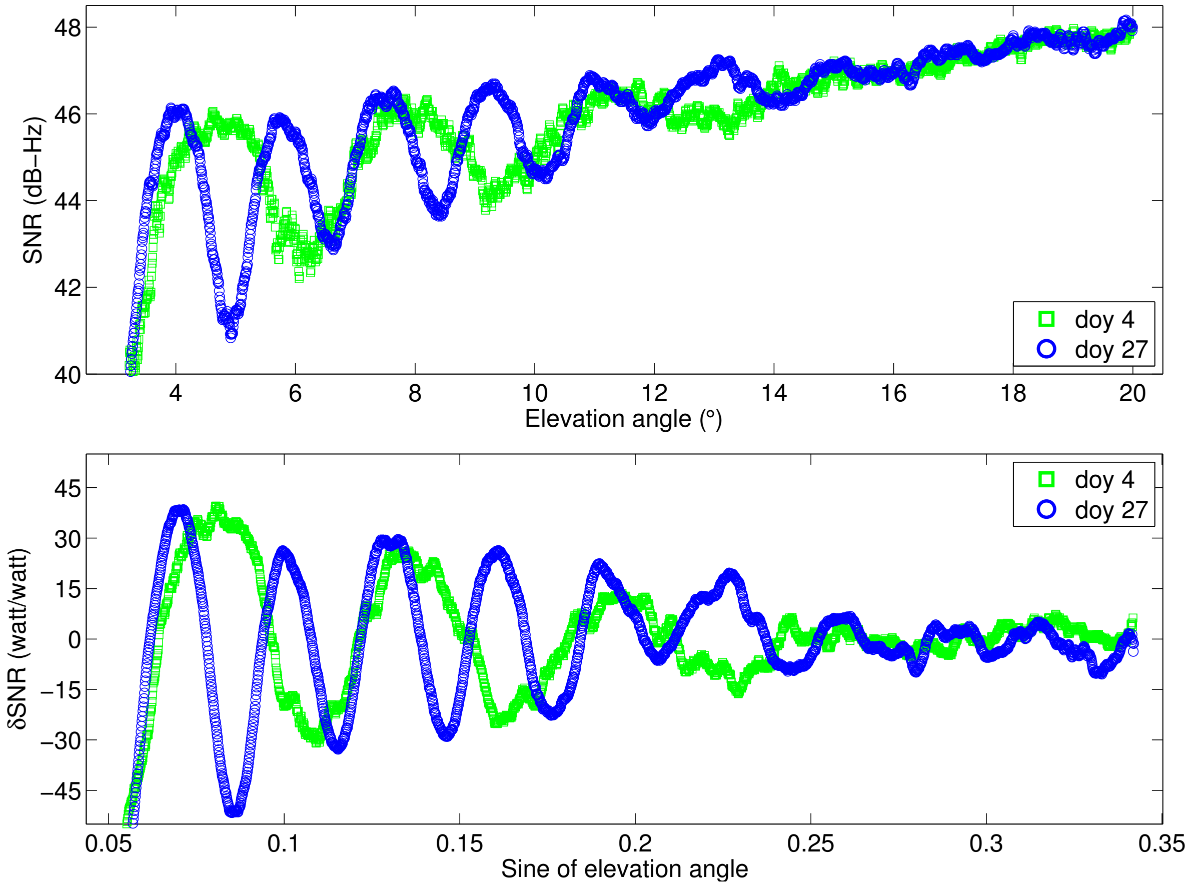

Figure 4.5: *Signal-to-Noise Ratio (SNR) data (top) and detrended SNR (δSNR; bottom) from a GPS satellite (frequency L_1) at two different days in 2012, day-of-year (doy) 4 and doy 27, observed during about 40 min each. The SNR data are recorded by a GNSS installation on the coast and are thus affected by multipath signals from that direction, interfering with the direct signals, and creating oscillations in the SNR data. The multipath effect is higher for low elevations than for high elevations and it is decreasing with increasing satellite elevation angle, see the decreasing amplitudes of the oscillation envelopes in the top figure. The δSNR is created by fitting and removing a low-order polynomial to the SNR arcs from the top figure, and is done in order to isolate the multipath oscillations. The reflector height (the sea surface) has changed between the two days, which can be seen from the different oscillation frequencies of the two SNR observations. For a reflector that is not changing with time during the observations, the SNR oscillation frequency is constant as a function of sine of elevation angle and can be directly related to the reflector height. The reflector height for the arc at doy 4 and doy 27 are 1.63 m and 3.07 m, respectively. SNR data are typically reported as carrier-to-noise-density ratio with the unit dB-Hz, but can be converted using the noise bandwidth to watt per watt in linear scale (see e.g., Joseph, 2010).*

signal wavelength. In Figure 4.6, the reflector height is presented on the top axis and the corresponding reflector heights for the dominant frequencies of the oscillations in the SNR arcs from doy 4 and doy 27 are 1.63 m and 3.07 m, respectively.

From Figure 4.6, it is evident that a high multipath frequency corresponds to a high reflector height and vice versa. For a GNSS station at the coast, affected by reflected signals from the ocean, the reflector height is directly proportional to the sea surface height. This means that a high multipath frequency, which is equivalent to a high reflector height (a large distance between the antenna and the sea surface), corresponds to a low sea level, whereas a low multipath frequency, which is equivalent to a

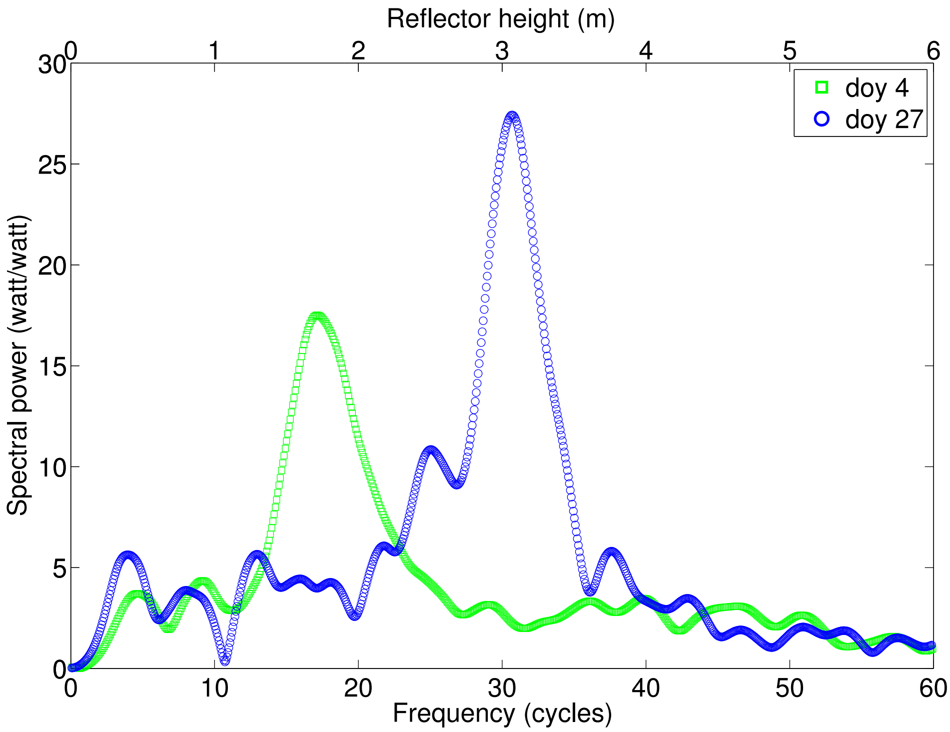

Figure 4.6: *Spectral power as a function of frequency from analysis of the two detrended Signal-to-Noise Ratio (δSNR) arcs, as a function of sine of elevation angle from Figure 4.5 (bottom), using the Lomb-Scargle Periodogram. The dominant frequency for the observation from day-of-year (doy) 4 is lower than the dominant frequency for the observation from doy 27. Assuming a constant reflector height during the observations the dominant frequency can be converted into reflector height, see the top axis. The corresponding reflector heights for the dominant frequencies are 1.63 m and 3.07 m for doy 4 and doy 27, respectively. Since the surface causing the reflections (and thus the oscillations in the SNR), is the sea surface, a larger value for the reflector height (a larger distance between the antenna and the reflector) is equivalent to a lower sea surface and vice versa.*

low reflector height (a short distance between the antenna and the sea surface), corresponds to a high sea level. Therefore, from Figure 4.6, the conclusion is that the sea level was higher during doy 4 than during doy 27.

When using the peak of the spectral power of the LSP spectrum to detect the multipath frequency (or the reflector height), the assumption made is that the δSNR data as a function of sine of the elevation angle only consists of one single frequency. From the peak of the two spectra in Figure 4.6, this is obviously not true. First of all, the sea surface is normally not perfectly flat, which will introduce an error in the detection. Second, the observed SNR data arcs are affected by multipath from several reflectors located in the surroundings of the installation. The error on the final reflector height (or sea level) solutions caused by other reflectors than the sea surface can be reduced by only selecting GNSS observations from directions where the sea surface is expected to be the only reflector. This can be done by making sure that the signal reflection area, i.e., the first Fresnel zone (see Section 3.1.2) is always located on the sea surface. If additional reflections are close in multipath frequency to the multipath frequency of the sea surface reflection, they will show up in the LSP spectrum and overlap the spectrum of interest. This could possibly distort the desired peak and introduce an error in the retrieved reflector height.

Besides selecting data from the directions of the desired reflector, there are some other restrictions that can be beneficial when retrieving the reflector height from the LSP. With knowledge of the GNSS site, it is possible to implement the physical restrictions for the site into the SNR-analysis, e.g., on-site measurements of minimum and maximum reflector heights. In the analysis, these values should be used with some additional window to account for possible extreme values of the reflector height. Another useful restriction is to somehow make sure that the peak of the highest spectral power is well above other peaks in the spectrum. A simple way to implement this is to only consider reflector heights which have a peak spectral power that is several times higher than the mean spectral power of the LSP.

Until now, only a non-moving reflector, i.e., the right term in Equation 4.11, has been considered. However, for a reflector that is moving substantially in the vertical direction during the observation, e.g, at a site with high tidal variations, the full result of Equation 4.11 needs to be considered when estimating the reflector height. As previously described, the left term in Equation 4.11 can be used as a correction term to the non-moving reflector solution (*Larson et al.*, 2013). The difficulty with this correction is that it contains the rate of change of the parameter of interest, i.e., the reflector height. It has therefore been called height-rate correction. One possibility would be to use another dataset, e.g., from a traditional tide gauge, to estimate the rate of change of the reflector height. However, this would to some extent defeat the purpose of having a GNSS tide gauge, since the sea level is already measured with the traditional tide gauge.

A first attempt to calculate the height-rates (the time derivative of the reflector heights) from the GNSS tide gauge data was made in *Paper IV*. This was done by using the reflector heights acquired from LSP during one day to directly estimate the height-rates from differentiation, i.e., taking the difference between two nearby reflector heights and divide by the time difference. However, this was not successful, since the height-rate values were too noisy. Instead, another method was developed, using the LSP-retrieved reflector heights for each day and least-squares fitting a sinusoidal function of the form

$$F(x) = x_1 + x_2 \sin(2\,\pi\, f_1\, t + x_3) \,+\, x_4 \sin(2\,\pi\, f_2\, t + x_5) \tag{4.13}$$

where x_i are the parameters to be determined and f_1 and f_2 are known frequencies. The idea was that the most significant contributions to the sea level (or reflector height) changes during one day come from the diurnal and the semi-diurnal tides. This assumption holds true, if the site does not experience a strong meteorological forcing relative to the tidal variations and is usually the case for sites with a high tidal range. There are several known diurnal and semi-diurnal tides. In order to reduce the number of parameters in the daily fit, only the mean frequencies of the dominant tides in each band was used, i.e., O_1: 25.8 h and K_1: 23.9 h (diurnal) and M_2: 12.4 h and S_2: 12.0 h (semi-diurnal). This resulted in diurnal and semi-diurnal frequencies with the period 24.9 h and 12.2 h, respectively. From the daily sinusoidal fit according to Equation 4.13, the height-rates values were calculated from the tangent of the function using 2 min of data around the time-tag of each LSP-retrieved reflector height. The height-rate values were then used together with the other parameters from the left term of Equation 4.11 to create height-rate corrections that were applied to each LSP-retrieved reflector height. For more information regarding the height-rate correction, see *Paper IV*.

5 GNSS Sea Level Results

The concept of the GNSS tide gauge, using bistatic radar measurements at L-band to estimate the sea level, was introduced in Chapter 4. The installation allows to record both the direct satellite signals and the satellite signals that are reflected off the sea surface. As previously mentioned, this thesis focuses on using standard geodetic commercially off-the-shelf GNSS equipment for recording these GNSS signals.

With a GNSS tide gauge installation using two antennae, it is possible to analyse both the phase-delay data and the Signal-to-Noise Ratio (SNR) data and obtain sea level. The phase-delay method utilises the difference in phase-delay between the direct and the reflected signal in standard geodetic analysis, whereas the SNR method utilises the interference of the direct and the reflected signal in SNR-analysis.

At the Onsala Space Observatory, three different GNSS tide gauge installations have been deployed in different campaigns since late 2008. All three installations contained two antennae connected to one receiver each recording both phase-delay and SNR, allowing sea level analysis using both the phase-delay method and the SNR method. The current installation was installed in the autumn of 2011 and is still continuously recording GNSS data for estimation of the varying sea level.

In this chapter, ***The GNSS Tide Gauges at the Onsala Space Observatory*** are described in detail together with results from some of the campaigns. In addition, the GNSS-derived sea level is compared and validated with sea level observations from several independent techniques, i.e., stilling well gauges in Ringhals and Gothenburg (about 18 km south and 33 km north of the observatory, respectively), pressure sensors co-located with the current GNSS tide gauge installation, and a bubbler tide gauge located at the observatory. These datasets are also described.

Additionally, a few ***GNSS Tide Gauges World Wide***, i.e., GNSS installations close to the ocean in different parts of the world, are presented. With data from these installations, consisting of a zenith-pointing GNSS antenna, it is possible to estimate the sea level using SNR-analysis. The resulting GNSS-derived sea level is compared to independent sea level observations from co-located traditional tide gauges.

5.1 The GNSS Tide Gauges at the Onsala Space Observatory

Since late 2008, there have been three different versions of the GNSS tide gauge at the observatory on the west coast of Sweden. The first setup was realised for a short campaign in December 2008, testing the phase-delay analysis, see *Paper I*. The second setup was installed in September 2010 and recording data until October 2011 for improving the phase-delay analysis and for introducing SNR-analysis for sea level, see *Paper II and III*, respectively. The current GNSS tide gauge installation was realised in October 2011 for continuous monitoring of the sea level at the observatory and it is still recording both

Figure 5.1: *The first (bottom left) and second (bottom right) experimental installation of the GNSS tide gauge at the Onsala Space Observatory both installed at the same location facing south (top). The top photo is taken from the north with the installation, left of the cabin, directed to the south (middle of photo) and with open sea water extending at least 100 m to the south. The two experimental installations consisted of two antennae with hemispherical radomes mounted back-to-back on a beam extending over the coastline. Both antennae were connected to one receiver each, recording GNSS data with a sampling frequency of up to 20 Hz. For the first installation (see bottom left), the antennae were not aligned horizontally, however, this was changed for the second installation (see bottom right).*

GNSS phase-delay and SNR data, see *Paper IV and V*.

All three installation have been realised according to Section 4.1, with one Right-Hand Circularly Polarised (RHCP) zenith-looking antenna and one Left-Hand Circularly Polarised (LHCP) nadir-looking antenna, each connected to a standard geodetic commercially off-the-shelf GNSS receiver. Since the visibility of satellites to the north is limited at these latitudes (57° N), the installations were directed towards the south, maximising the reflective surface and the number of observations. Below follows some more detailed information about the three different realisations of the GNSS tide gauge.

The first and second realisation of the GNSS tide gauge were both installed at the same location. This was on a wooden deck secured on the coastal bedrock on the southwest part of the observatory, close to a small cabin, providing electricity and shelter for the receivers, see Figure 5.1 (top). At this location, the water surface was extending at least 100 m towards the south, with an small island about 20 m to the east (see Figure 5.1, top and bottom right), and with the coastline approximately from azimuth 40° counterclockwise to 260°.

The first experimental installation of the GNSS tide gauge was deployed on December 1–3, 2008 (see

Figure 5.2: *The current installation of the GNSS tide gauge at the Onsala Space Observatory (bottom left and right) with a panoramic view of the reflective sea water surface towards the south (top). This location is situated a few hundred metres west of the location for the previous installations, see Figure 5.1, and has an open sea water surface of at least 100 m in a southward direction. The installation consists of two antennae with hemispherical radomes mounted back-to-back on a beam extending over the coastline (bottom left). With this installation it is possible to change the height of the antennae beam over the sea surface in steps of 25 cm (bottom right).*

Figure 5.1, bottom left). The bottom of the LHCP nadir-looking antenna was approximately 1 m over the sea surface during the campaign. Data were collected during three days using two Leica GRX1200 receivers, one connected to the zenith-looking RHCP antenna Leica AT504 GG choke-ring, and the other connected to the nadir-looking LHCP antenna Leica AR25 multi-GNSS choke-ring. Both antennae were covered by hemispherical radomes. In this first installation it was not possible to align the antennae along a local vertical (see Figure 5.1), but the horizontal baseline was measured and accounted for in the phase-delay analysis. Both receivers recorded 40 hours of continuous GNSS data with 20 Hz sampling rate. More information can be found in *Paper I*.

The second realisation of the GNSS tide gauge was mounted at the same location as the first installation in September 15, 2010, and was recording GNSS data with 20 Hz sampling rate (SNR resolution of 0.25 dB-Hz) until October 4, 2011 (see Figure 5.1, bottom right). The whole installation was setup slightly higher than the previous realisation to prevent the antennas from damage due to tides and waves during storm surges (local tidal range is about 20 cm, however, the local sea level can change by about ± 0.5 m due to meteorological forcing and storm surges). The bottom of the LHCP nadir-looking antenna was approximately 1.5 m over the sea surface. One major difference with this installation was that the antennae were aligned horizontally this time, see Figure 5.1 (bottom right). Additionally, another receiver (Leica GRX1200+) was connected to the RHCP zenith-looking antenna and the LHCP nadir-looking antenna was replaced with an LHCP antenna of the same type as the zenith-looking antenna (Leica AR25 multi-GNSS choke-ring). Both antennae were covered by hemispherical radomes. More information can be found in *Paper II and III*.

The current realisation of the GNSS tide gauge was installed at the observatory on October 13, 2011, and is still continuously recording GNSS data with 1 Hz sampling rate. Similar to the other two realisations, this installation was directed towards the south, but monumented at a location a few hundred metres west of the earlier location, see Figure 5.2 (top). The new installation was designed to be more robust and versatile than the previous versions, having the possibility of changing the height of the antennae beam. The lowest position of the antennae beam is approximately 2.5 m above the water surface (bottom of the LHCP nadir-looking antenna) and it can be raised in steps of 25 cm to about 4.75 m above the water surface, see Figure 5.2 (bottom right).

As can be seen in Figure 5.2 (top), the water surface is limited by bedrock to the east (left in the photo towards the 25 m telescope and the white radome of the 20 m telescope), and to the west (right in the photo), the water surface is limited by a beach and a few smaller islands. Nonetheless, the open water surface has a radius of more than 100 m and extends from about azimuth angles 60° to 300°.

The antennae are aligned horizontally, see Figure 5.1 (bottom left). Both the zenith-looking RHCP and the nadir-looking LHCP antennae are of the model Leica AR25 multi-GNSS choke-ring and both are covered by hemispherical radomes. Each antenna is connected to a Leica GRX1200GGPRO GNSS receiver recording both phase-delay and SNR data (resolution 0.25 dB-Hz). More information is given in *Paper IV and V*.

5.1.1 Traditional Tide Gauge Observations at the Onsala Space Observatory

Currently, there are several traditional tide gauges located either at the area of Onsala or on the west coast of Sweden. During the beginning of this study, the closest independent sea level observations were from two stilling well gauges, operated by the Swedish Meteorological and Hydrological Institute (SMHI), located at Ringhals and Gothenburg about 18 km south of and 33 km north of the observatory, respectively. The stilling well gauge consists of a vertical tube (well) of concrete, coated steel, or plastic (∼1 m diameter) extending below the lowest sea level to be measured. In the bottom of the well or in the lower parts of the well, small openings allow inflow and outflow of water. A float in the well is vertically connected, through a wire to a pulley (or a float wheel) and a counterweight system, to a recording system (*IOC*, 2006). The stilling well gauge is designed to filter out, or still, wave activity and works due to the ratio between the larger well and the smaller water openings as a low-pass filter. Because of this construction, the installation also experiences amplitude attenuation and a phase lag on shorter time periods (*IOC*, 2006). The accuracy of stilling well gauges is about 2 cm (*Pugh*, 1996).

The two stilling well gauge records from Ringhals and Gothenburg were used in *Paper I and II* for comparison with the GNSS-derived sea level. However, for *Paper III*, a single independent sea level time series, valid for the area of Onsala, was desired. Therefore, a synthetic tide gauge record based on the two tide gauge records from Ringhals and Gothenburg was constructed. The calculation of the synthetic tide gauge record was based on the distance from the observatory to the two tide gauges. For each stilling well gauge, a weighting factor was calculated as the distance between the other tide gauge and the observatory divided by the total distance between the stilling well gauges, which resulted in factors of 0.65 and 0.35 for Ringhals and Gothenburg stilling well gauge record, respectively. The final synthetic tide gauge record was then calculated by adding the two stilling well gauge records after multiplying them with their respective weighting factor. This weighting takes into account that a tide

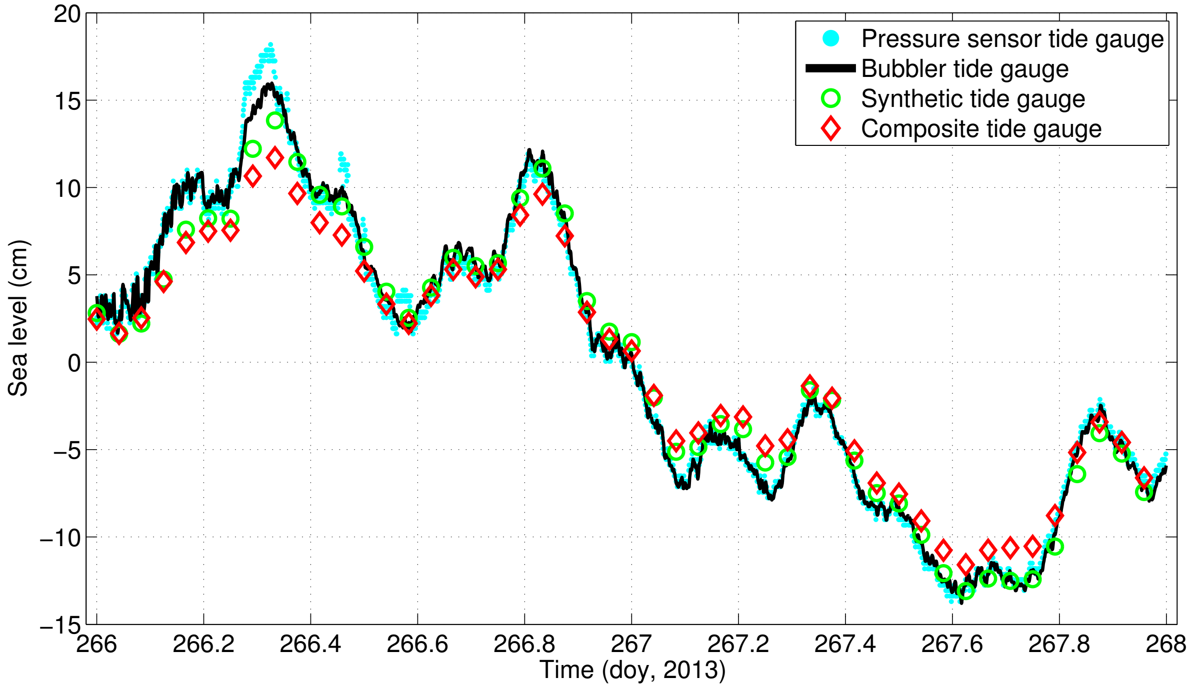

Figure 5.3: *Sea level records from the pressure sensor tide gauge (cyan dots) and the bubbler tide gauge (black line) located at the Onsala Space Observatory, together with sea level records from the synthetic tide gauge (green circles) and the composite tide gauge (red diamonds) constructed from the sea level records at Ringhals and Gothenburg. The observations are from September 23–24, day-of-year 266–267, 2013. A mean value is removed from each time series.*

gauge close to the observatory should have a larger weight than a tide gauge further away from the observatory. An example of the synthetic stilling well gauge record can be found in Figure 5.3.

A the beginning of 2012, three hydrostatic level transmitters (HLT) or pressure sensors were installed at the observatory for the possibility of co-located sea level measurements to the GNSS tide gauge installation. The pressure sensors were mounted together on a submerged pole and measure the pressure of the overlying column of water from the hydrostatic relation, see e.g., *IOC* (2006). The sensor type is a Mobrey series 9710 HLT with the temporal resolution set to 1 sample per second (usually the output averaged from 60 samples). The accuracy of the pressure sensors are related to the scale of the gauge as 0.1 % of the nominal range (0–5 m), which corresponds to an accuracy of 0.5 cm (*Emerson Process Management*, 2007).

After a comparison between the GNSS-derived sea level at the observatory and the synthetic tide gauge record, it was found that the weights (distance factors) for the records at Ringhals and Gothenburg were not fully representable for the sea level at the observatory. In order to improve the independent traditional sea level record at the observatory, for comparison with the GNSS-derived sea level, a composite sea level record was constructed. The new pressure sensors promised sea level observations with better accuracy than the stilling well gauges and a co-located record. However, they were not fully functional until the later half of 2012. Therefore, the pressure sensor sea level (the mean of the three pressure sensors) was fitted to the Ringhals and Gothenburg sea level record for the dates September 29, day-of-year (doy) 273, to December 31, doy 366, 2012. The model of the fit consisted of a rate for each stilling well gauge record and a common bias. Before the fit, the epochs of the pressure sensor sea level were interpolated to the epochs of the stilling well gauge record, since the former had a higher temporal resolution than the latter. The resulting coefficients of the model were calculated to 0.49 m, 0.47, and 0.39 for the bias, the rate for the Ringhals record, and the rate for the Gothenburg record, respectively.

These coefficients were then used to calculate the composite sea level record for the complete year of 2012, which was used for comparison to the GNSS-derived sea level in *Paper IV*. An example of the composite sea level record and the pressure tide gauge sea level record from one of the three sensors is presented in Figure 5.3.

In addition to the observations from the traditional tide gauges used in *Paper I to V*, a bubbler system (or bubbler tide gauge or pneumatic bubbler gauge) was installed during the autumn of 2013 for additional sea level observations at the observatory. The bubbler tide gauge is of the type CS471 Compact Bubbler System and has an accuracy of about ± 0.3 cm (*Campbell Scientific Inc.*, 2009). The bubbler is constructed to have compressed air, produced by a piston pump, flowing in a measuring tube into the water. The pressure created in the tube is then directly proportional to the water column above the bubble chamber and the height of the water level above the bubble chamber is calculated from the difference between the barometric air pressure and the bubble chamber pressure. An example of the bubbler tide gauge sea level record is presented in Figure 5.3.

For the time period of the data used in *Paper V*, the bubbler tide gauge was not installed yet at the observatory. Instead the pressure tide gauge was the available sea level record co-located with the GNSS tide gauge. In a comparison between the pressure tide gauge and the bubbler tide gauge using data from 2013, it was found that all three pressure sensors showed systematic errors (note that the bubbler tide gauge has a higher accuracy than the pressure sensors). For the comparison with the GNSS-derived sea level, the pressure sensor that showed only minor errors was used as the reference tide gauge in that study.

5.1.2 Sea Level Results

In *Paper I to V*, GNSS-derived sea level results from phase-delay analysis and SNR-analysis have been compared with traditional sea level observations, showing good agreement and high correlation. As an example of phase-delay analysis results, the Root-Mean-Square (RMS) differences between the GPS-derived sea level and the two stilling well gauge records were 5.5 cm to 5.9 cm for a 3 month period, with correlation coefficients of 0.95–0.96, and the RMS differences between the GNSS-derived sea level and the pressure sensor sea level were 3.2 cm to 3.5 cm for a period of about 1 month, with correlation coefficients of 0.95–0.96 (see *Paper II and V*, respectively). As an example of SNR-analysis results, the RMS difference between the GPS-derived sea level and the synthetic tide gauge records was 4.8 cm for a 3 month period, with a correlation coefficient of 0.97, and the RMS difference between the GNSS-derived sea level and the pressure sensor sea level was 4.0 cm to 4.7 cm (frequency band L_1) for a period of about 1 month, with correlation coefficients of 0.96–0.97 (frequency band L_1; see *Paper III and V*, respectively). Since these results are well described in *Paper I, II, and V* (see also a summary in Chapter 6), the following section is dedicated to some new results from the GNSS tide gauge at the observatory, namely GPS-derived sea level compared to the bubbler tide gauge sea level and preliminary phase-delay sea level results from two days of GPS double difference solutions.

For the comparison between GNSS-derived sea level and the traditional tide gauge records, both in *Paper I to V* and in this thesis, relative time series were used and they were not compared in an absolute sense, i.e., the benchmark of the GNSS tide gauge was not related to the benchmark of the traditional tide gauge. Instead, a mean was removed from each time series before the comparison. The reasons for this were that neither antenna phase centre variations were taken into account in the analysis, nor signal phase changes from the reflection, e.g., carrier phase wind-up (see *Beyerle*, 2009).

As an example of sea level results from the GNSS tide gauge, both phase-delay analysis (single differences) and SNR-analysis were performed on GPS L_1 data from September 23 (doy 266) to September 29 (doy 272), 2013. The resulting GPS-derived sea level time series are shown in Figure 5.4 together with sea level from the co-located bubbler tide gauge. The GPS-derived time series were treated in a similar way as the GNSS-derived time series in *Paper V*, i.e., all phase-delay solutions that had a formal error in the least-squares minimisation process of larger than 4 cm were removed and for both the phase-delay and the SNR solutions a moving average filter with a window size of approximately 3 h was applied to each time series. From the difference between the original time series and the filtered

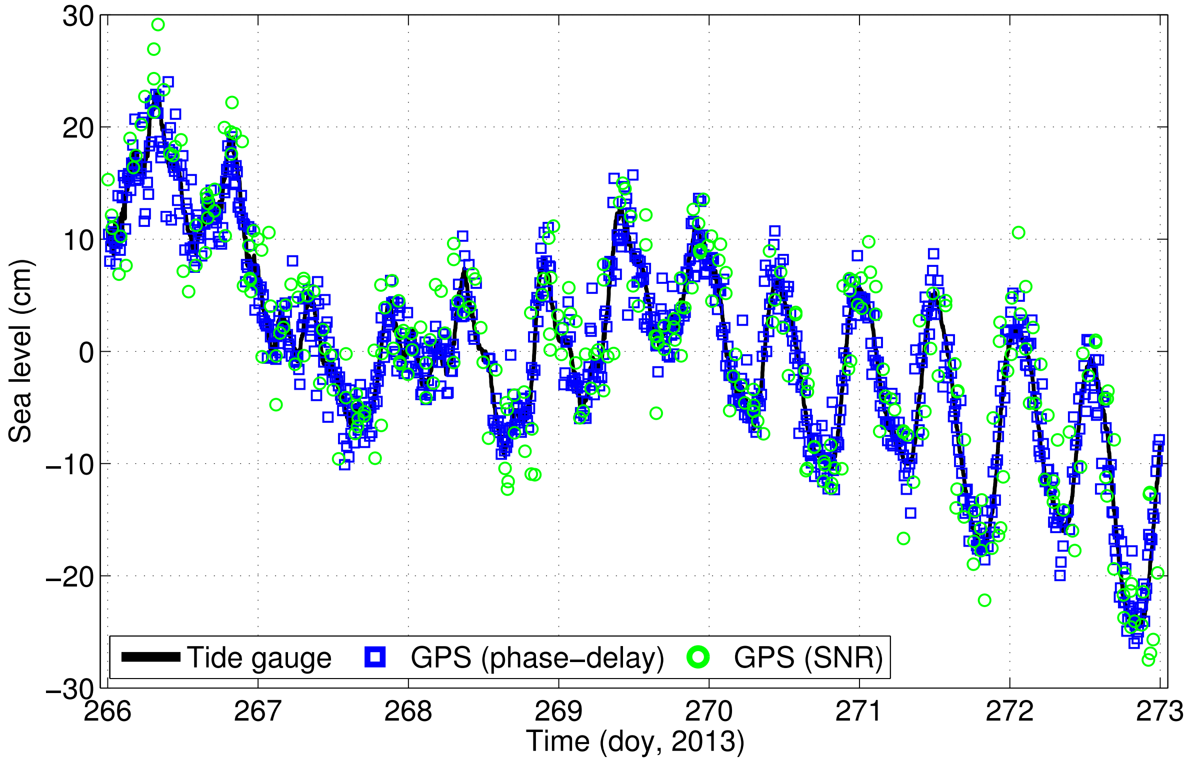

Figure 5.4: *Sea level from phase-delay analysis (blue squares) and Signal-to-Noise Ratio (SNR) analysis (green circles) of GPS L_1 data recorded by the GNSS tide gauge at the Onsala Space Observatory and sea level observations from the co-located bubbler tide gauge (black line). Observations are from September 23, day-of-year (doy) 266, to September 29, doy 272, 2013. A mean value is removed from each time series. The Root-Mean-Square differences between the bubbler gauge record and the sea level derived from phase-delay analysis and SNR-analysis are 2.1 cm and 4.0 cm, respectively.*

time series, observations outside of 3σ were considered as outliers and removed.

In Figure 5.4, a good agreement between the GPS-derived sea level and the co-located bubbler gauge record is visible. To quantify the results, the RMS differences with respect to the bubbler tide gauge record are 2.1 cm and 4.0 cm for the phase-delay analysis and the SNR-analysis, respectively. The corresponding correlation coefficients are 0.98 and 0.92, respectively. The results are consistent with *Paper V*, where in addition to GPS results also sea level results from GLONASS observations are presented.

The phase-delay sea level solutions that have been shown in this thesis, and in *Paper I, II, and V*, are all based on single difference analysis, see Section 4.2. However, another type of phase-delay analysis was mentioned, namely double difference analysis. The analysis is similar to the single difference analysis, but the recorded data are combined in another way. Double differences are created by taking the difference between observations from two receivers and two satellites, instead of taking the difference between observations from two receivers (which is the single difference combination). The advantage of using double differenced observations instead of single differenced observations for GPS data is the possibility of fixing the ambiguity parameters to integer values, which will improve the accuracy of the solutions (for more information see Section 4.2).

Phase-delay analysis using both single differences, previously called phase-delay analysis, and double differences with integer ambiguities using the LAMBDA method (see Section 4.2) were performed on GPS L_1 data from the GNSS tide gauge at the observatory for July 20–21 (doy 201–202), 2011. The preliminary sea level results from the phase-delay analysis are shown in Figure 5.5, together with the

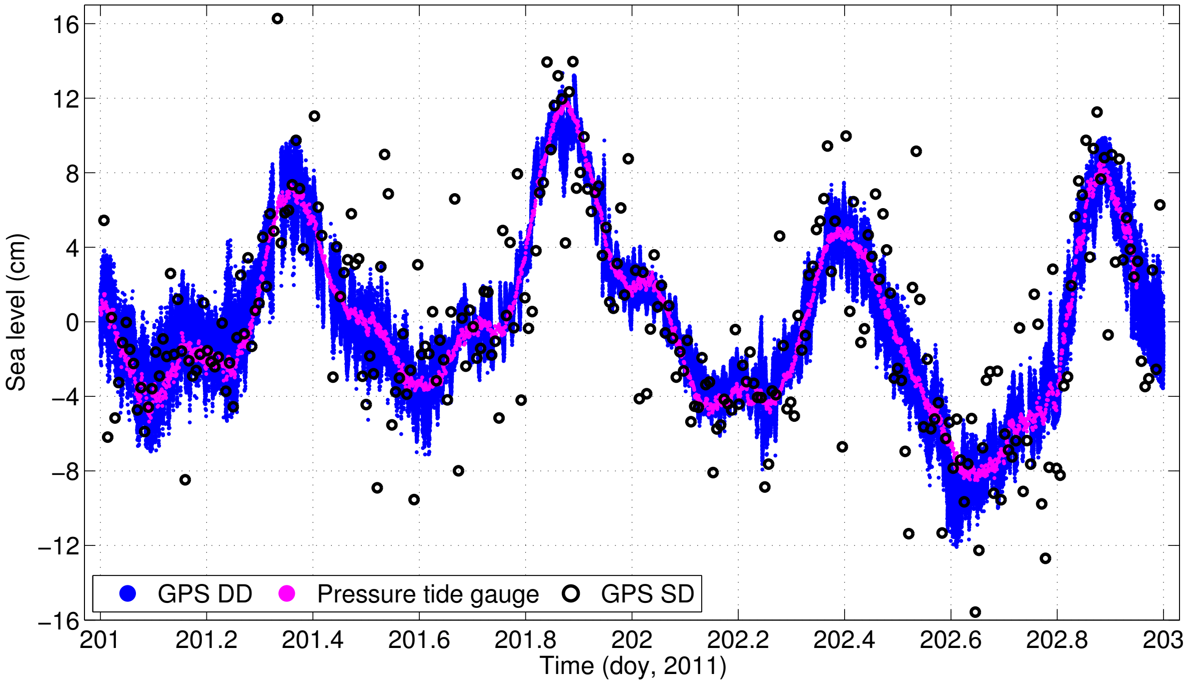

Figure 5.5: *Sea level from phase-delay analysis of GPS L_1 data from the GNSS tide gauge at the Onsala Space Observatory. Sea level solutions are from both single differenced observations (GPS SD; black circles) and double differenced observations with integer ambiguities (GPS DD; blue dots) together with the mean of the sea level records of the co-located pressure gauge sensors (magenta dots). A mean value is removed from each time series. The temporal resolution of the single difference solution is lower than that of the double difference solution (every 10 min compared to every second), however, it can also be as high as the sampling rate of the GPS data, which is 1 sample per second. The root-mean-square differences with respect to the pressure sensor sea level record are 3.4 cm and 0.6 cm for the single difference and the double difference sea level, respectively.*

mean of the sea level from the three co-located pressure gauge sensors.

In Figure 5.5, it appears that the double difference phase-delay sea level has a better agreement with the pressure gauge sea level than the single difference phase-delay sea level. It should be noted that the temporal resolution of the double difference time series is 1 solution per second, which is the sampling rate of the of the GPS data, whereas the temporal resolution of the single difference time series is one solution every 10 min. However, the temporal resolution of the single difference analysis results can also be as high as the sampling rate of the GPS data, see e.g., *Löfgren et al.* (2010), but for *Paper I, II, and V*, the temporal resolution is every 10 min and therefore the same is shown for the single difference solution in this thesis.

In order to compare the single difference and the double difference sea level to each other and to the pressure sensor sea level record without introducing a bias from the different number of solutions to compare (the temporal resolution of the pressure sensor record is 1 sample per min), the comparison was done at the epochs of the single difference sea level. In addition, since the single difference solutions consisted of data from 20 min around that epoch, the double difference solutions were averaged around 20 min for the chosen epochs. The correlation coefficients as compared to the pressure sensor sea level record were 0.79 and 0.99 for the single difference and the double difference sea level solutions, respectively. The RMS differences show similar results, i.e., that the double difference solution (with integer ambiguity parameters) performs better than the single difference solution (with float ambiguity parameters), with RMS differences of 3.4 cm and 0.6 cm for the single difference and the double differ-

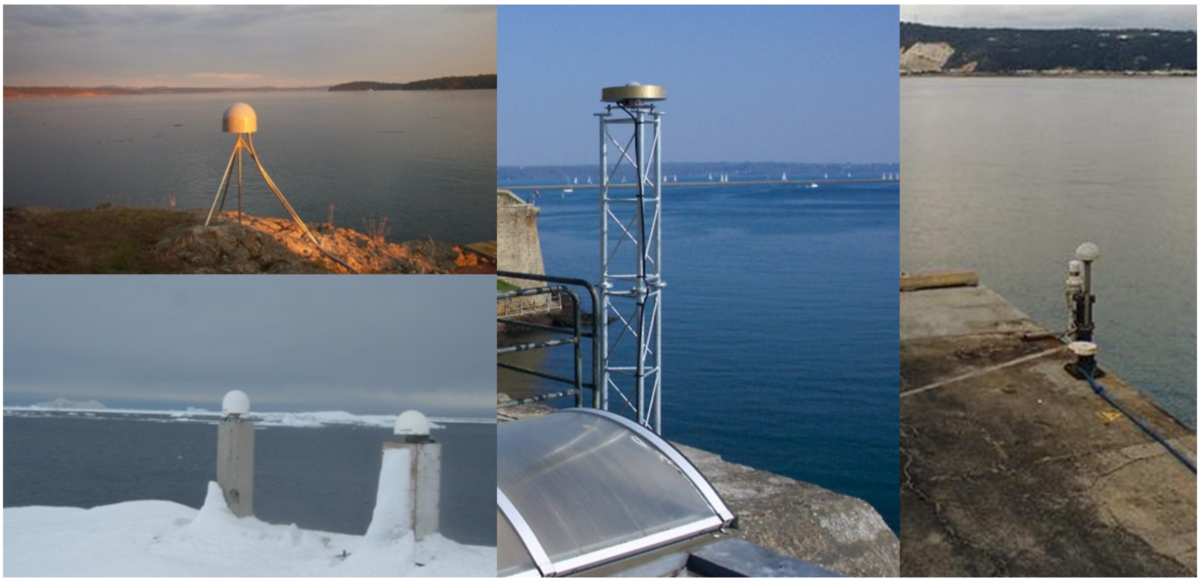

Figure 5.6: *Permanent GNSS reference stations that are also GNSS tide gauges: SC02 (top left) in Friday Harbor, USA; OHI3 (bottom left) in O'Higgins, Antarctica; BRST (middle) in Brest, France; and BUR2 (right) in Burnie, Australia. More information about the stations, together with sea level results can be found in Paper III, and IV. The original photographs for SC02, OHI3, BRST, and BUR2 were provided by the University NAVSTAR Consortium (UNAVCO), Ruslan Artemenko (Deutsches Zentrum für Luft- und Raumfahrt, DLR), the Institut National de l'Information Geographique et Forestiere (IGN), and Christopher Watson (University of Tasmania), respectively.*

ence sea level solution, respectively.

5.2 GNSS Tide Gauges World Wide

The possibility to use any GNSS station as a GNSS tide gauge, provided that it is installed close enough to the ocean, was introduced in Chapter 4. With a location close to the ocean, the multipath signals reflected in the ocean surface will interact with the direct signals, affect the observables, and through analysis of the recorded SNR data, the sea level can be derived. In *Paper III, IV, and V*, this analysis was made with data from the GNSS tide gauge at the Onsala Space Observatory and results from the analysis were illustrated previously in this chapter. In this section, the focus lies on GNSS stations in permanent GNSS reference networks, see Section 2.5. These stations were not installed to measure the sea level, however, for some of the vast number of GNSS stations, it is possible.

In *Paper III and IV*, 4 different permanent GNSS reference stations are introduced as GNSS tide gauges. These stations are SC02 (Friday Harbor, USA), BRST (Brest, France), BUR2 (Burnie, Australia), and OHI3 (O'Higgins, Antarctica), which are operated by the University NAVSTAR Consortium (UNAVCO), the Institut National de l'Information Geographique et Forestiere (IGN), Geoscience Australia (GA), and Bundesamt für Kartographie und Geodäsie (BKG), respectively. Photographs of these sites can be found in Figure 5.6, showing the antennae mountings in the vicinity of the ocean, and additional information about the sites can be found in *Paper IV*.

The reason for using these quite different sites as GNSS tide gauges is of course that they are all affected by multipath from the ocean surface. However, equally important is that the effect of this multipath is recorded in the observables with a high enough quality for SNR-analysis. *Paper IV and V* provide some discussion and suggested criteria or guidelines on how to select a suitable GNSS station for use as a GNSS tide gauge. Below, some of these criteria are highlighted with a short explanation.

First of all, the GNSS station has to be located on the coast, close enough to the ocean to receive multipath signals reflected off the ocean surface. The closer to the water, the better. However, since the multipath effect on the recorded SNR is most dominant for observations from satellites with low elevation angles (0° to 30°, see Section 4.3), the GNSS station does not have to be directly next to the water to be affected. As long as the antenna has an unobstructed view for small negative elevation angles (0° to about –30°, corresponding to low satellite elevation angles), it will be affected by multipath from the ocean. This is of course also a function of antenna height over the ocean surface, e.g., an antenna installed on a higher pillar (with a large vertical distance between the antenna and the ocean surface) can be placed further inland than an antenna on a lower pillar (with a short distance between the antenna and the ocean surface) and still be affected by ocean multipath. Examples are BUR2, which has a short vertical installation and is located right next to the water, and SC02 and OHI3, which both have a larger vertical distance to the sea surface and can therefore be used even though they are installed further inland (see Figure 5.6).

By recalling the reflective surface, approximated by the first Fresnel zone (see Section 3.1.2), a criterion can be set for the possible horizontal distance between the antenna and the ocean surface. For example, an antenna with a vertical distance to the ocean surface of 4.3 m can be located about 9 m inland and still record multipath from the ocean for observations from satellites with elevation angles of less than 15°, see Figure 3.2. In this case, the reflective surface is still over the ocean surface. In practice, this is also a function of the land terrain and the shape of the coastline. Making sure that the reflective surface is always on the ocean surface for the desired observations will also ensure clear multipath oscillations, i.e., observations affected dominantly by multipath from the ocean surface and not from other reflecting objects such as islands or the surface next to the antenna.

Second, the sampling rate of the GNSS receiver is of great importance and the sufficient sampling rate can be seen as a function of the antenna height over the ocean surface. For example, an antenna high over the ocean surface, e.g., BRST (see Figure 5.6), results in SNR oscillations with a higher frequency than for an antenna closer to the ocean surface, e.g., BUR2 (see Figure 5.6). Thus, in the first case, the SNR oscillation period is sampled with less data points than in the second case, assuming that data are recorded with receivers using the same sampling rate. In practice, this means that a receiver connected to an antenna that is located vertically close to the ocean surface can have a low sampling rate, whereas a receiver connected to an antenna that is located vertically high over the ocean surface needs a higher sampling rate, in order to resolve the recorded SNR oscillations. For the analysed data described in this thesis, the sampling rate was 1 sample per second (1 Hz), which is common for current geodetic-type GNSS receivers. This sampling rate has been sufficient even for the station BRST, which has the mean vertical distance between the antenna and the sea surface of approximately 17 m. The sampling rate of 1 Hz is not necessary for the analysis of data from most GNSS stations. However, the conventional sampling rate of 1 sample per 30 seconds (0.033 Hz) often appears to be too low. It is therefore unfortunate that networks often only store the 30 s data because of data storage limitations.

Third, the resolution of the SNR observations needs to be considered. It has been reported by *Bilich et al.* (2007) that there is a considerable inconsistency among GNSS receiver manufacturers and models. From previous studies, e.g., *Anderson* (2000); *Paper III, IV, and V*, the SNR resolution needs to be on the order of 1 dB, or actually 1 dB-Hz, in order to resolve the SNR oscillations sufficiently.

Fourth, the vertical distance between the antenna and the sea surface will have an impact on the temporal resolution and the accuracy of the measurements. For example, an antenna installed high above the sea surface will result in SNR data with a high oscillation frequency. This means that it will take a shorter time to record a given number of oscillation periods than for an antenna closer to the sea surface. Thus, it could be possible to divide the SNR arcs and estimate the sea level more often. In addition, estimating the sea level from shorter SNR arcs, provided that enough periods of the multipath oscillations are observed during that time, results in a GNSS-derived sea level that probably agrees better with the actual sea level, since the sea level will not change significantly during short epochs. An installation with a short vertical distance to the sea surface would therefore be a very unfortunate setup for measuring sea level at a location with a large tidal variation.

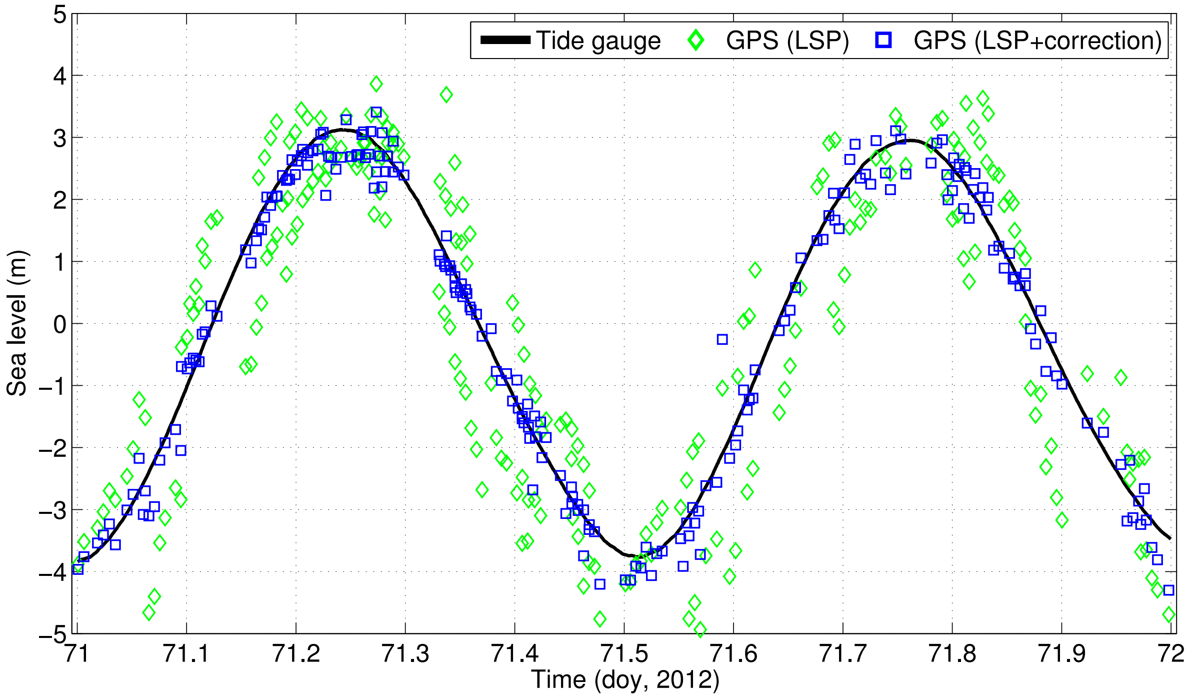

Figure 5.7: *Sea level during March 11, day-of-year (doy) 71, 2012 at the harbour of Brest, France. The GPS-derived sea level is from SNR-analysis using only Lomb Scargle Periodogram (LSP, see Section 4.3.2), GPS (LSP) green diamonds, and using LSP and the height-rate correction (see Section 4.3.1), GPS (LSP+correction) blue squares, whereas the traditional tide gauge record comes from a radar sensor, see Paper IV. A mean value is removed from each time series. For a site with a high tidal variation such as Brest, using the height-rate correction in the SNR-analysis improves the sea level results significantly. For example, using 1 year of data and comparing the GPS-derived sea level with the sea level record from the traditional tide gauge, the correlation coefficient increased from 0.89 to 0.97 and the root-mean-square difference decreased from 81.5 cm to 43.2 cm, applying the correction term.*

5.2.1 Sea Level Results

GNSS-derived sea level from SNR-analysis has been compared to traditional tide gauge records of sea level in *Paper III, IV, and V* as well as in Section 5.1.2. The comparisons showed high correlation and a good agreement between the GNSS-derived sea level and the sea level records from the traditional tide gauges. As an example of the results, the correlation coefficient and the RMS difference between the GPS-derived sea level from SC02 and the traditional tide gauge record at Friday Harbor were 0.98 and ∼10 cm, respectively, for analysis of data from a period of about 3.5 months (see *Paper III*). In this study, at a site with a tidal range of about 407 cm, the height-rate correction was not applied in the SNR-analysis, see Section 4.3.1. Additional examples, applying the height-rate correction in the SNR-analysis, can be found in *Paper IV*. Using the station BUR2 as an example, the correlation coefficient increased from 0.95 to 0.96 and the RMS difference decreased from 26.5 to 25.1 from the dataset of about 1 year. Conversely, it was shown that for sites with a small tidal range, the height-rate correction, or at least the height-rate correction that was applied using a diurnal and semi-diurnal fit, did not improve the results. Examples are the GNSS tide gauge at the observatory with a tidal range of about 165 cm, where the correction did not improve the results, and the GNSS station OHI3 with a tidal range of about 272 cm, where the correction only slightly improved the RMS difference with the traditional tide gauge (see *Paper IV*).

Since results from the SNR-analysis of data from the GNSS tide gauge at the observatory, a site experiencing very small tidal variations, was presented in Section 5.1.2, SNR-analysis results from BRST, a site experiencing high tidal variations (about 772 cm), are presented in this section as a complimentary example. In Figure 5.7, GPS-derived sea level from SNR-analysis of 1 day of data from the GNSS station BRST in the harbour of Brest, France, is presented. Results with and without the height-rate correction (see Section 4.3.1) are shown, illustrating the improvement possible for sites experiencing high tidal variations using this correction term. From Figure 5.7, it is clearly visible that the SNR-analysis using the correction term better resembles the traditional tide gauge sea level than the SNR-analysis solution without the correction term. In comparison of the GPS-derived sea level time series with the traditional tide gauge record for 1 year, the correlation coefficient increased from 0.89 to 0.97 and the RMS difference decreased from 81.5 cm to 43.2 cm, when applying the correction term.

6 Conclusions and Future Work

The focus of this thesis was to use standard geodetic-type commercially off-the-shelf Global Navigation Satellite System (GNSS) equipment to record signals reflected off the sea surface and estimate the local sea level. This was achieved using the different GNSS tide gauge installations at the Onsala Space Observatory, allowing to record the GNSS signals reflected off the sea surface in different ways. First of all, the phase-delay of the reflected GNSS signals were recorded directly with the receiver connected to the nadir-looking antenna. Together with the phase-delay of the direct signals, recorded with the receiver connected to the zenith-looking antenna, standard geodetic analysis provided GNSS sea level observations. Second, the Signal-to-Noise Ratio (SNR) recorded with the receiver connected to the zenith-looking antenna, provided an indirect measurement of the reflected GNSS signals, as the reflected signals interfered with the direct GNSS signals and affected the recorded observables. From analysis of the multipath oscillations, an additional type of sea level observation was possible. Furthermore, the SNR-analysis method allowed other GNSS stations, located close to the ocean, in different parts of the world to become GNSS tide gauges.

Comparisons of the GNSS-derived sea level with independent observations from traditional tide gauges showed a high level of agreement with correlation coefficients of 0.89–0.99. The sea level results from the phase-delay analysis performed better with respect to the traditional sea level records than the SNR-analysis. As an example, the Root-Mean-Square (RMS) differences between the GNSS-derived sea level (using frequency band L_1), observed during 1 month with the GNSS tide gauge at the observatory, and the sea level observations from the co-located tide gauge were 3.5/3.2 cm (GPS/GLONASS) and 4.0/4.7 cm (GPS/GLONASS) for the phase-delay analysis and the SNR-analysis, respectively. Results from analysis of observations from both systems (GPS and GLONASS) showed similar performance, whereas results based on data from frequency band L_2 (recorded with receivers using the P(Y)-code) were more noisy than those based on data from frequency band L_1. However, results based on observations from GPS L_{2C} transmitting satellites seemed to be at least as good as those from L_1.

The temporal resolution of the GNSS-derived sea level is different for the two analysis methods. For the phase-delay analysis, the temporal resolution can be as high as the sampling rate of the GNSS data, whereas for the SNR-analysis, the temporal resolution depends on the number of rising and setting satellites observed over the ocean. This also means that the sea level derived from the SNR-analysis is not evenly sampled during the day, which is the case for the sea level derived from the phase-delay analysis.

Sea level results from 5 different GNSS stations around the world illustrate the valuable concept that any GNSS station close to the ocean can be used as a GNSS tide gauge. In comparison with co-located traditional tide gauges, the RMS differences were on the order of 6.2 cm for stations with a low tidal range (up to 165 cm) and 43 cm for stations with a high tidal range (up to 772 cm). In this case, an extended SNR-analysis approach was applied, modelling a time dependent sea level during each satellite arc. For stations with high tidal range, the sea level results based on the extended SNR-analysis approach agreed better with the tide gauge records, than the results based from the standard SNR-analysis approach (assuming a static sea level during each satellite arc). Furthermore, the results indicated that for stations with a tidal range of up to about 270 cm, the standard analysis approach can be used without performing significantly worse than the extended analysis approach.

As previously mentioned, the GNSS phase-delay observations allow a higher accuracy in the estimated sea level than the SNR observations, but they have proven to be more vulnerable to rough sea surface conditions due to the receiver tracking loop. With the wind speed as an indicator for sea surface roughness, the performance of the two analysis methods were evaluated. The results were that the SNR-analysis was possible even during the highest wind speed observed (17.5 m/s), while the phase-delay analysis became difficult for wind speeds above 6 m/s.

The results from this thesis show that it is possible to use standard geodetic commercially off-the-shelf GNSS receivers for recording signals reflected from the sea surface and together with phase-delay analysis and SNR-analysis accurately estimate the local sea level.

Further conclusions are presented as a ***Summary of Paper I, II, III, IV, and V*** and the section ***Future Work*** consists of an outlook of the GNSS tide gauge research.

6.1 Summary of Paper I

The first experimental installation of the GNSS tide gauge was constructed at the observatory in the end of 2008, recording 40 h of continuous 20 Hz sampled GPS data. This installation demonstrated the concept of the phase-delay method, during calm sea conditions, using standard geodetic-type GNSS receivers to record reflected signals from the sea surface. Additionally, estimates of the local sea level were produced from the post-processing data analysis.

The analysis of the SNR of the recorded signals showed, as expected, that the reflected signals were more noisy than the direct signals and both signals experienced multipath effects and lower SNR for lower elevation angles that at higher elevation angles. After exclusion of observations with azimuth angles from the north-west, corresponding to the bedrock where the installation was mounted, the majority of these erroneous observations were removed, concluding these effects to mostly originate from the bedrock and surroundings. Moreover, the remaining observations showed that the reflected signals had a lower SNR than the direct signals with an average difference in SNR during 12 h of 1.0–3.4 dB.

Using an early version of the in-house developed single difference analysis software in MATLAB, 1 Hz GPS phase-delay data (the recorded 20 Hz data were re-sampled) were processed leading to 27 estimates of local sea level. The result of comparison with independent datasets of sea level from two stilling well gauges, in Ringhals and Gothenburg, showed good RMS agreement of 3.7 cm (3.3 cm between the both stilling well gauges).

6.2 Summary of Paper II

Starting in September 2010 the GNSS tide gauge was operated continuously with a sampling frequency of 1 Hz, recording three months of data until the middle of December. These observations demonstrated the phase-delay concept and the possibility of meaningful and valuable sea level estimation over longer time periods. The effect of reflection of GPS signals from the sea surface was examined theoretically as well as the impact of the reflective surface, which depends on the satellite elevation angle and the antenna height of the installation over the water.

From the further developed in-house single difference analysis software, the three months of GPS phase-delay data were analysed to estimate the local sea level. The time series showed several data gaps related to limitations of the downward-looking receiver in rough sea surface conditions (the coherent part of the reflected signal decreases), but some of these gaps could also partly be due to the data analysis algorithm.

The GPS-derived time series of sea level showed good agreement with the Ringhals and Gothenburg stilling well gauge time series with an RMS agreement of 5.9 cm and 5.5 cm, compared to 6.1 cm from the comparison between the stilling well gauges. Additionally, the correlation between the time series were high with correlation coefficients higher than 0.95. Moreover, slope coefficients were estimated in the comparison to 0.90 and 0.99 involving the GNSS-derived sea level and 1.03 between the stilling well gauges.

Further validation and comparison of the GNSS-derived time series were done in the frequency domain showing a high level of agreement with coherency up to a frequency of six cycles per day between the datasets. Using an ocean tide analysis, harmonic solutions of a full year (2010) of data from the stilling well gauge sea level time series were compared with the three months of GNSS solutions. Even though the GNSS-derived time series were noisier than the stilling well gauge time series (which are constructed to low-pass filter the sea level observations), several tidal components were determined above the 1-σ limit: M_2, S_2, N_2, O_1, M_4. The ocean tide results for the observatory are in between those of the two stilling well gauges north and south of the observatory. Furthermore, comparison with model calculations based on global ocean tide models with local refinement revealed limitations in the ocean tide models.

6.3 Summary of Paper III

From the SNR data recorded by the GNSS tide gauge at the observatory during a three month period from the middle of September to December (the same time period as in *Paper II*), local sea level was estimated for the first time using SNR-analysis. This method had previously only been applied to measurements of soil moisture and snow depth.

The SNR data were evaluated to find directions with multipath reflections from the ocean. Since the affected observations originated from lower satellite elevation angles than for the phase-delay analysis, the reflective surface of the observations were larger and further away from the installation. With the fairly low installation, the antenna used was approximately 1.5 m over the sea surface, the SNR arcs obtained for the SNR-analysis were about 45–65 min long. During the SNR-analysis of the 1 Hz sampled GPS data, one static sea level was estimated for each arc. It was noted that clear peaks could be found in the Lomb Scargle Periodogram spectrum for the retrieval of reflector height, but these were weaker than observed in similar studies devoted to snow depth.

The GPS-derived sea level was compared to sea level from a synthetic tide gauge based on the sea level records from the two stilling well gauges in Ringhals and Gothenburg, weighted with the distances to the observatory. The synthetic tide gauge record was constructed to obtain a single co-located tide gauge record valid for the location of the observatory. The comparison showed that the RMS difference between the GPS-derived sea level and the synthetic tide gauge record was 4.8 cm, with a correlation coefficient of 0.97.

In addition to the GNSS tide gauge at the observatory, a GPS station at Friday Harbor (USA), SC02, operated by the EarthScope Plate Boundary Observatory (PBO) was used for sea level estimation for the time period of about 3.5 months. One of the main differences between the site at Onsala and the site in Friday Harbor was that the tidal variations are much larger for the Friday Harbor site. The SC02 GPS SNR data had a sampling rate of 1 sample per 15 s (0.67 Hz) and the data used were only from L_{2C} transmitting satellites (see Section 2.2). Each analysed SNR arc was about 25 min long. The RMS difference between the GPS-derived sea level and the sea level record from the co-located tide gauge was $\sim$10 cm, with a correlation coefficient of 0.98.

Furthermore, the two GPS-derived sea level time series for the observatory were compared, i.e., the sea level derived from phase-delay analysis in *Paper II* was compared to the sea level derived from SNR-analysis in this paper. The sea level from the phase-delay analysis had a lower RMS value in comparison with the synthetic tide gauge (4.0 cm versus 4.8 cm) and a higher temporal resolution than the sea level from SNR-analysis. However, the sea level from SNR-analysis performed better during windy conditions.

6.4 Summary of Paper IV

The SNR-analysis method was evaluated for 5 different GPS stations located in different regions around the world, with different multipath environment (from rural coastal areas to busy harbors), and experiencing different tidal ranges. The stations were GTGU (Onsala, Sweden; the zenith-looking antenna of the new GNSS tide gauge installation at the observatory), SC02 (Friday Harbor, USA), BRST (Brest, France), BUR2 (Burnie, Australia), and OHI3 (O'Higgins, Antarctica).

The recorded SNR from the 5 sites were analysed by spectral analysis using two approaches: a standard analysis approach assuming a static sea level during a satellite arc, similar to *Paper III*, and an extended analysis approach involving a time dependent sea level during a satellite arc (also described as a height-rate correction, see Section 4.3.1). The SNR-analysis was performed on 1 year of GPS L_1 data from each station (6 months for GTGU).

The GPS-derived sea level time series for each site were compared to a sea level record from co-located tide gauge, showed a high correlation with correlation coefficients on the order of 0.89–0.99. The RMS differences were on the order of 6.2 cm for stations with low tidal range (up to 165 cm) and 43 cm for stations with high tidal range (up to 772 cm), in the latter case using the extended analysis approach. The relative accuracy, defined as the ratio of RMS difference and tidal range, was between 2.4 % and 10.2 % for all stations.

For stations with high tidal range, the sea level results based on the extended SNR-analysis approach agreed better with the tide gauge records, than the results from the standard approach, e.g., for the station with the highest tidal range (772 cm) the RMS difference was reduced by 47 % when using the extended approach. Furthermore, the results indicated that for stations with a tidal range of up to about 270 cm, the standard analysis approach (assuming a static sea level) can be used without performing significantly worse than the extended analysis approach.

The GPS-derived sea level results were also compared to the tide gauge records in the frequency domain. Tidal amplitudes and phases were derived by harmonic analyses of the GNSS and the traditional sea level records. A high level of agreement is observed and again the results based on the extended analysis approach perform better for stations with large tidal ranges.

6.5 Summary of Paper V

The GNSS tide gauge at the observatory was used to evaluate both the phase-delay analysis method, using the one antenna approach, and the SNR-analysis method, using the two antennae approach, with dual-frequency observations from both GPS and GLONASS. By using observations from several GNSS, the installation was for the first time truly a GNSS tide gauge. Signals from the frequency bands L_1 and L_2 were used during the 1 month long campaign. In contrast to *Paper III*, the L_2 observations were not from L_{2C} transmitting satellites (see Section 2.2), since these signals had already been evaluated. Instead the L_2 signals were from receivers using the P(Y)-code.

The results from both analysis methods were compared to independent sea level observations from a co-located pressure tide gauge, showing high correlation for both systems and frequency bands with correlation coefficients of 0.86–0.97. The results from the phase-delay analysis showed at better agreement with the tide gauge sea level than the results from the SNR-analysis with RMS differences of 3.5 cm (GPS L_1 and L_2) and 3.3/3.2 cm (GLONASS L_1/L_2 bands) compared to 4.0/9.0 cm (GPS L_1/L_2) and 4.7/8.9 cm (GLONASS L_1/L_2 bands).

The two satellite systems, GPS and GLONASS, showed similar performance in the comparison for both phase-delay analysis and SNR-analysis. The results revealed that for the phase-delay analysis it is possible to use both frequencies and achieve similar results, whereas for the SNR-analysis, L_2 observations from receivers using the P(Y)-code should be avoided.

Additionally, the phase-delay analysis method and the SNR-analysis method were investigated for their sensitivity for sea surface roughness. This was done using wind speed as an indicator for sea surface roughness. It was found that the SNR-analysis performs better in rough sea surface conditions than the phase-delay analysis. The SNR-analysis was possible even during the highest wind speed observed during the campaign (17.5 m/s), while the phase-delay analysis became difficult for wind speeds above 6 m/s, confirming the results from *Paper II*.

6.6 Future Work

In the future, the sea level results will benefit from multi-GNSS solutions, i.e., combining several GNSS observations for the analysis. For example, using GPS, GLONASS, Galileo, and BeiDou signals together will significantly increase the number of observations in a combined phase-delay analysis, providing more precise sea level estimates. Furthermore, the combination of multi-GNSS observations will also be an advantage for the SNR-analysis, increasing the temporal resolution of the sea level results. In addition, an improved handling of antenna phase centre variations and signal reflection effects will allow time series of absolute sea level for both analysis methods.

The current GNSS tide gauge installation at the observatory allow to change the height of the antennae in 25 cm steps in the approximate range of 1.5–4.5 m over the sea surface. This will aid in the evaluation of absolute sea level from the phase-delay analysis and the SNR-analysis method. In addition, the newly installed bubbler tide gauge at the observatory, promising an even better accuracy than the previously used traditional tide gauges, will allow further assessment of the quality of the GNSS tide gauge at the observatory. The previously described qualifications of the new GNSS tide gauge installation at the Onsala Space Observatory, makes it the perfect GNSS-R installation for systematic studies and calibration of GNSS-R instruments. It would therefore be of interest to operate other GNSS-R instruments side-by-side with the current GNSS tide gauge.

For the phase-delay analysis, the plan is to implement a filter-based analysis software as a first step in developing real-time sea level monitoring. This software will include an improved handling of phase ambiguity parameters, cycle slips, and outlier editing. In addition, with the promising results from the double difference phase-delay analysis using integer ambiguity parameters, further development of this approach is of interest. With these contributions, it would also be interesting to test the software on other kinematic datasets.

Another future possibility for the GNSS tide gauge at the observatory would be to use multi-GNSS, multi-frequency, phase-delay analysis and SNR-analysis in a filter approach, in order to benefit from the individual advantages. From this multi-combination, it should be possible to derive continuous and accurate absolute GNSS sea level time series in a wide range of sea surface roughnesses.

There are thousands of geodetic GNSS stations in GNSS networks around the world, operated by different organisations that provide free-of-charge data for research purposes. A subset of these stations are located next to the ocean and thus record multipath signals from the ocean, which can be used to determine the sea level. These GNSS tide gauges can be used either on their own, or if traditional tide gauges exists, as a compliment. It is therefore of great interest to identify suitable stations and to make sure that the stored data are of the right quality and have the right sampling rate.

Bibliography

Anderson, K. D., (1995), A GPS tide gauge, presented at *GPS World Showcase*, 6, pp. 44-44.

Anderson, K. D., (1996), Remote sensing: a valuable source of information, paper presented at the *AGARD SPP Symposium*, Toulouse, France, 22–25 April.

Anderson, K. D., (2000), Determination of Water Level and Tides Using Interferometric Observations of GPS Signals, *J. Atmos. Oceanic Technol.*, 17, 8, pp. 1118–1127.

Auber, J.-C., A. Bibaut, & J.-M. Rigal, (1994), Characterization of Multipath on Land and Sea at GPS Frequencies. *Proceedings of 7th International Technical Meeting of the Satellite Division of the Institute of Navigation*, Part 2, ION GPS-94, Sept. 1994, pp. 11551171.

AVISO (Archiving, Validation and Interpretation of Satellite Oceanographic data), (2011), *Mean Sea Level rise*, Centre National d'Etudes Spatiales (CNES), Laboratoire d'Etudes en Géodésie et Océanographie Spatiales (LEGOS), and Collecte Localisation Satellites (CLS), available from: `http://www.aviso.oceanobs.com/en/news/ocean-indicators/mean-sea-level/index.html`, (December 30, 2013)

Bai, W., Y. Sun, Y. Fu, G. Zhu, Q. Du, Y. Zhang, Y. Han, & C. Cheng, (2011), GNSS-R open-loop difference phase altimetry: Results from a bridge experiment, *J. Adv. Space Res.*, 50, 8, pp. 1150-1157.

Bedford, L., N. Brown, & J. Walford, (2009), Leica AR25 White paper, Leica Geosystems AG, Heerbrugg, Switzerland, available from `http://www.leica-geosystems.com/common/shared/downloads/inc/downloader.asp?id=10904`, (December 11, 2013).

Benedicto, J., G. Giuliano, A. Garutti, J. Paffet, A. Bradford, C. Jackson, & E. Rooney, (2006), The Triumph of GIOVE-A, European Space Agency, *Bulletin 127*, available from: `http://www.esa.int/esapub/bulletin/bulletin127/bul127i_benedicto.pdf`, (December 2, 2013).

Benton, C. J., & C. N. Mitchell, (2011), Isolating the multipath component in GNSS signal-to-noise data and locating reflecting objects, *Radio Sci*, 46, RS6002.

Beyerle, G., (2009), Carrier phase wind-up in GPS reflectometry, *GPS Solut.*, 13, pp. 191–198.

Bilich, A. L., P. Axelrad, & K. M. Larson, (2007), Scientific Utility of the Signal-to-Noise Ratio (SNR) Reported by Geodetic GPS Receivers, in *Proceedings of the 20th International Technical Meeting of the Satellite Division of the Institute of Navigation ION GNSS 2007*, Fort Worth, Texas, pp. 19992010.

Bilich, A., K. M. Larson, & P. Axelrad, (2008), Modeling GPS phase multipath with SNR: Case study from the Salar de Uyuni, Boliva, *J. Geophys. Res.*, 113, B04401.

Bindoff, N. L., J. Willebrand, V. Artale, A. Cazenave, J. Gregory, S. Gulev, K. Hanawa, C. Le Qur, S. Levitus, Y. Nojiri, C. K. Shum, L. D. Talley, & A. Unnikrishnan, (2007), Observations: Oceanic Climate Change and Sea Level, In: *Climate Change 2007: The Physical Science Basis*, Contribution of Working Group I to the Fourth Assessment Report of the Intergovernmental Panel on Climate Change [Solomon, S., D. Qin, M. Manning, Z. Chen, M. Marquis, K. B. Averyt, M. Tignor, & H. L. Miller (eds.)], Cambridge University Press, Cambridge, United Kingdom and New York, NY, USA, pp. 385–432.

Bishop, G. J., J. A. Klobuchar, & P. H. Doherty, (1985), Multipath effects on the determination of absolute ionospheric time delay from GPS signals, *Radio Sci.*, 20, 3, pp. 388–396.

Blewitt, G., (1997), Basics of the GPS Technique: Observation Equations, In: *Geodetic Applications of GPS*, [Johnson B. (ed.)], Nordic Geodetic Commission, Sweden, ISSN 0280–5731, pp. 10–54.

Campbell Scientific Inc., (2009), *Instruction Manual CS470/CS471 Compact Bubbler System*, Revision: 7/11, Campbell Scientific Inc., USA, available from: `http://www.campbellsci.com/cs470-specifications`, (January 2, 2014).

Caparrini, M., A. Egido, F. Soulat, O. Germain, E. Farres, S. Dunne, & G. Ruffini, (2007), Oceanpal®: Monitoring Sea State with a GNSS-R Coastal Instrument, *Proceedings of the 2007 IEEE International Geoscience and Remote Sensing Symposium*, July 23–28 2007, Barcelona, Spain, pp. 5080–5083.

Cardellach, E., F. Fabra, O. Nogués, S. Oliveras, S. Ribó, A. Rius, & M. Belmonte, (2009), From Greenland to Antarctica: CSIC/IEEC results on sea-ice, dry-snow, soil-moisture, and ocean GNSS reflections, *Proceedings of the 2nd International Colloquium - Scientific and Fundamental Aspects of the Galileo Programme*, European Space Agency, October 14–16 2009, Padua, Italy, 7 pp., proceedings CD ROM.

Cardellach, E., A. Rius, A., M. Martín-Neira, F. Fabra, O. Nogués-Correig, S. Ribó, J. Kainulainen, A. Camps, & S. Addio, (2013), Consolidating the Precision of Interferometric GNSS-R Ocean Altimetry using Airborne Experimental Data, *IEEE Transactions on Geoscience and Remote Sensing*, in print.

Chambers, D., J. C. Ries, C. K. Shum, & B. D. Tapley, (1998), On the use of tide gauges to determine altimeter drift, *J. Geophys. Res.*, 103 (C6), pp. 12885-12890.

Cheng, K., C. Shum, S. Han, Y. Yi, & D. Martin, (2002), Application of GPS-Buoy Water Level Instrument for Radar Altimeter Calibration, *in Gravity, Geoid, and Geodynamics 2000: GGG2000 IAG International Symposium*, International Association of Geodesy Symposia, Sym. 123. Edited by M.G. Sideris. Springer, pp. 171-178.

Chong, C., (2009), Status of COMPASS/BeiDou Development, *Stanfords 2009 PNT Challenges and Opportunities Symposium*, October 21–22 2009, presentation, San Francisco, United States.

Church, J. A., N. J. White, L. F. Konikow, C. M. Domingues, J. G. Cogley, E. Rignot, J. M. Gregory, M. R. van den Broeke, A. J. Monaghan, & I. Velicogna, (2011), Revisiting the Earths sealevel and energy budgets from 1961 to 2008, *Geophys. Res. Lett.*, 38, L18601.

Dach, R., U. Hugentobler, P. Fridez, & M. Meindl, (2007), *Bernese GPS Software Version 5.0, User manual*, Astronomical Institute, Universtiy of Bern, 640 pp.

Davis, J., T. Herring, I. I. Shapiro, A. Rogers, & G. Elgered, (1985), Geodesy by radio interferometry: Effects of atmospheric modeling errors on estimates of baseline length, *Radio Sci.*, 20, pp. 1593–1607.

Dow, J. M., R. E. Neilan, & C. Rizos, (2009), The International GNSS Service in a changing landscape of Global Navigation Satellite Systems, *J. Geod.*, 83, pp. 191–198.

Dunne, S., F. Soulat, M. Caparrini, O. Germain, E. Farres, X. Barroso, & G. Ruffini, (2005), Oceanpal®, a GPS-reflection coastal instrument to monitor tide and sea-state, Paper presented at *Oceans 2005 – Europe*, 2, Brest, France, 20–23 June 2005.

Elósegui, P., J. L. Davis, R. T. K. Jaldehag, J. M. Johansson, A. E. Niell, & I. I.Shapiro, (1995), Geodesy using the Global Positioning System: The effects of signal scattering on estimates of site position, *J. Geophys. Res.*, vol. 100, B6, pp. 2156–2202.

Emerson Process Management, (2007), *Mobrey Series 9700 Hydrostatic level transmitter - Instruction Leaflet*, IP342, Rev. AB, 12 pp., United Kingdom, available from: http://www2.emersonprocess.com/en-US/brands/mobrey/Level-Products/Hydrostatic/9700-Series/Pages/index.aspx, (January 2, 2014).

Engberg, L. E., A. Engfeldt, L. Jivall, C. Kempe, M. Lidberg, C. Lilje, M. Lilje, D. Norin, H. Steffen, P. Wiklund, & J. Ågren, (2013), National Report of Sweden to the EUREF 2013 Symposium – geodetic activities at Lantmäteriet, *EUREF 2013 Symposium*, May 29–31, 2013, presentation, Budapest, Hungary, available from: http://euref2013.fomi.hu/Download/Session_6/Sweden_NationalReport2013_paper.pdf, (December 2, 2013).

ESA (European Space Agency), (2013a), Galileo In-Orbit Validation Fact Sheet, *European Space Agency*, available from: http://download.esa.int/docs/Galileo_IOV_Launch/Galileo_factsheet_2012.pdf, (December 2, 2013).

ESA (European Space Agency), (2013b), Galileo Full Operational Capability Fact Sheet, *European Space Agency*, available from: http://download.esa.int/docs/Galileo_IOV_Launch/FOC_factsheet_20111003.pdf, (December 2, 2013).

European Union, (2010), European GNSS (Galileo) Open Service Signal-In-Space Interface Control Issue 1.1 (OS SIS ICD), *E*uropean Union, available from: http://ec.europa.eu/enterprise/policies/satnav/galileo/files/galileo-os-sis-icd-issue1-revision1_en.pdf, (December 2, 2013).

Gakstatter, E., (2006), Survey: L2C – not just vanilla GPS anymore, *GPS World*, April issue, United States, available from http://gpsworld.com/surveyl2c-not-just-vanilla-gps-anymore-3399/, (November 28, 2013).

Gao, G. X., D. M. Akos, T. Walter, & P. Enge, (2008), GIOVE-B on the Air - Understanding Galileo's New Signals, *Inside GNSS*, May/June Issue, Gibbons Media & Research LLC, United States, available from: http://www.insidegnss.com/auto/mayjune08-Gao.pdf, (December 2, 2013).

Garrison, J. L., S. J. Katzberg, & M. I. Hill, (1998), Effect of sea roughness on bistatically scattered range coded signals from the Global Positioning System, *Geophys. Res. Lett.*, 25, pp. 2257-2260.

Georgiadou, Y., & A. Kleusberg, (1988), On carrier signal multipath effects in relative GPS positioning, *Manusc. Geod.*, 13, pp. 172–179.

Gfg^2 Consortium, (2013), GNSS for Global Environmental Earth Observations, *Gfg^2 Best Practices Booklet*, Chalmers Reproservice, Gothenburg, 32 pp, available from: http://www.gfg2.eu/sites/gfg2.eu/files/Gfg2\%20booklet_web.pdf, (November 13, 2013).

Gleason, S., S. Hodgart, Y. Sun, C. Gommenginger, S. Mackin, M. Adjrad, & M. Unwin, (2005), Detection and Processing of bistatically reflected GPS signals from low Earth orbit for the purpose of ocean remote sensing, *Trans. Geosci. Remote Sensing*, 43, 6, pp. 1229–1241.

GPS World, (2011), GLONASS Modernization, *GPS World*, November issue, United States, available from http://gpsworld.com/glonass-modernization-12232/, (November 28, 2013).

GPS World, (2012a), Directions 2013: Plans Set in Motion for GPS, *GPS World*, December issue, United States, available from http://gpsworld.com/directions-2013-plans-set-in-motion-for-gps/, (November 14, 2013).

GPS World, (2012b), Directions 2013: GLONASS Today and Tomorrow, *GPS World*, December issue, United States, available from http://gpsworld.com/directions-2013-glonass-today-and-tomorrow/, (November 14, 2013).

Gurtner, W., & L. Estey, (2013), RINEX – The Receiver Independent Exchange Format Version 3.02, *International GNSS Service (IGS), RINEX Working Group and Radio Technical Commission for Maritime Services Special Committee 104 (RTCM-SC104)*, available from http://igscb.jpl.nasa.gov/igscb/data/format/rinex302.pdf, (December 16, 2013).

Hammarklint, T., (2010), *Havspeglar*, Swedish Meteorological and Hydrological Institute (SMHI), available from: http://www.smhi.se/kunskapsbanken/oceanografi/havspeglar-1.13444, (December 31, 2013).

Hannah, B. M., (2001), Modelling and simulation of GPS multipath propagation, *Ph.D. thesis*, Queensland University of Technology.

Hein, G. W., H. Landau, & H. Blomenhofer, (1990), Determination of instantaneous sea surface, wave heights, and ocean currents using satellite observations of the global positioning system, *Marine Geodesy*, 14, 3, pp. 217–224.

Hernández-Pajares, M., J. M. Juan, J. Sanz, & R. Orús, (2007), Second-order ionospheric term in GPS: Implementation and impact on geodetic estimates, *J. Geophys. Res.*, 112, B08417, 16 pp.

Herring, T. A., R. W. King, & S. C. McClusky, (2010), *Introduction to GAMIT/GLOBK Release 10.4*, Department of Earth, Atmospheric, and Planetary Sciences, Massachusetts Institute of Technology, 48 pp.

Hobiger, T., R. Haas, & J. S. Löfgren, (2013), GLONASS-R: GNSS reflectometry with an FDMA based satellite navigation system, *Radio Sci.*, submitted December 2013.

Hofmann-Wellenhof, B., H. Lichtenegger, & J. Collins, (2001), *GPS Theory and Practice - Fifth, revised edition*, Springer, New York, 382 pp.

Häkli, P., M. Poutanen, J. Näränen, A. Raja-Halli, H. Koivula, J. Kuokkanen, S. Marila, & M. Ollikainen, (2013), National Report of Finland, *EUREF 2013 Symposium*, May 29–31, 2013, presentation, Budapest, Hungary, available from: http://euref2013.fomi.hu/Download/Session_6/Finland_NationalReport2013.pdf, (December 2, 2013).

ILRS (International Laser Ranging Service), (2012), COMPASS, *International Laser Ranging Service*, available from: http://ilrs.gsfc.nasa.gov/missions/satellite_missions/current_missions/cmm3_general.html, (December 2, 2013).

Inside GNSS, (2006), The L2C Study: Benefits of the New GPS Civil Signal, *Inside GNSS*, July/August issue, Gibbons Media & Research LLC, United States, available from http://www.insidegnss.com/node/888, (November 28, 2013).

Inside GNSS, (2013), First Galileo FOC Satellite Doresa Passes Thermal Vacuum Tests, *Inside GNSS News*, November 27, Gibbons Media & Research LLC, United States, available from http://www.insidegnss.com/node/3794, (December 2, 2013).

Inside GNSS, (2013), BeiDou – Chinas Rapidly Emerging GNSS, *Inside GNSS*, May/June issue, Gibbons Media & Research LLC, United States, available from http://www.insidegnss.com/node/3590, (December 2, 2013).

IOC (Intergovernmental Oceanographic Commission of UNESCO), (2006), *Manual on Sea-level Measurements and Interpretation, Volume IV: An update to 2006*, IOC Manuals and Guides No.14, vol. IV, JCOMM Technical Report No.31; WMO/TD. No.1339, 78 pp, Paris.

IPCC, (2007), Summary for Policymakers, In: *Climate Change 2007: The Physical Science Basis*, Contribution of Working Group I to the Fourth Assessment Report of the Intergovernmental Panel on Climate Change [Solomon, S., D. Qin, M. Manning, Z. Chen, M. Marquis, K. B. Averyt, M. Tignor, & H. L. Miller (eds.)], Cambridge University Press, Cambridge, United Kingdom and New York, NY, USA, 18 pp.

ITU (International Telecommunication Union), (1992), Electrical Characteristics of the Surface of the Earth, *Recommendation ITU-R P.527-3*, ITU Radiocommunication Assembly.

Jacobson, M. D., (2010), Snow-covered lake ice in GPS multipath reception - Theory and measurement, *J. Adv. Space Res.*, 46, pp. 221–227.

Johansson, J. M., J. L. Davis, H.-G. Scherneck, G. A. Milne, M. Vermeer, J. X. Mitrovica, R. A. Bennett, B. Jonsson, G. Elgered, P. Elosegui, H. Koivula, M. Poutanen, B. O. Rönnäng, & I. I. Shapiro, (2002), Continuous GPS measurements of postglacial adjustment in Fennoscandia 1. Geodetic results, *J. Geophys. Res. (Solid Earth)*, 107 (B8), pp. ETG3.1–ETG3.27.

Joseph, A., (2010), What is the difference between SNR and C/N0?, *InsideGNSS*, 5(8), pp. 20-25.

Kato, T., Y. Terada, K. Ito, R. Hattori, T. Abe, T. Miyake, S. Koshimura, & T. Nagai, (2005), Tsunami due to the 2004 September 5th off the Kii peninsula earthquake, Japan, recorded by a new GPS buoy, *Earth, Planets, Space*, 57, pp. 297–301.

Katzberg, S., & J. Garrison, (1996), Utilizing GPS to determine ionospheric delay over the ocean, *NASA Tech. Memo 4750*, 14 pp.

Katzberg, S., (1998), Applications of GPS altimetry for Wetlands mapping, paper presented at *GPS Applications to the Structure and Dynamics of the Earths Oceans and Ionosphere Workshop*, Arcadia, Calif., Dec. 1-3.

Keller, K., M. Weber, & K. Engsager, (2013), National Report Denmark, *EUREF 2013 Symposium*, May 29–31, 2013, presentation, Budapest, Hungary, available from: `http://euref2013.fomi.hu/Download/Session_6/Denmark_NationalReport2013.pdf`, (December 2, 2013).

Komjathy, A., V. Zavorotny, P. Axelrad, G. Born, & J. Garrison, (1998), GPS signal scattering from sea surface: Comparison between experimental data and theoretical model, paper presented at *Fifth International Conference on Remote Sensing for Marine and Coastal Environments*, Environ. Res. Ins. of Mich. International, San Diego, Calif., Oct. 5–7.

Komjathy, A., J. Maslanik, V. Zavorotny, P. Axelrad, & S. Katzberg, (2000), Sea Ice Remote Sensing Using Surface Reflected GPS signals, paper presented at *IEEE International Geoscience and Remote Sensing Symposium*, Honolulu, HI, July 24–28.

Kuo, C.-Y., K.-W. Chiu, K.-W. Chiang, K.-C. Cheng, L.-C. Lin, H.-Z. Tseng, F.-Y. Chu, W.-H. Lan, & H.-T. Lin, (2012), High-Frequency Sea Level Variations Observed by GPS Buoys Using Precise Point Positioning Technique, *Terr. Atmos. Ocean. Sci.*, 23, 2, pp. 209-218.

Larson, K. M., E. E. Small, E. D. Gutmann, A. L. Bilich, J. J. Braun, & V. U. Zavorotny, (2008), Use of GPS receivers as a soil moisture network for water cycle studies, *Geophys. Res. Lett.*, 35, L24405.

Larson, K. M., E. D. Gutmann, V. U. Zavorotny, J. J. Braun, M. W. Williams, & F. G. Nievinski, (2009), Can we measure snow depth with GPS receivers?, *Geophys. Res. Lett.*, 36, L17502, 5 pp.

Larson, K. M., J. J. Braun, E. E. Small, V. U. Zavorotny, E. D. Gutmann, & A. L. Bilich, (2010), GPS Multipath and Its Relation to Near-Surface Soil Moisture Content, *IEEE Journal of Selected Topics in Applied Earth Observations and Remote Sensing*, 3, 1, pp. 91–99.

Larson, K. M., R. D. Ray, F. G. Nievinski, J. T. Freymueller, (2013), The Accidental Tide Gauge: A GPS Reflection Case Study From Kachemak Bay, Alaska, *IEEE Geosci. Remote Sens. Lett.*, 10, 5,pp. 1200–1204.

Lidberg, M., J. M. Johansson, H.-G. Scherneck, & G. A. Milne, (2010), Recent results based on continuous GPS observations of the GIA process in Fennoscandia from BIFROST, *J. Geodyn.*, 50(1), pp. 8–18.

Lomb, N. R., (1976), *Astrophysics and Space Science*, 2, pp. 447–462.

Lowe, S. T., C. Zuffada, Y. Chao, P. Kroger, & L. E. Young, (2002a), 5-cm-Precision aircraft ocean altimetry using GPS reflections, *Geophys. Res. Lett.*, 29, 10, 1375.

Lowe, S. T., J. L. LaBrecque, C. Zuffada, L. J. Romans, L. E. Young, & G. A. Hajj, (2002b), First spaceborne observation of an Earth-reflected GPS signal, *Radio Science*, 37, 1, 28 pp.

Löfgren, J. S., R. Haas, & J. M. Johansson (2010), High-rate local sea level monitoring with a GNSS-based tide gauge, *Proceedings of the 2010 IEEE International Geoscience and Remote Sensing Symposium (IGARSS)*, 25–30 July 2010, Honolulu, HI, USA.pp. 3616–3619.

Ma, L. H., Y. B. Han, & Z. Q. Yin, (2009), Periodicities in Global Mean TEC from GNSS Observations, *Earth, Moon, and Planets*, 105, 1, pp. 3–10.

Martin-Neira, M., (1993), A PAssive Reflectometry and Interferometry System (PARIS): Application to ocean altimetry, *ESA J.*, 17, pp. 331–355.

Martin-Neira, M., P. Colmenarejo, G. Ruffini, & C. Serra, (2002), Altimetry precision of 1 cm over a pond using the wide-lane carrier phase of GPS reflected signals, *Can. J. Rem. Sens.*, 28, 3, pp. 394–403.

Masters, D., P. Axelrad, & S. Katzberg, (2004), Initial results of land-reflected GPS bistatic radar measurements in SMEX02, *Rem. Sens. Env.*, 92(4), pp. 507–520.

Mitchum, G. T., (1994), Comparison of Topex sea surface heights and tide gauge sea levels, *J. Geophys. Res.*, 99 (C12), pp. 24541-24554.

Mitchum, G. T., (2000), An improved calibration of satellite altimetric heights using tide gauge sea levels with adjustment for land motion, *Mar. Geodesy*, 23, pp. 145-166.

Moray, R., (1666), Considerations and inquiries concerning tides, *Phil. Trans. R. Soc. Lond.*, 1, 298.

Nakashima, Y., & K. Heki, (2013), GPS tide gauges using multipath signatures, *J. Geod. Soc. Japan*, in press.

Nicholls, R. J., P. P. Wong, V. R. Burkett, J. O. Codignotto, J. E. Hay, R. F. McLean, S. Ragoonaden, & C. D. Woodroffe, (2007), Coastal systems and low-lying areas, In: *Climate Change 2007: Impacts, Adaptation and Vulnerability*, Contribution of Working Group II to the Fourth Assessment Report of the Intergovernmental Panel on Climate Change [Parry, M. L., O. F. Canziani, J. P. Palutikof, P. J. van der Linden, & C. E. Hanson (eds.)], Cambridge University Press, Cambridge, UK, pp. 315–356.

Niell, A., (1996), Global mapping functions for the atmosphere delay at radio wavelengths, *J. Geophys. Res.*, 101, pp. 3227–3246.

Nievinski, F. G., (2013), Forward and inverse modeling of GPS multipath for snow monitoring, *Ph.D. thesis*, Department of Aerospace Engineering Sciences, University of Colorado.

Ning, T., G. Elgered, & J. M. Johansson, (2011), The Impact of Microwave Absorber and Radome Geometries on Geodetic Measurements With Ground-Based GNSS Antennas, *J. Adv. Space. Res. Scientific applications of Galileo and other Global Navigation Satellite Systems*, 47(2), pp. 186–196.

NOC (National Oceanographic Center), (2010), *Tidal predictions - UK & Irish tidal predictions*, National Environment Research Council, available from: `http://www.pol.ac.uk/ntslf/tidalp.html`, (December 31, 2013).

Nogués-Correig, O., S. Ribó, J. C. Arco, E. Cardellach, A. Rius, E. Valencia, J.M. Tarongí, A. Camps, H. van der Marel, & M. Martín-Neira, (2010), The proof of concept for 3-cm altimetry using the PARIS interferometric technique, *Proceedings of the 2010 IEEE International Geoscience and Remote Sensing Symposium*, July 25–30 2010, Honolulu, USA, pp. 3620–3623.

Park, K.-D., P. Elósegui, J. L. Davis, P. O. J. Jarlemark, B. E. Corey, A. E. Niell, J. E. Normandeau, C. E. Meertens, & V. A. Andreatta, (2004), Development of an antenna and multipath calibration system for Global Positioning System sites, *Radio Sci.*, 39, RS5002.

Polischuk, G. M., V. I. Kozlov, V. V. Ilitchov, A. G. Kozlov, V. A. Bartenev, V. E. Kossenko, N. A. Anphimov, S. G. Revnivykh, S. B. Pisarev, A. E. Tyulyakov, B. V. Shebshaevitch, A. B. Basevitch, and Y. L. Vorokhovsky, (2002), The Global Navigation Satellite System GLONASS: Development and Usage in the 21st Century, *34th Annual Precise Time and Time Interval (PTTI) Meeting*, December 3-5 2002, Reston, VA, United States.

Press, W. H., S. A. Teukolsky, W. T. Vetterling, & B. P. Flannery, (1992), *Numerical Recipes in Fortran 77. The Art of Scientific Computing*, 2nd Edition, Cambridge University Press, USA.

Pugh, D. T., (1996), *Tides, Surges, and Mean Sea-Level*, John Wiley & Sons Ltd., Great Britain, 472 pp.

Rees, W. G. (2003), *Physical principles of remote sensing, second edition*, University press, Cambridge, United Kingdom, 343 pp.

Rius, A., O. Nogués-Correig, S. Ribó, E. Cardellach, A. J. Camps, J. Marchán, & H. van der Marel, (2009), PARIS interferometric technique: proof of concept, *Proceedings of the 2nd International Colloquium - Scientific and Fundamental Aspects of the Galileo Programme*, European Space Agency, October 14–16 2009, Padua, Italy, 5 pp., proceedings CD ROM.

Rius, A., F. Fabra, S. Ribó, J. C. Arco, S. Oliveras, E. Cardellach, A. Camps, O. Nogués-Correig, J. Kainulainen, E. Rohue, & M. Martín-Neira, (2012), PARIS Interferometric Technique Proof Of Concept: Sea surface altimetry measurements, *Proceedings of IEEE International Geoscience and Remote Sensing Symposium*, IEEE Geoscience and Remote Sensing Society, 22–27 July, Munich, Germany, pp. 7067–7070.

Rivas, M. B., & M. Martin-Neira, (2006), Coherent GPS Reflections From the Sea Surface, *IEEE Geosci. Remote Sens. Lett.*, 3, 1, pp. 28–31.

Rosmorduc, V., J. Benveniste, E. Bronner, S. Dinardo, O. Lauret, C. Maheu, M. Milagro, & N. Picot, (2011), *Radar Altimetry Tutorial*, [J. Benveniste and N. Picot (Eds.)], available from: `http://www.altimetry.info`

Saastamoinen, J., (1971), Atmospheric correction for the troposphere and stratosphere in radio ranging for satellites, in The Use of Artificial Satellites for Geodesy, *Geophys. Monogr. Ser.*, 15, pp. 247–251, AGU, Washington, D.C.

Scargle, J. D., (1982), *Astrophysical Journal*, 263, pp. 835–853.

Scherneck, H.-G., J. M. Johansson, G. Elgered, J. L. Davis, B. Jonsson, G. Hedling, H. Koivula, M. Ollikainen, M. Poutanen, M. Vermeer, J. X. Mitrovica, & G. A. Milne, (2002), BIFROST: Observing the three-dimensional deformation of Fennoscandia, in: *Ice Sheets, Sea Level, and the Dynamic Earth*, AGU Geodyn. Ser., vol. 29., [Mitrovica, J. X., and B. Vermeersen (eds.)], American Geophysical Union, Washington, DC, pp. 69–93.

Scherneck, H.-G., M. Lidberg, R. Haas, J. M. Johansson, & G. A. Milne, (2010), Fennoscandian strain rates from BIFROST GPS: A gravitating, thick-plate approach, *J. Geodyn.*, 50(1), pp. 19–26.

Schöne, T., N. Schön, & D. Thaller, (2009), IGS Tide Gauge Benchmark Monitoring Pilot Project (TIGA): scientific benefits, *J. Geod.*, 83, pp. 249–261.

Seeber, G., (1993), *Satellite Geodesy - Foundations, Methods, and Applications*, Walter de Gruyter, Berlin, 531 pp.

Semmling, M., T. Schmidt, J. Wickert, S. Schön, F. Fabra, E. Cardellach, & A. Rius, (2012), On the Retrieval of the Specular Reflection in GNSS Carrier Observations for Ocean Altimetry, *Radio Sci.*, 47, RS6007.

Semmling, A. M., J. Wickert, S. Schön, R. Stosius, T. Gerber, M. Markgraf, M. Ge, & G. A. Beyerle, (2013), Zeppelin experiment to study airborne altimetry using specular Global Navigation Satellite System reflections, *Radio Sci.*, 48, pp. 427440.

Stewart, R. H., (2008), *Introduction to Physical Oceanography*, Department of Oceanography, Texas A & M University, 353 pp., available from: `http://oceanworld.tamu.edu/resources/ocng_textbook/contents.html`, (December 31, 2013).

Teunissen, P. J. G. (1993), Least-squares estimation of the integer GPS ambiguities, *invited lecture, Section IV Theory and Methodology, IAG General meeting*, Beijing, China, 16 p., also in Delft Geodetic Computing Centre LGR series No. 6.

Teunissen, P. J. G., (1994), A new method for fast carrier phase ambiguity estimation, in *Proceeding IEEE Position, Location and Navigation Symposium PLANS 94*, Las Vegas, Nevada, USA, April 11–15, 1994. pp. 562–573.

Teunissen, P. J. G., (1995), The least-squares ambiguity decorrelation adjustment: a method for fast GPS integer ambiguity estimation, *J. Geod.*, 70, pp. 65–82.

Teunissen, P. J. G., & A. Kleusberg, (1998), *GPS for Geodesy, 2nd Edition*, Springer, Berlin, 650 pp.

UNAVCO (University NAVstar COnsortium), (2013), General Information – GNSS Modernization, avaiable from `http://facility.unavco.org/general-info/gnss-modernization/gnss-modernization.html`, (November 28, 2013).

Vestol, O., (2013), National Report from Norway, *EUREF 2013 Symposium*, May 29–31, 2013, presentation, Budapest, Hungary, available from: `http://euref2013.fomi.hu/Download/Session_6/Norway_NationalReport2013.pdf`, (December 2, 2013).

Ward, P., (1996), Satellite signal acquisition and tracking, in *Understanding GPS: Principles and Applications*, edited by E. D. Kaplan, Artech House, Norwood, Mass.

Watkins, K., C. Ugaz, L. Carvajal, D. Coppard, R. F. Nieva, A. Gaye, W. Ha, C. Johansson, A. Kennedy, C. Kuonqui, I. M. Pereira, R. Menon, J. Morse, & P. Seck, (2007), Human Development Report 2007/2008 - Fighting climate change: Human solidarity in a divided world, Palgrave Macmillan, New York, USA, for United Nations Development Programme, 384 pp.

Wöppelmann, G., C. Letetrel, A. Santamaria, M.-N. Bouin, X. Collilieux, Z. Altamimi, S. D. P. Williams, & B. Martin Miguez, (2009), Rates of sea-level change over the past century in a geocentric reference frame, *Geophys. Res. Lett.*, 36, L12607.

Zumberge, J. F., M. B. Heflin, D. C. Jefferson, M. M. Watkins, & F. H. Webb, (1997), Precise point positioning for the efficient and robust analysis of GPS data from large networks, *J. Geophys. Res.*, 102 (B3), pp. 5005–5017.

Paper I

Monitoring Coastal Sea Level Using Reflected GNSS Signals

Johan S. Löfgren, Rüdiger Haas, & Jan M. Johansson

Journal of Advances in Space Research, 47(2), pp. 213–220, 2011

Paper II

Three Months of Local Sea Level Derived from Reflected GNSS Signals

Johan S. Löfgren, Rüdiger Haas, Hans-Georg Scherneck, & Machiel S. Bos

Radio Science, 46, RS0C05, 12 pp., 2011

Paper III

Coastal Sea Level Measurements Using a Single Geodetic GPS Receiver

Kristine M. Larsson, Johan S. Löfgren, & Rüdiger Haas

Journal of Advances in Space Research, 51(8), pp. 1301–1310, 2013

Paper IV

Sea Level Time Series and Ocean Tide Analysis from Multipath Signals at Five GPS Sites in Different Parts of the World

Johan S. Löfgren, Rüdiger Haas, & Hans-Georg Scherneck

Submitted to Journal of Geodynamics, September 2013

Paper V

Sea Level Measurements Using Multi-Frequency GPS and GLONASS Observations

Johan S. Löfgren & Rüdiger Haas

Submitted to EURASIP Journal on Advances in Signal Processing, December 2013